DEVELOPING BIOMATERIALS THROUGH ENHANCING ORGANIC/INORGANIC INTERFACES

By Erik Andreas Bjørnstad Hughes

A thesis submitted to the

School of Chemical Engineering, College of Engineering

and Physical Sciences, University of Birmingham

For the degree of

DOCTOR OF ENGINEERING (EngD)

School of Chemical Engineering

College of Physical Sciences and Engineering

University of Birmingham

B15 2TT

August 2017

ABSTRACT

The socioeconomic demand for biomaterials has never been greater. Formulation at the organic/inorganic interface of materials has enabled the conception of several novel biomaterial systems for bone repair and bone fusion applications, which are presented across four research chapters (Chapters 2-5).

In Chapter 2, a poly(ether ether ketone) (PEEK) and calcium sulphate (CS) composite is formulated. The inclusion of the polymer slowed CS degradation and augmented the mechanical properties of the material significantly. Chapter 3 examines the formation mechanism of tubular calcium phosphate structures from a gel/solution interface. The tube composition and microstructure was analogous with intricate features of bone. In Chapter 4, a model bone defect was augmented with particles that could generate calcium phosphate tubes in the presence of biological tissue. 3D computed tomography reconstructions revealed extensive bone-like mineral deposition throughout the cavity. Chapter 5 explores the chemical coupling of hydroxyapatite particles within a PEEK matrix, a composite that may be used for fabricating spinal fusion devices. Physical properties of chemically linked composites were improved by a reduction in additive debonding and inhibition of micro crack formation. This allowed more effective load transfer between phases.

Together, the research presented herein puts forward a novel collection of biomaterials that may be applied to the treatment of bone fractures and fusion of the spine.

ACKOWLEDGEMENTS

I wish to extend a massive thank you to my supervisor, Prof. Liam Grover, whose supervision throughout my EngD has been invaluable. I'm so grateful to have had the opportunity to work and develop as a scientist under your guidance. I also want to thank Dr. Richard Greenwood for giving me the chance to undertake the EngD project. It has been a blast!

I extend my thanks to TWI Ltd for allowing me to gain industry experience during my project. Thank you to my industrial supervisors over the course of my project, including Dr. Judith Juhasz, Prof. Medhi Tavakoli, and Dr. Roger Wise.

I want to thank all the past and current members of TRIAL lab, as well as the many researchers I have been lucky enough to collaborate with over the last five years. Special thanks must go to Dr. Richard Williams for his eclectic mix of expertise and banter. Not forgetting the countless work sessions in Costa!

I offer my wholehearted thanks to my family, especially my parents and sister for supporting me throughout my EngD. I couldn't have done this without you. Most importantly, I have to thank the love of my life, Holly, for her support. You have made me laugh every day we have been together and throughout my write-up. I know you love your books but I have a feeling my thesis won't make your collection!

For Dad

TABLE OF CONTENTS

LIST OF FIGURES

LIST OF TABLES

LIST OF PAPERS

Review papers

Hughes EAB, Yanni T, Jamshidi P, Grover LM. Inorganic cements for biomedical application: calcium phosphate, calcium sulphate and calcium silicate. Advances in Applied Ceramics. 2015;114(2):65-76.

Research papers

Hughes EAB, Grover LM. Characterisation of a novel poly (ether ether ketone)/calcium sulphate composite for bone augmentation. Biomater Res. 2017;21:7.

Hughes EAB, Williams RL, Cox SC, Grover LM. Biologically Analogous Calcium Phosphate Tubes from a Chemical Garden. Langmuir. 2017;33(8):2059-67.

Hughes EAB, Cox SC, Cooke ME, Williams RL, Hall TJ, Grover LM. Interfacial mineral fusion and tubule entanglement as a means to harden a bone augmentation material. *Submitted.*

Hughes EAB, Parkes A, Williams RL, Jenkins MJ, Grover LM. Development of a covalently bonded hydroxyapatite and PEEK composite. *Submitted.*

AUTHOR STATEMENT

This thesis presents four published or submitted papers that have been adapted into chapters. The author of this thesis is the first author of the adapted works presented herein. Conception of the experiments, undertaking of the experimental work, and manuscript writing was undertaken by the first author. Secondary authors are duly acknowledged for their contribution to the work through assistance with experimental work and help revising manuscripts. Industrial sponsors TWI Ltd approved the publication and submission of the manuscripts presented herein.

Chapter 1. Introduction

1.0 RESEARCH AIMS AND OBJECTIVES

The literature regarding the development of biomaterials consists of many decades worth of explorative research studies that focus on the formulation and employment of many different materials suitable for healing hard and soft tissues. Whilst the current cohort of clinically employed hard tissue biomaterials appears to result in widely positive restorative outcomes, it is recognised that both tissue derived and synthetic substitutes are unable to match or overtake bone in terms of mechanical and biological performance [1]. Therefore, the field of research continues to evolve as researchers innovate novel methods to fabricate and characterise biomaterials that aim to emulate the structure and properties of bone, in addition to furthering the understanding of the interactions between such biomaterials and the body.

The aim of this thesis is to formulate calcium sulphate and phosphate based composites with enhanced physiochemical properties and structural features that can be utilised in applications including bone regeneration and hard tissue fusion. In order to achieve this aim, the following objectives will be addressed:

- To identify the inherent shortcomings of biomaterials employed in bone defect augmentation and spinal fusion applications.
- To overcome the identified shortcomings of these biomaterials by strategically formulating and fabricating novel composites that possess enhanced interfacial interactions between organic/inorganic interfaces present between dissimilar phases.

- To determine nature and significance of the organic/inorganic interactions relating to biomaterial property enhancement using an extensive array of advanced chemical and physical characterisation techniques.

1.1 RESEARCH MOTIVATION

1.1.1 Increasing and ageing population

The global population crossed the 7.6 billion mark in mid-2017 and continues to grow at a staggering rate on a daily basis [2]. These numbers reflect the healthier lifestyles more people are choosing to adopt, advances in improved life expectancy, tackling infant mortality and increased longevity of the ageing population [3].

Consequently, the incidence of age-related diseases associated with our bones, such as osteoporosis, which describes the loss and thinning of the bone structure, and osteoarthritis, which describes the loss of cartilage and stiffening of bony joints, are continually on the rise. In the UK alone, approximately 3.2 million and 8.75 million people suffer from osteoporosis and osteoarthritis respectively according to figures obtained earlier during this decade [4, 5].

1.1.2 Occurrence

1.1.2.1 Bone fractures

Around 8 million people suffer a bone fracture in the United States every year, with up to approximately 10 % of cases resulting in persistence of

non-union, which can have negative implications for hard tissue function [6]. Younger people appear to be increasingly prone to muscoskeletal incidents that are normally associated with age due to lifestyle habits, such as participation in injury risk sports, as well as involvement in traffic accidents [7-9]. For the elderly, risk factors include degenerative diseases (e.g. osteoporosis), muscle weakness and loss of balance leading to traumatic injury.

Osteoporosis is a disease prevalent in the over 50's population, and affects around 200 million people around the world [10]. The loss of bone mineral density and strength due to osteoporosis leads to greater risk of fracture with regards to weight bearing bones. This is a major concern as it is these members of the population who may be prone to accidental and minor falls, resulting in the fracture of bones, and in extreme circumstances, increase the chance of premature death by up to 20 % [11, 12]. Around 300000 fragility fractures occur a year in the UK due to such incidences. For very frail individuals, 10 % to 20 % of these falls will result in hip fracture [13].

1.1.2.2 Spinal conditions

Lower back pain is a highly reported ailment that can advance to more serious spinal illnesses requiring medical attention, including degenerative disc disorder and disc herniation. Pain is felt as a consequence of pressure being applied to spinal nerves. This pain can also transcend to the legs in the case of radicular spinal nerve compression.

Annually in the USA, over 65 million people experience and suffer lower back pain, and 85 % of the population will display evidence of disc

degeneration by the age of 50 [14]. In the UK, approximately 27 million people suffer lower back pain yearly and are typically aged between 40 and 60 years of age [15]. Herniated disc disease is most prevalent in the 30 to 50-year-old population, with 95 % of cases affecting the lower lumbar region of the spine [16].

1.1.3 Prevention shortcomings

1.1.3.1 Bone fractures

Systematic avoidance strategies may prevent 25 % of osteoporotic hip fractures [17, 18]. These include raising awareness of osteoporosis, better identification of those most at risk of fracture (e.g. do they have a parental history regarding fracture), provision of preventative drugs to aid those at risk (i.e. postmenopausal osteoporosis sufferers), encouraging individuals to perform a level of physical activity that maintains muscle strength and bone density from an early age as well as later in life, exposure to sunlight in order to increase vitamin D levels, and ensuring those receiving treatment are compliant over several years (i.e. following a course of prescribed medicine) [11, 19-26]. Despite following preventative measures however, bone fractures aren't always avoidable and will require some form of intervention to repair or augment the damaged bone. Costs are further driven up by fracture reoccurrence, unforeseen circumstances, and fracturing other bones in the body [27].

1.1.3.2 Spinal conditions

Lower back pain is managed by an initial assessment followed by preventative measures. Preventative measures for spinal conditions include staying active, prescription of anti-depressants, bed rest, epidural injections, heat placement, ice placement, massages and traction [16]. These interventions aim to relieve pain, increase patient mobility, and improve quality of life. If pain persists, further non-surgical approaches to manage the condition may be carried out, including psychological therapy and acupuncture [15].

Worryingly, preventive measures are recommended to last between 6 to 12 months before surgical treatment is considered, whilst there is no evidence to prove the effectiveness of such treatments following a 6-week period [28]. This may be due to the historical attitude of healthcare professionals that spinal maintenance can be overcome by changes in lifestyle as opposed to the need to spend on healthcare resources [29]. Furthermore, a UK study conducted at the start of the decade found that only 50 % of the 127 primary care organisations surveyed provided funding for acupuncture treatment and only 15 % offered acupuncture within the practice itself [15].

Taken together, evidence worryingly suggests that the effectiveness of recommended early treatment strategies is unfounded, in addition to the fact that treatment guidelines may be seldom applied. Therefore, preventative measures for spinal conditions potentially offer a poor outlook for patients, increasing the likelihood of surgical intervention.

1.1.4 Socioeconomic demand

1.1.4.1 Bone fractures

Problematically, unlike younger individuals whose fractures tend to heal without complication, osteoporotic bone does not possess the regenerative capacity to heal fractures without major intervention.

Fractures are extremely costly; the occurrence of approximately 75000 hip fractures for instance in the UK costs as much as £2 billion per annum to treat [30]. Fractures incurred from osteoporosis are severe, as they will almost certainly require intervention and subsequent treatment to stabilise and replenish the damaged bone tissue. Over 500,000 operations in the USA per year require the use of bone graft, with 50 % of these being related to spine surgeries [31]. The provision of biomaterials that are able to stimulate healing in both healthy and diseased bone is therefore crucial, especially given that the economic burden of providing treatment for new and previous osteoporotic fractures in the UK is set to increase from £3.5 billion to £5.5 billion by the year 2025 [32].

Furthermore, the pain associated with fractures can range from acute to chronic depending on severity [33]. Fractures are therefore not only considered a major economic burden, but also a detrimental burden to a person's health and wellbeing. Consequently, the socioeconomic demand for biomaterials that are able to restore and regenerate bone tissue in a cost-effective manner, so as to avoid reoccurrence and need for surgical revision, has never been greater.

1.1.4.2 Spinal conditions

Treatment of lower back pain is essential for a patient's wellbeing. Not only is the suffering of pain uncomfortable, it can also lead to depression and anxiety. Spinal conditions can therefore be debilitating, often requiring sufferers to take leave from work for extended periods. In the UK, the treatment of back pain costs upward of £1 billion annually, and furthermore costs the economy £12.3 billion annually through people being unable to work [15]. These figures indicate that back pain is more of an economic burden compared to other illnesses, including heart disease, Alzheimer's disease, and diabetes [34].

Surgical intervention with a spinal fusion procedure is recommended for pain alleviation. The frequency of such procedures has continually risen over recent decades, and is partially due to advancements in the technologies of the components, such as fixative screws and fusion cages, being employed [34]. As such, there is a growing demand to further evolve the technologies of spinal fusion components with increasing fusion efficacy.

1.2 BONE

1.2.1 Overview of bone

Bone consists of a mineralised extracellular matrix, containing both organic and inorganic components, as well as active populations of cells responsible for maintaining a function and healthy tissue structure. Bone has a capacity to regenerate and repair itself, and can therefore be thought of as a dynamic living composite. The human body contains 206 individual bones,

made up of 126 bones of the appendicular skeleton, 74 bones of the axial skeleton, and 6 bones of the auditory ossicles [35].

Bones of the human skeletal system are categorized as flat, long, short, irregular and sesamoid. Flat bones, which possess flattened morphologies, include the cranial and rib bones, and serve protective functions. Long bones are elongated structures and include the femur and the humerus. These bones typically facilitate movement through joints and bear load. Short bones provide a supportive role in combination with other bones, and are associated with little movement. Irregular bones exhibit irregular and complex structures, and include the vertebrae, a collection of 33 bones that constitute the human spine. Finally, sesamoid bones are embedded in tendons and protect them from stress. The kneecap, or patella, is an example of sesamoid bone.

1.2.2 Bone properties and function

Hierarchical structuring from the nano- to the macro- scale provides bone with impressive mechanical properties (Table 1.1), which means that it can provide structural support, facilitate movement through interaction with muscles, and protect organs. Bone also has less obvious, but equally important functions such as mineral and acid-base homeostasis. It also stores growth factors, and provides space for the generation of blood cells [35, 36].

Table 1.1 Mechanical properties of cortical and cancellous bone (Adapted from [37] with permission from Copyright © 2011 Bentham Science Publishers).

Property	Cortical bone	Cancellous bone
Compressive strength (MPa)	100-230	2-12
Flexural, Tensile strength (MPa)	50-150	10-20
Strain to failure	1-3	5-7
Tensile modulus (GPa)	7-30	0.05-0.5
Fracture toughness (K_{IC}) (MPa.$m^{1/2}$)	2-12	-

1.3 BONE COMPOSITION

The composition of bone includes both organic and inorganic components that undergo constant structural re-modeling by cell-mediated processes.

1.3.1 Organic components

Organic components contribute to around 30 % of bone mass. Approximately 90 % of this mass is accounted for by type-1 collagen, with noncollagenous proteins (NCPs), lipids, and mass of hydration together making up the remaining 10 % mass [38, 39]. Collagen type I molecules consist of three polypeptide chains, specifically two alpha 1 chains and an alpha 2 chain, which self-arrange as triple helices that are 300 nm in length and 1.23 nm wide [40, 41]. This collagen structure is referred to as

tropocollagen. In bone, a spacing of 40 nm exists between the top and bottom of each segment of tropocollagen where mineralisation is initiated.

This material is the basic building block of many human soft and hard tissues as well as bone, including skin, ligaments, tendons, and teeth [42].

1.3.2 Inorganic components

Up to 70 % of the remaining bone mass is apatitic calcium phosphate mineral, first identified in the 1920's by X-ray diffraction, and later confirmed in the 1930's [43, 44]. This mineral is generally identified as hydroxyapatite (HA) ($Ca_{10}(PO_4)_6(OH)_2$), however this form of the bulk phase of inorganic bone material is considered extremely pure [45]. Stoichiometric HA has a calcium to phosphorous (Ca/P) ratio of 1.67. In reality the naturally occurring composition of HA may deviate from this stoichiometry, being either calcium deficient ($Ca_9(PO_4)_5(HPO_4)OH$), or containing ionic substitutions. The most prevalent substitution of bone mineral is of the carbonate (CO_3^{2-}) anion in place of either hydroxyl (-OH), or more commonly phosphate (PO_4) groups, referred to as A type and B type substitution, respectively [46, 47]. Carbonate makes up 2 % to 8 % of bone mineral by mass [46, 47]. Additionally, minor concentrations of Mg, Na, as well as trace concentrations of Si, Sr, Zn, Pb, have been identified [45]. It is believed that these impurities and non-stoichiometric phases contribute to chemical changes in HA mineral in terms of surface reactivity and charge, and also make mineral more soluble such that the release of ions may promote bone remodeling and turnover [45].

Moreover, despite the nanocrystalline nature of bone mineral, it is considered overall to be poorly crystalline due to the presence of an amorphous fraction. The presence of amorphous calcium phosphate (ACP) contributes to the low crystallinity, and it is thought that the formation of bone includes a step where ACP matures to form a more crystalline HA [48, 49].

1.4 BONE ORGANISATION

Bone is structured from the molecular to macroscales. These include tropocollagen organisation, micro fibrilous, fibrilous, lamellar, osteonal, and macroscopic levels [50]. The structure of bone at each length scale is shown in Figure 1.1.

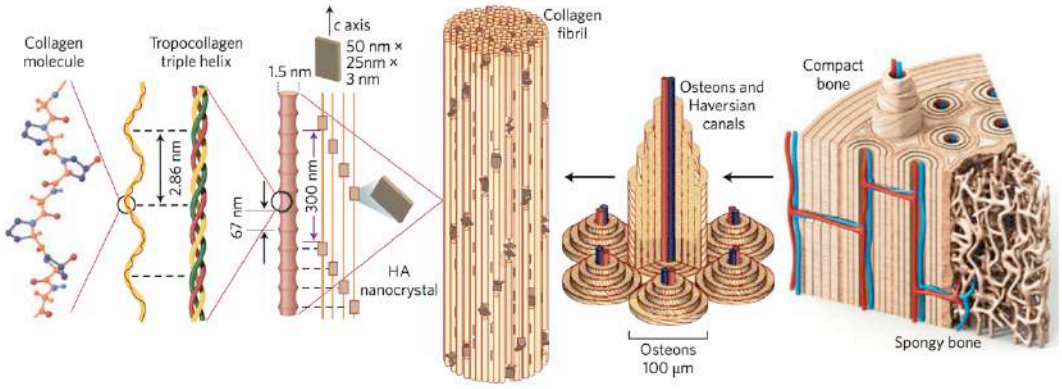

Figure 1.1 Schematic of bone structure from the molecular to the macrosacle (Adapted from [40] with permission from Copyright © 2014 Nature Publishing Group).

1.4.1 Organisation of collagen

With regards to bone, the organization of collagen is complex and has been thoroughly examined [51, 52]. On the molecular level, tropocollagen

molecules are assembled into triple helix structures that align in a quarter-staggered array to form a microfibril.

A collection of microfibrils constitutes a collagen fiber. In the formation of bone tissue, arrangements of mineralised collagen fibres may be disordered, resulting in woven bone structure, or be highly aligned, forming sheets of lamellar bone structure [39]. Disordered woven bone is remodeled to aligned lamellar bone, giving rise to trabecular and cortical bone structures (Figure 1.1).

1.4.2 Organisation of apatite

Apatitic mineral nucleates in the 40 nm spacing between the top and bottom of each tropocollagen segment, and extends into the 0.24 nm gaps that exist between parallel tropocollagen collagen molecules arranged within microfibrils and around them. The resulting HA nanocrystals are described as platelets, which exhibit an irregular structure but are often assigned approximate dimensions of 50 nm x 25 nm x 3 nm, aligning on the c-axis parallel to the direction of collagen [40, 50]. It remains unknown as to the involvement of collagen in the processes by which amorphous mineral precursor evolves into highly orientated HA nanocrystals [53]. There are two trains of thought, the first being NCPs influence apatite nucleation, and the second being that nucleation sites exist upon collagen [53].

1.4.3 Cortical bone

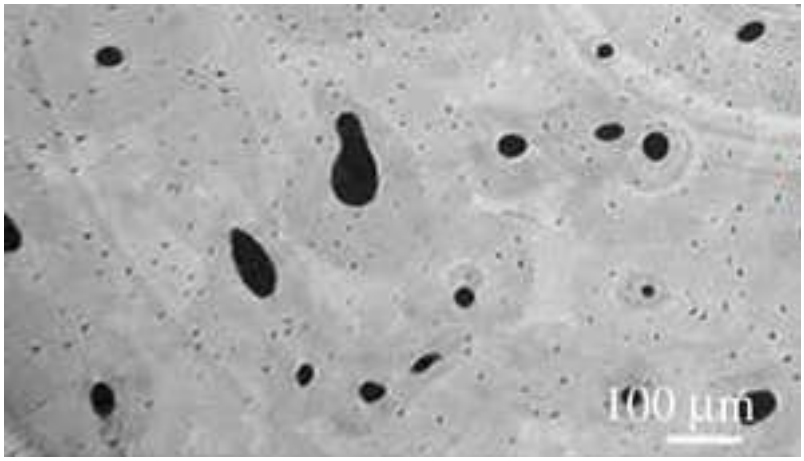

Figure 1.2 Osteonal microstructure of cortical bone imaged with synchrotron radiation-based computed tomography technique (Adapted from [55] with permission from Copyright © 2016 The Royal Society).

Cortical bone is often referred to as compact bone due to its dense structuring and relatively low porosity ranging between 5 % and 10 % [35, 54, 55] (Figure 1.2).

Within cortical bone, collagen fiber sheets form concentric circular channels, termed osteons [39, 55, 56]. Osteons house a complex system of Haversian canals containing blood vessels that align parallel to the length of long bones [55-57] (Figure 1.3). Volkman's canals are another type of vascular channel, which interconnect the vessels of the Haversian system perpendicular to the length of long bones [56, 57].

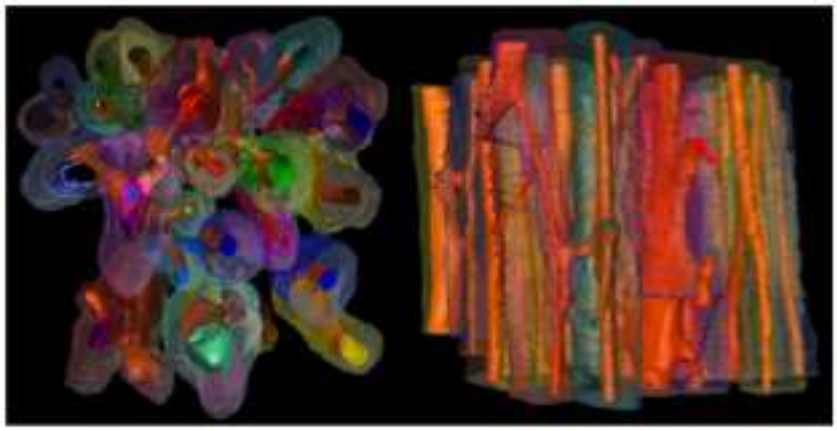

Figure 1.3 Reconstruction of the Haversian system in a 2.93 mm^3 sample of human femoral bone tissue imaged with synchrotron radiation-based computed tomography technique (Orange is representative of the outline of individual Haversian canals, whilst the multi-hued regions are representative of the osteonal morphology) (Adapted from [57] with permission from Copyright © 2016 Anatomical Society).

1.4.4 Trabecular bone

Trabecular, or spongy bone, is 50 % to 90 % porous, and is interspersed in the marrow compartment [35, 54, 55] (Figure 1.4). This type of bone architecture is encased by cortical bone structure.

In the development of trabecular tissue, collagen fiber sheets align parallel to one another resulting in an open network structure of interconnected trabeculae. This bone tissue is subsequently referred to as spongy bone because of this structuring.

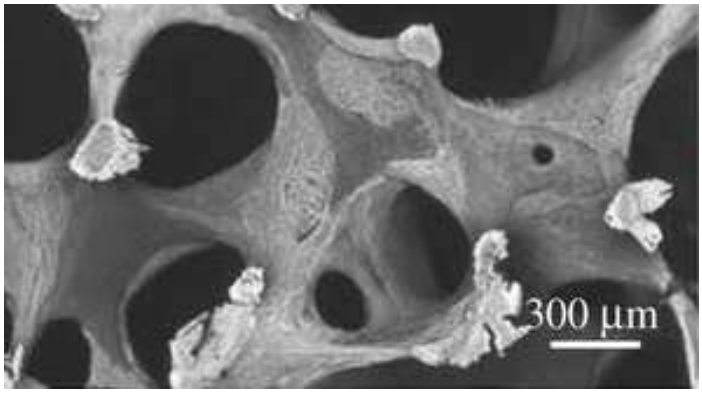

Figure 1.4 Trabecular microstructure of cancellous bone imaged with back scattered scanning electron microscopy technique (Adapted from [55] with permission from Copyright © 2016 The Royal Society).

1.5 BONE CELLS

Bone is a living tissue that undergoes constant remodeling by cellular processes. Several different cells are present in mineralized tissue, which include primarily osteoblasts, osteocytes and osteoclasts [58]. Generally, osteoblasts are responsible for the deposition of bone, whilst osteoclasts are responsible for its resorption [58, 59]. In order to balance deposition and resorption activities, signaling molecules are released by bone cells themselves that influence one another's activity [59]. Osteoblasts secrete factors such as osteoprotegerin (OPG) that inhibit osteoclast cell function, and furthermore, osteocytes regulate both the activity of osteoblast and osteoclast cells [60]. The secretion of sclerostin from osteocytes, which are osteoblast cells that have become encapsulated in mineralized tissue, inhibits further bone formation from osteoblasts [61]. Immune cells also generate signaling molecules that enhance or lessen bone remodeling by cellular components [62].

1.5.1 Osteoblasts

Osteoblast function is associated with bone production, with their main functions including osteoid deposition and the regulation of bone resorption [59]. Osteoblasts differentiate from pluripotent mesenchymal stem cells (MSCs), which also have the potential to develop into adipocytes, myocytes, and chondrocytes [63]. The differentiation to the osteoblast lineage is driven by runt-related transcription factor 2 (Runx2) and Osterix transcription factors [64, 65]. Canonical Wnt signaling has also been shown to be important for the fate of maturing pre-osteoblastic cells into osteoblasts [66]. The development of these cells promotes the development of osteoclast cells, as shown in experiments where mice devoid of early osteoblast cells did not develop a normal population of osteoclasts, suggesting that immature bone forming cells are partially responsible for the formation of their bone resorbing counterparts [63, 67].

Osteoblasts can also influence osteoclast activity, promoting bone dissolution or reducing it, in coordination with their own functions. The release of receptor activator of nuclear factor κB ligand (RANKL) from osteoblasts promotes osteoclast differentiation and their breakdown of bone by binding to nuclear factor κB (RANK) on the surface of preosteoclasts [68]. Osteoblasts may also release OPG, which blocks the binding of RANKL with RANK through binding with RANKL [68].

1.5.2 Osteocytes

Cells of the osteoblastic linage terminally differentiate into osteocytes when they become entrapped by a bony matrix, which are the most abundant cell found in bone tissue outnumbering osteoblasts by a factor of 10 in human bone [69]. During bone deposition, a population of osteoblasts becomes engulfed in the surrounding bone mineral. The resulting osteocytes occupy a space know as a lacuna, and possess dendritic spindles that extend and link to other osteocytes through canaliculi. These cells influence the remodeling process through the release of signaling molecules that stimulate bone formation or resorption processes in response to chemical and mechanical stimuli [60].

1.5.3 Osteoclasts

Bone apatite is dissolved by osteoclasts [70]. Osteoclast cells are members of monocyte/macrophage lineage and form from the fusion of mononuclear osteoclast precursors [70]. A complex mixture of hormones and mediators found in the bone matrix influences the development of osteoclast cells [71]. Once fully differentiated, these cells are relatively large, and can possess variable numbers of nuclei, typically between 3 and 20 [70, 72]. Pathological bone osteoclasts may contain even more nuclei, for instance in Paget's disease, where over 100 nuclei have been observed [73].

Osteoclasts can be characterized by their expression of several osteoclast markers, including tartrate resistant acid phosphatase (TRAP), matrix metalloproteinase (MMP), cathepsin K and others [71]. Both the

breaking down of bone mineral, as well as the organic matrix of bone, is accomplished by enzymatic degradation as determined by osteoclast activity.

1.6 BONE REMODELING

Bone remodeling involves a balancing act between bone formation and bone resorption. The process removes old bone tissue, replacing it with a new mineralizing collagenous matrix. This prevents long-term accumulation of micro damage, maintaining bone in terms of its structure, quality and strength [35, 39].

In healthy adults, remodeling occurs through a series of systematic stages, beginning with activation, followed by resorption, reversal, and finally formation [35, 39]. These processes take place at the site of a basic multicellular unit (BMU), involving complex signaling pathways between osteoblasts, osteoclasts, and osteocytes [74]. Resorption processes are relatively fast in comparison to the development of new bone; it may take several weeks to resorb bone, however, it can take several months to deposit new mineral [59]. Pathological conditions associated with bone remodeling include osteoporosis, whereby osteoclast activity outweighs that of bone forming osteoblasts, resulting in a loss of bone mineral density [75].

1.6.1 Activation

Mechanical loads may activate remodeling non-specifically. Osteocytes are able to detect mechanical forces as shown by demonstrating a strong response to the flow of interstitial fluid within the lacuna and canaliculi spaces,

which results in the release of signaling molecules that influence bone remodeling [60, 76]. BMUs may be steered to specific areas of localised micro damage, targeting specific sites to remodel [77, 78].

1.6.2 Resorption

On the initiation of resorption, bone lining cells, which spread over bony surfaces, make-way for incoming osteoclasts [79, 80]. Osteoclasts form a sealing zone on the surface of bone. Adhesion can be influenced by surface energy [81]. Membrane bound molecules also ensure stable attachment of osteoclasts for bone resorption. Resorption is characterised by the formation of the ruffled border that is an intensely convoluted structure found at the sealing zone [82]. Its formation isn't fully understood [82]. Calcium phosphate crystals localise at the ruffled border [83]. These crystals reveal distinctive alterations such as variation of shape and electron density due to bone resorption activities [83].

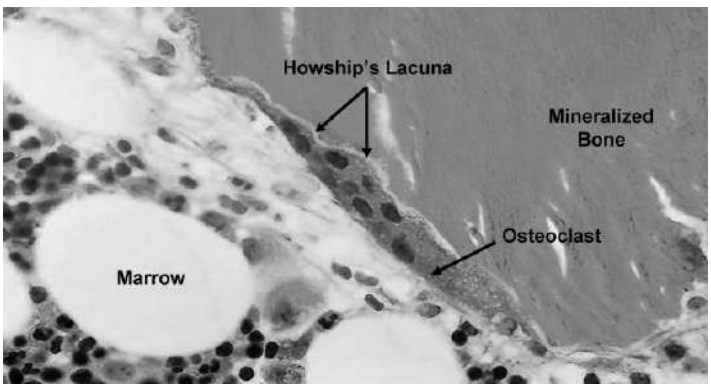

Figure 1.5 Howship's lacuna develop where osteoclasts resorb bone (Adapted from [35] with permission from Copyright © 2008 American Society of Nephrology).

The main two resorption processes, acid secretion and proteolysis, are believed to occur simultaneously [82]. Release of HCl promotes HA matrix dissolution. The high level of H^+ ions that is needed comes from the catalysis of CO_2 and H_2O to form H_2CO_3 [82]. The H_2CO_3 then ionizes into H^+ and CO_3^- ions [84]. The exchange of CO_3^- with Cl^- ions provides the Cl^- ions needed for acidification and break down of apatite [84]. Proteolysis and subsequent breakdown of collagen is due to the activity of cathepsin K, MMP, and gelatinase released from cytoplasmic lysosomes, all active at low pH levels [82, 85]. Resorption pits form where digestion takes place, referred to as Howship's lacunae, which were first identified in the 1960s (Figure 1.5) [35, 86].

1.6.3 Reversal

Following resorption, an intermittent period in the remodeling process follows known as the reversal phase, which can last several weeks [79]. In this time, osteoclasts undergo apoptosis and the pro-osteogenic signals released from osteoclasts at the end of resorption stimulate pre-osteoblasts to differentiate into osteoblasts [79, 87]. A myriad of chemical signals and growth factors released during resorption may also stimulate pre-osteoblast recruitment and activity [62, 88]. Mononuclear cells also prepare the resorbed surface for bone deposition [62].

1.6.4 Formation

Osteoblasts replenish resorbed areas with osteoid, which consists of bone’s non-mineral components. An osteoblast may deposit 2 to 3 times its

volume in osteoid before it transforms into an osteocyte, effectively becoming cocooned in bone matrix post-mineralisation, or alternatively an osteoblast lining cell, covering the newly formed bone osteoid and forming networks to osteocytes via canaliculi channels [35, 89, 90] (Figure 1.6).

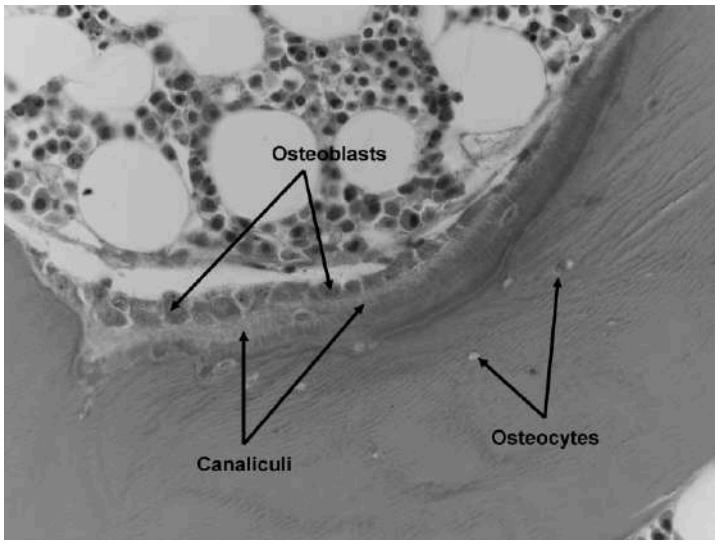

Figure 1.6 Synthesis and deposition of collagenous bone matrix by osteoblast cells. As mineralisation proceeds, osteoblasts transform into osteocytes, becoming encapsulated in hard tissue (Adapted from [35] with permission from Copyright © 2008 American Society of Nephrology).

Mineralisation of the osteoid ensues in a matter of days following its deposition, beginning with the precipitation of amorphous calcium phosphate mineral in between collagen arrangements as previously described, which matures into nanocrystalline hydroxyapatite [91]. An approximate 20 % fraction of the initial mineral remains amorphous and contributes toward maintaining ionic homeostasis [91].

1.7 BONE REPAIR

In the event of fracture, the damage caused to bone may compromise the integrity of the skeletal system, cellular components and blood supply, all of which are addressed by healing. Healthy bone possesses an impressive healing capacity that does not leave a scar, and will heal without the presence of rigid fixation for defects up to 12 mm in length [92, 93]. Healing of fractures occurs in three stages, starting with inflammation, followed by repair, and finally remodeling, which when successful, replenish damaged bone with healthy mineralised tissue as to avoid a non-union scenario and restore function [92, 94].

Enhanced bone healing can be facilitated through invasive techniques such as electrical stimulation, low intensity pulsed ultrasound, and externally applied shock waves, which promote mechanical and biological stimuli [95]. The natural bone healing processes may be impaired by disease, smoking, diabetes, and the position of the non-union [96].

1.7.1 Inflammation

The inflammatory response following fracture is immediate, peaking after a couple of days and lasting around a week in total [92]. During this time, the fracture site is both swollen and painful, which although uncomfortable, prevents unnecessary movement of the fracture site. At the start of the inflammation stage, disruption of the normal organisation of hard tissue results in breakage of vasculature, facilitating acute necrosis, acidosis and hypoxia of surrounding bone and tissue local to the fracture [97].

Consequently, complex signaling cascades result in the release of specific chemotactic agents, which initiate the migration of platelets, neutrophils, macrophages, fibroblasts, blood monocytes, polymorphonuclear leukocytes, and undifferentiated cells toward inflamed tissue where a haematoma (blood clot) develops due to the accumulation of blood, which clots at the fracture site [92, 94].

A cocktail of signaling molecules and growth factors are present within the resulting haematoma and are essential in bone healing by activating specific cellular processes [92, 94]. These molecular components are responsible for promoting the formation of extracellular matrix, angiogenesis, chemo attraction of immune and mesenchymal cells, and fibroblast recruitment [98]. For instance, cytokines IL-1 and IL-6 recruit the movement of mesenchymal cells that proliferate into chondrogenic and osteogenic cells [92, 94, 98].

1.7.2 Repair

The repair phase overlaps the inflammatory period, beginning after a few days and can continue for a few weeks [92, 99]. During the repair phase, the haematoma is first transformed to granulated tissue. This consists of fibrous tissue deposited by fibroblasts that bridges the junction of the fracture gap and contains a high concentration of new blood vessels. Despite being mechanically weak, the resulting soft callus supports the penetration of vasculature, restoring a blood supply to the healing space [92, 99] .

The soft callus transitions into a hard and bony callus by ossification processes. Ossification can take place through either an indirect (secondary) or direct (primary) pathway. Commonly, natural fracture healing proceeds through the indirect pathway, which involves endochondral and intramembranous ossification processes [92, 99]. Endochondral bone formation refers to bone formed through the ossification of intermediate cartilage tissue, which is transformed into woven bone. Intramembranous ossification describes bone formation within fibrous connective tissues, and occurs in the absence of cartilage. The endochondral and intramembranous ossification pathways employed to heal bone are also responsible for formation of bones during fetal development.

1.7.3 Remodeling

Eventually, the hard callus consists of entirely woven bone tissue that is converted to regular bone structure by osteoblast and osteoclast cells through the remodeling mechanism described previously. Following remodeling processes, the cortical and cancellous architecture and function of the bone is restored.

1.8 BONE RELATED BIOMATERIALS APPLICATIONS

Biomaterials related to bone are employed to repair and regenerate the skeleton when it is compromised by trauma, illness and/or age-related diseases in scenarios and natural healing processes alone are unable to replenish tissue and restore function. These materials interact with the body

directly in the form of an external system or implanted material or device to repair or replace bone.

1.8.1 Bone graft

The “self-healing” ability of bone means small defects can be replenished by new bone formation in response to the injury. However, not all defects will heal in this manner, instead being filled in with a fibrous tissue [100]. The minimal size of a bone defect that will not heal by itself naturally is defined as a critical size defect [100].

Critical size defects may arise following the traumatic loss of bone, or tissue excision to remove an infected bone region, as well as benign and cancerous growths. The surgeon is left with a defect that is typically irregular and the size of which is difficult to predict prior to surgery. The formation of this fibrous tissue will weaken the overall structure of the bone and may result in permanent deformity. These defects must be augmented with suitable material to prevent fibrous ingress into the defect whilst contributing a degree of biomechanical stability.

Bone regeneration materials need to be able to provide a scaffold capable of facilitating the healing of bone in scenarios that include fractures, large defects, and cavities resulting from the removal of bone tumors, as well as the fusing of adjacent vertebrae in the spine, whilst avoiding the development of fibrous tissues.

Biomaterials are used in every reconstructive orthopedic surgical operation [101]. Bone grafts are biomaterials that can augment a defect or

void space of bone. Bone grafts provide orthopedic surgeons with tools for adjunctive fixation between bony tissues, such as where bone healing and filling of bone defects is sought. Bone grafts that provide a scaffold onto which newly forming hard tissue can be deposited are referred to as being osteoconductive. Osteoinductive materials can additionally stimulate bone formation through physical or chemical cues (e.g. release of growth factors) in a non-bony site. Additionally, these materials must also be well tolerated by the body (i.e. biocompatible), ideally resorbed, cost-effective, easily stored, as well as easy to apply in the clinical setting.

1.8.2 Bone fusion

Bone fusion is used as a means to prevent the specific pathologies that are associated with damage to the spinal column. In order to alleviate conditions concerning nerve root compression, arthrodesis of the spine, colloquially referred to as spinal fusion, is an acceptable treatment option when more preservative treatment measures are ruled out. Following the removal of compromised vertebral disc material, a spinal cage device is inserted into the disc space, restoring the spacing between vertebrae and relieving pressure upon trapped nerve roots.

In addition to facilitating the fusion of adjacent vertebrae, the spinal cage maintains correct alignment and foraminal height of the spine. A successful procedure results in the alleviation of pain suffered by the patient, however the mobility of the spine is never fully recovered. Moreover, other

issues include cage subsidence, dislocation, and deviation from normal lordosis.

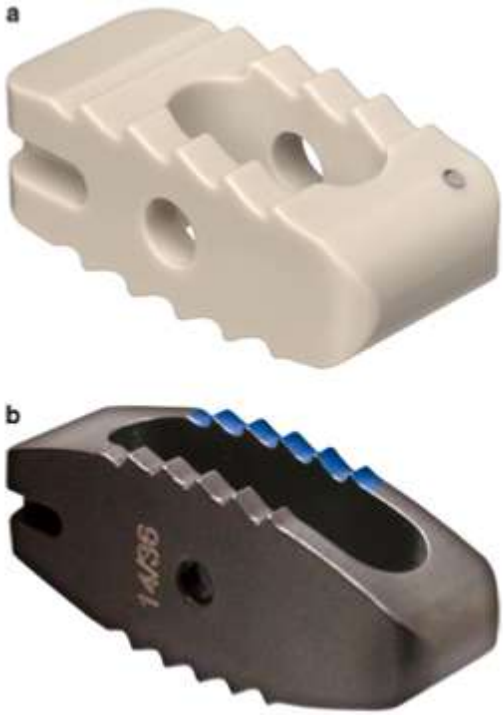

Figure 1.7 Bullet shaped spinal fusion cages designed for lumbar vertebral fusion fabricated from (a) PEEK and (b) titanium (Adapted from [102] with permission from Copyright © 2014 Springer-Verlag Berlin Heidelberg).

Spinal fusion devices have been in clinical use since the 1990's [103]. These devices were first shown to be successful in the treatment of horses suffering from nerve root compression [104]. In humans, incorrect sizing of a fusion device can lead to poor clinical results, despite achieving fusion, due to incorrect lordosis of the spine [105]. Therefore, fusion devices are specifically designed for use in different localities of the spine, such as for lumbar or cervical implantation [102, 106].

Conventional spinal fusion devices are fabricated from non-resorbing biomaterials such as poly(ether ether ketone) (PEEK) or titanium based alloy (e.g. Ti6Al4V), and typically incorporate a cavity space to accommodate for bone grafting material (Figure 1.7). A bone graft of choice may then be packed in by the surgeon, which when in contact with the bony surfaces of vertebra, aids in fusion and complete through growth of new bone. The 'gold standard' for decades has been autologous graft, which facilitates successful fusion with at least 90 % rate of success [107]. Alternatively some devices may be designed to accept pre-fabricated bone graft inserts that can be readily placed into the fusion device before implantation, such as Tribone 80 for the Solis cervical cage system, consisting of β-TCP (80%) and HA (20%) [108].

1.9 BIOMATERIALS FOR BONE REPAIR

Several classes of materials are widely employed for the replacement and regeneration of bone tissue and facilitating bone fusion, including tissue derived, ceramic, polymeric, composite and metallic materials.

1.9.1 Tissue derived biomaterials

1.9.1.1 Autograft

The long-standing 'gold standard' bone augmentation material is autologous bone. Autograft has been shown to outperform other tissue derived and synthetic bone graft materials based on histological comparison of new bone formation [109].

This bone graft is native to the patients themselves, and is taken from a second surgical site, typically the iliac crest. Employment of autologous bone removes concerns relating to immunological rejection. Requirement for a secondary surgical procedure, adds to additional surgery time and potential for blood loss, which can bring further pain and discomfort to the patient, as well as putting them at risk of contracting infection.

Cortical bone graft is typically associated with poor cellular ingress and limited vascular ingress due to dense structuring [110]. Alternatively, autograft that exhibits structure similar to cancellous bone can facilitate cellular ingress and vascularisation due to the porous architecture of trabecular tissue, which provides an intricate 3D scaffold for bone formation [110].

In some cases, surgeons may be limited by the availability and morbidity of bone that can be taken. Removing autologous tissue would likely cause further deterioration to the condition of a patient suffering with osteoporosis as it would increase their risk of fracture. Moreover, elderly as well as osteoporotic bone may possess deficient osteogenic potential needed for bone healing. Attention has therefore shifted toward the development and employment of alternative bone augmenting materials.

1.9.1.2 Allograft

Allograft is bone that is also human derived but has been harvested from another person, typically deceased, and is therefore acquired from a tissue bank [111]. This tissue derived bone graft has been demonstrated as a suitable alternative to autologous graft material in both orthopedic and

craniofacial surgeries [112-114]. Benefits include good availability and avoidance of further surgery to acquire grafting material.

Forms of allograft include fresh, frozen and freeze-dried, which provide osteoconductive scaffolds for bone formation [115, 116]. Due to time required for disease screening and sterility procedures, fresh allograft is seldom employed. Frozen grafts are maintained below temperatures of -60 ^{o}C, which suspends enzymatic degradation of the material. Freeze-dried allografts include freeze-dried bone allograft (FDBA) and demineralised freeze-dried bone allograft (DFDBA), which has been stripped of calcium phosphate content, leaving being a material consisting of collagen, non-collagenous proteins and bone growth promoting factors (e.g. bone morphogenic proteins (BMPs)) [115]. Mineral content is removed with hydrochloric acid treatment to produce a demineralized bone matrix (DBM) [111]. Being in possession of bone growth promoting agents, including growth factors and proteins, means DFDBA is considered to possess osteoinductive properties in addition to being osteoconductive [111, 116].

Tissue banks provide powdered forms of DFDBA that range in particle size between 250-750 μm [116]. DFDBA particulates of 100-300 μm have been shown to be more osteogenic compared to larger particles of 1000-2000 μm, as demonstrated through enhanced healing of femur fractures in Rhesus monkeys [117]. This may be due to the increased surface area of smaller particles, which facilitates greater interaction with cells involved in bone formation.

Concerns with bone allograft include the risk of disease transmission (e.g. HIV), expensive processing costs, and potential toxicity of chemical remnants present after de-calcification [115].

1.9.1.3 Xenograft

Xenograft refers to tissue originating from another species, such as bovine or porcine derived bone, and is also inclusive of mineralised corals and algae. Issues with these materials includes cross species disease transmittance and ethical concerns [118, 119].

Commercial xenograft products, including blocks and powdered forms, are void of organic components to help reduce negative immune response following implantation [115]. Examples of a commercially available xenograft include bovine derived Bio-Oss®, and coral derived Pro-Osteon®. Despite not being wholly resorbed *in vivo*, Bio-Oss® facilitates substantial bone ingrowth [120]. Pro-Osteon® can achieve significantly higher bone ingrowth compared to DBM bone graft, demonstrated in a rabbit femoral defect model [121].

Xenograft offers a cheaper alternative to allograft that is just as effective. For the treatment of calcaneal fractures, equine derived xenograft was shown to perform as well as allograft bone tissue [122].

1.9.2 Ceramic biomaterials

For bone graft applications, much attention has focused on ceramic materials that are chemically comparable to the inorganic mineral found in bone. Many inorganic calcium based salts have been used for the

augmentation of hard tissues. Concerns regarding disease transmission are eliminated in synthetic forms of these materials, which are synthesised in specialist laboratories as opposed to being harvested from a biological donor.

1.9.2.1 Bioglass

Since the discovery of Bioglass by Hench et al. in 1971, various types of biomaterials containing $CaO\text{-}SiO_2$ have been investigated as biomaterials for hard tissue repair or replacement [123]. The element silicon is an important trace element in the early stages of bone formation. The soluble form of silicon may contribute to the stimulation of type I collagen synthesis and osteoblastic differentiation in human osteoblast-like cells [124]. It is shown that biomaterials containing $CaO\text{-}SiO_2$ have excellent bioactivity and can bond to both hard and soft tissues through the development of a biologic apatite layer on the surface of the implanted material [125].

1.9.2.2 Calcium phosphates

Calcium phosphates include hydroxyapatite (HA) ($Ca_{10}(PO_4)_6(OH)_2$), α- and β- phases of tricalcium phosphate (TCP) (α-/β- $Ca_3(PO_4)_2$), brushite or dicalcium phosphate dihydrate (DCPD) ($CaHPO_4.2H_2O$), and calcium deficient hydroxyapatite (CDHA) ($Ca_9(HPO_4)(PO_4)_5OH$), which are reported to be well tolerated by the body and provide an osteoconductive scaffold, or osteoinductive platform (depending on the inclusion of bone promoting factors) for the regeneration of bone [126]. Table 1.2 provides a summary of calcium phosphate phases.

Table 1.2 Calcium phosphate phase compositions and their solubility's (Adapted from [127] with permission from Copyright © 2008 American Chemical Society).

Molecular formula	Molecular mass (g mol^{-1})	Ca:P	-log (K_{sp}) at 25°C [128]	Common names
$Ca(H_2PO_4)_2$	234.05	0.5	Very soluble	Monocalcium phosphate anhydrous (MCPA)
$Ca(H_2PO_4)_2.H_2O$	252.07	0.5	Very soluble	Monocalcium phosphate monohydrate (MCPM)
$CaHPO_4$	136.1	1	6.90	Monetite, dicalcium phosphate anhydrate (DCPA)
$CaHPO_4.2H_2O$	172.1	1	6.59	Brushite, dicalcium phosphate dihydrate (DCPD)
$Ca_8(HPO_4)_2(PO_4)_4.5H_2O$	982.5	1.3	96.6	Octacalcium phosphate (OCP)
α-$Ca_3(PO_4)_2$	310.2	1.5	25.5	Alpha-tricalcium phosphate (α-TCP)
β-$Ca_3(PO_4)_2$	310.2	1.5	28.9	Beta-tricalcium phosphate (β-TCP)
$Ca_{10}(PO_4)_6(OH)_2$	1004.6	1.67	116.8	Hydroxyapatite (HA)
$Ca_4(PO_4)_2O$	366.3	2	38.0	Tetra-calcium phosphate (TTCP)

$Ca_xH_y(PO_4)_z.nH2O$ (n = 3-4.5)	Formula dependent	1.2-2.2	Very soluble	Amorphous calcium phosphate (ACP)

The soluble nature of some calcium phosphates results in their dissolution and subsequent resorption following implantation. Calcium and phosphate ions are the primary dissolution products, which may be utilised in the formation of new bone mineral. The solubility of calcium phosphates correlates to the Ca/P ratio. Generally, the lower the Ca/P, the higher the solubility of the calcium phosphate phase in water at 25^{o}C. Calcium phosphate solubility decreases in the order MCPA=MCPM>DCPD>DCPA>OCP>α-TCP>β-TCP >HA.

1.9.2.3 Calcium sulphate

Additionally, calcium sulphate (CS) based phases are a safe and cheap alternative to calcium phosphate that exists in three main forms, including fully hydrated ($CaSO_4.2H_2O$), partly hydrated ($CaSO_4.0.5H_2O$), and fully anhydrous ($CaSO_4$). These phases are also referred to as dihydrate, hemihydrate and anhydrite CS respectively, which exist as sub forms summarised in Table 1.3.

Since its first use *in vivo* in 1892 by Dressmann to treat tuberculous osteomyelitis, CS has been used for filling bone defects [131]. In the 1950's, Peltier demonstrated use of CS to repair large bone defects, including that of the tibiae of dogs [132]. The treated area displayed new bone formation. This work demonstrated CS is partially or completely resorbed with no foreign body reaction elicited, indicating it is well tolerated by local tissues *in vivo*. Peltier

and Jones used CS to fill cavities left over from removal of bone cysts [133]. The patients discussed had cavities filled with CS pellets, which were absorbed and replaced by new bone. Minimal side effects were reported. Early CS reports should be treated with caution due to variance of reported outcomes, possibly from inconsistent crystal structure, purity and CS quality being assessed at the time [134].

Table 1.3 Calcium sulphate phase compositions and their solubility's (+ Common names used in biomaterial literature, * Metastable in dry air, **Stable between 40-1180^{o}C, ***Stable at >1180 ^{o}C) (Adapted from [129] with permission from Copyright © 2015 Taylor & Francis).

Molecular formula	**Molecular mass (g mol^{-1})**	**Forms**	**-log (K_{sp}) at 25^{o}C [130]**	**Common names**
$CaSO_4.2H_2O$	172.2	n/a	4.5	Calcium sulphate dihydride^{+} Gypsum^{+} Raw Gypsum Byproduct gypsum Hardened gypsum
$CaSO_4.0.5H_2O$	145.1	Alpha* Beta*	6.5	Calcium sulphate hemihydrate^{+} Plaster of Paris^{+} Alpha Alpha form Alpha plaster Alpha hemihydrate

				Beta Beta form Beta plaster Beta Hemihydrate
$CaSO_4$	136.1	Anhydrate III* Stages: Beta anhydrite III Beta anhydrite III' Alpha anhydrite III Anhydrate II** Stages: AII-s (slowly soluble) AII-u (insoluble) AII-E (Estrich gips) Anhydrate I***	4.3	Calcium sulphate anhydrite^{+}

1.9.2.4 Calcium silicate

Calcium silicate has been well known as the main component in Portland cement, but has only two decades of history as a biomaterial. Depending on Ca/Si molar ratio, there are three kinds of calcium silicate: monocalcium silicate ($CaSiO_3$, MCS), dicalcium silicate (Ca_2SiO_4, C_2S), and tricalcium silicate (Ca_3SiO_5, C_3S). C_2S and C_3S, which are the main components of Portland cement, are hydraulic and can be hydrated and hardened when mixed with a liquid phase. C_2S have been known to have five polymorphs, designated by using the symbols α, α'H, α'L, β and γ.

Calcium silicate cements have attracted attention in the field of bone or dental repair and drug delivery since they showed good biocompatibility, bioactivity, excellent marginal adaptation and sealing ability [135, 136].

1.9.2.5 Pre-sets

Bioceramic compositions have been employed as both granules and pellets to fill critical sized defects, which are supplied as pre-set materials that may be readily implanted. Granules are often pre-fabricated particles of millimeter scale. Irregular packing can lead to migration from the implant site.

Pre-set CS poses minimal risk of *in vivo* side effects [137, 138]. However, it has been reported that severe inflammation is experienced in 20% of patients when treated with OSTEOSET®T pellets [139-142]. The relatively short time frame it takes CS to undergo *in vivo* dissolution could lead to inflammation from resulting calcium rich fluids. Transient hypercalcemia is an expected side effect [143]. Further research has attributed these

complications to impurities. Similar CS OSTEOSET® pellets were used by Stubbs *et al.,* with no inflammation [144]. Wilkins *et al.,* report of 50 patients treated with CS OSTEOSET® pellets; no complications arose [145].

1.9.2.6 Cements

Calcium phosphate, sulphate and silicate can form cement. Cements overcome migration issues as they can be applied as a paste that fills the defect entirely followed by hardening to provide both mechanical and biological functions. Typically, one or more cement precursors are mixed with solvent in which they are not thermodynamically stable. Reactants subsequently dissolve and the salt most stable at that stoichiometry and pH value is usually precipitated, hardening to form a solid cement matrix.

The credit for the formulation of the first calcium phosphate cement applicable for use in the clinical setting is rightly given to Brown and Chow of the Paffenbarger Dental Institute [146]. These researchers observed that combinations of tetracalcium phosphate (TTCP) ($Ca_4(PO_4)_2O$) and brushite, or dicalcium phosphate dihydrate (DCPD) ($CaHPO_4.2H_2O$), intended for use as a remineralising paste hardened when allowed to stand on the laboratory bench overnight. In years prior to this, other researchers including Monma had identified that the combination of calcium phosphate salts such as α-tricalcium phosphate (α-TCP) (α-$Ca_3(PO_4)_2$) with water formed a hardened product [147]. Despite the findings, these researchers did not report the first calcium phosphate cement in the modern literature. Indeed, in his seminal paper in 1950, Kingery demonstrated that the combination of CaO and H_3PO_4

enabled the formation of a hardened product that consisted of monocalcium phosphate monohydrate (MCPM) ($Ca(H_2PO_4)_2.H_2O$) [148]. The soluble and acidic nature of this compound would not have made this material useful for biomedical application.

The majority of the early work on calcium phosphate cements focused on the optimisation and application of apatite forming materials; the rationale being that apatite is the main constituent of bone mineral and the hardening of this material, in contrast to brushite cements, does not require the use of acidic pH values. Modern calcium phosphate cements harden to form one of only two products, as determined by kinetic and thermodynamic factors heavily influenced by pH [48, 127]. If the cement paste has a pH value > 4.2, hydroxyapatite (HA) ($Ca_{10}(PO_4)OH_2$) or more likely the calcium deficient form of the salt ($Ca_9(PO_4)_5HPO_4OH$) is favoured and if the cement has a pH < 4.2, brushite or dicalcium phosphate dihydrate (DCPD) ($CaHPO_4.2H_2O$) is favoured, which under certain conditions may dehydrate to form monetite, otherwise known as dicalcium phosphate anhydrate (DCPA) ($CaHPO_4$) [149-151].

Adding water to an anhydrous form of CS will rapidly lead to the solution becoming supersaturated with $CaSO_4.2H_2O$, which precipitates out via crystal nucleation and growth, which continues until a point below saturation. A cycle of dissolution and precipitation repeats, eventually resulting in a solid material consisting of hydrated CS [152]. Setting time is relatively fast. Korte and Brouwers have modeled CS hydration to provide more understanding of this mechanism [153]. Setting kinetics can be

quickened or disrupted by additives termed accelerators and retardants respectively [154].

1.9.3 Polymeric biomaterials

Both naturally occurring and synthetic polymers can be applied to bone repair applications. Synthetic polymers have many key advantages in a range of applications as biomaterials due to their tunable physical, chemical and degradation properties.

1.9.3.1 Polymeric hydrogels

Polymeric hydrogels are highly hydrated structures on to which cells may adhere or be encapsulated within, serving as a 3D scaffold for tissue formation. Owing to high water content and tissue-like structuring, hydrogels are attractive regenerative materials for several tissues, including skin, cartilage and bone [155]. Both fabricated forms and injectable formulations have been researched, covering biomaterials applications including bone grafting and anti-scarring wound dressings [94, 156].

Cell adhesion upon hydrogel surfaces is dependent upon interrelated factors including surface chemistry, surface energy, surface charge density, and surface topology [157]. Poly(ethylene glycol) (PEG), an FDA approved hydrogel for medical applications, is surprisingly cell adhesion resistant. The inclusion of adhesion promoting molecules in the bulk of the gel, attachment of such molecules to the gel surface, and modification of surface topology have been investigated to enhance cell attachment to PEG based gels [158].

Cell encapsulation is generally achieved by the gelation a liquid precursor containing a suspension of cells, with conditions being benign toward the biological components within, avoiding cytotoxicity [157]. Gelation mechanisms based on radical polymerisation and chemical crosslinking are widely employed in the encapsulation of many cell types (e.g. chondrocytes, fibroblasts, and stem cells etc.), in various gel networks (e.g. chitosan, alginate-co-gelatin, PEG, hyaluronic acid etc.) [157].

Hydrogels are dynamic structures that exhibit swelling and diffusion dependent on the surrounding environment. Such properties can be influenced by ionic and pH gradients, and furthermore may be exploited to control the release kinetics of soluble therapeutics and ionic species [159]. Ion exchange processes can facilitate biologically relevant mineralisation reactions between calcium and phosphate ion species either side of the gel/solution interface, promoting the formation of mineral either within or from the surface of hydrogel. These processes have extended the application of hydrogels for the fabrication of potential bone graft biomaterials, such as the formation of tubular calcium phosphate structures from calcium loaded agar gel in contact with phosphate solution [160, 161].

Typically, most hydrogels are limited by weak mechanical properties, which are essential to muskoskeletal load bearing applications. To overcome this, bioactive ceramic particles can be added to hydrogel matrices to enhance strength, as well as improving bone cell adhesion [94, 162, 163].

1.9.3.2 Poly(methyl methacrylate (PMMA)

Poly(methyl methacrylate (PMMA) is commonly employed as a fixative, its primary purpose to facilitate the transfer of mechanical loadings from bone to implant prosthesis. It was first used in 1958 in a total hip replacement operation [164]. This material does not form a direct bond with bone, relying on mechanical interlocking [165]. Strategies to improve integration with bone include the addition of bioactive particulates such as HA [166].

PMMA is a cementitious polymer that dissolves in its own monomer, a liquid MMA component, before hardening [165]. It can therefore be injected directly into defect spaces. There are concerns regarding toxicity of reaction products and its exothermic setting reaction, which can generate temperatures of 90 ^{o}C or greater whilst in close contact with tissue leading to potential tissue necrosis [167].

1.9.3.3 Poly(ether ether ketone) (PEEK)

Poly(ether ether ketone) (PEEK) is a semi crystalline engineering polymer. The polymer belongs to a family of poly(aryl ether ketone)s (PAEKs). Other structures within the PAEK family also include poly(ether ketone) (PEK) and poly(ether ketone ketone) (PEKK). These polymers are distinguishable by their chemical structure consisting of chains of benzyl ether and benzyl aldehyde subunits in specific arrangements (Figure 1.8).

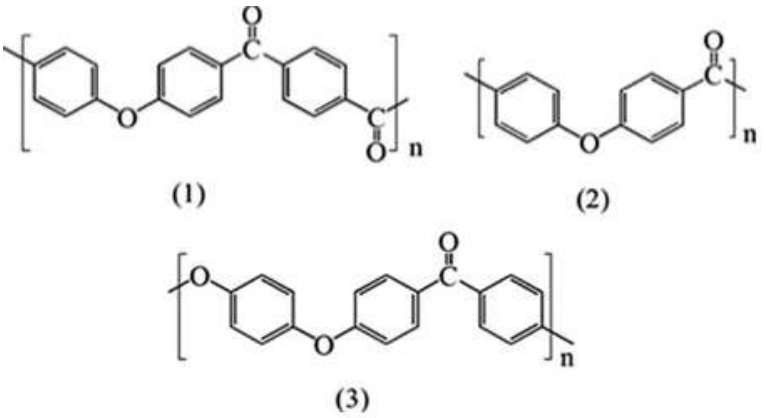

Figure 1.8 Polymeric repeat units of some poly(aryl ether ketone)s, including (1) Poly(ether ketone ketone) (PEKK), (2) Poly(ether ketone) (PEK), and (3) Poly(ether ether ketone) (PEEK) (Adapted from [168] with permission from Copyright © 2012 Taylor and Francis).

The use of PEEK is widespread. It has been used in industries such as aerospace, oil & gas, automotive, electronic, energy and medical applications due to its impressive properties, such as thermostability, and resistance to degradation when in prolonged contact many organic solvents [168]. Over recent decades, PEEK has become an increasingly important and relied upon biomaterial for the medical sector, particularly in bone regeneration applications, seeing extended use in orthopedic, maxillofacial and, spinal surgeries [169, 170].

PEEK is physically ideal for the role of spinal implants, exhibiting physical properties, such as modulus, close to that of bone (3 GPa to 4 GPa), as well being well tolerated by the body [169]. It has also been proven in this application in both animal models and humans [106, 171-175]. Despite this,

alternative metallic counterparts, such as titanium alloy (Ti6Al4V), have been shown to outperform PEEK in terms of fusion capability.

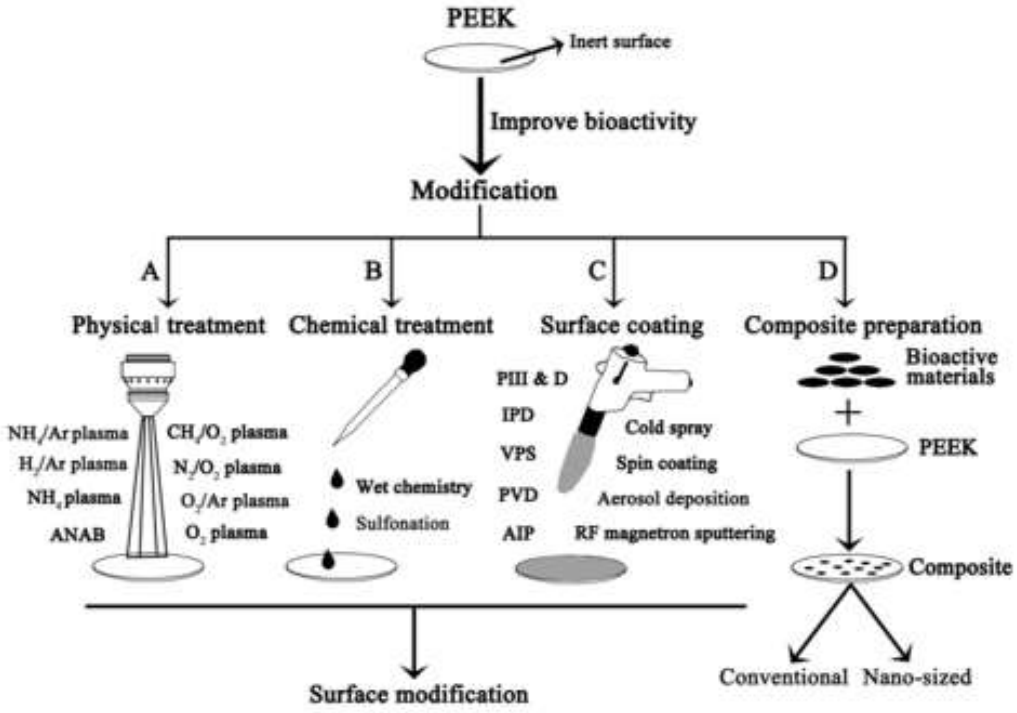

Figure 1.9 Overview of techniques used to enhance the bioactivity of PEEK (Adapted from [176] with used under the Creative Commons Attribution License (CC BY 3.0)).

Novel processing, surface treatments and composite formulations have therefore been applied to PEEK to enhance its bioactive properties (Figure 1.9). In the case of PEEK spinal fusion devices, applying these chemical, physical and compositional alterations may improve the interaction of the polymer with bone, improving tissue integration and fusion efficacy [176].

1.9.4 Composites

Advancements in materials engineering now frequently allow for the combination of polymer and ceramic materials into a single composite formulation. Composites have the potential to possess the sum of favourable properties that originate from the constituent phases.

Composites are an interesting prospect for biomedical applications. Blending a polymer with bioactive particles can engender a typically inert material with bioactive properties through the addition of the secondary bioactive phase. These formulations are developed to enhance adherence with adjacent bone tissue. It is therefore possible to improve on the properties of a given polymer through blending with a bioactive ceramic material such as HA. Whilst this can improve biocompatibility, it is potentially at a cost to the strength of the polymer if a high volume fraction of a brittle phase is added [169].

1.9.4.1 Carbon fiber reinforced PEEK

Carbon fiber reinforced PEEK (CFR_PEEK) has been successfully applied as spinal rods and cages. In the role of spinal cages, CFR_PEEK achieves high rates of fusion and is rarely associated with negative complications, including subsidence and neurological issues [177].

Commercial carbon fibre reinforced PEEK is available from several manufactures, including Invibio®, who market it under the trade name CFR PEEK-OPTIMA® [178].

1.9.4.2 Hydroxyapatite reinforced PEEK

The addition of HA to inert PEEK can produce a bioactive composite material (HA_PEEK). HA exposed on the surface of HA_PEEK contributes to increasing bioactivity [179]. As a reflection of the bioactivity properties HA introduces, apatite has been shown to develop on the surface of HA_PEEK submerged in simulated body fluid (SBF) [180]. HA particulates surrounded by polymeric matrix and not exposed on the surface do not contribute to apatite formation [181]. Compared to unfilled PEEK, HA_PEEK has been shown to enable better integration with surrounding bone [182]. Design considerations for polymer composites include polymer orientation, the interface between filler and polymer, loading level, morphology, orientation, and size [183].

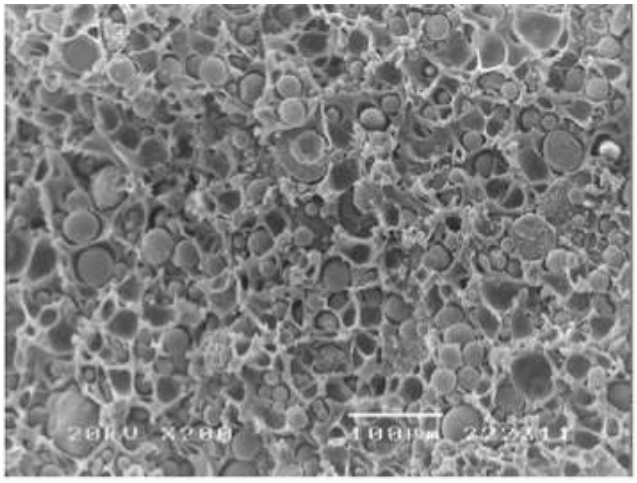

Figure 1.10 Fracture surface of a 20 vol% HA_PEEK composite specimen that shows evidence of HA particulate debonding from the PEEK matrix (Adapted from [182] with permission from Copyright © 2003 Elsevier Science Ltd)

Inclusion of bioactive HA particulates from between 2.5 to 7.5 vol% to PEEK can provide a slight improvement to mechanical attributes. However,

increasing the bioactivity of composites by the addition of greater loadings of bioactive particulates results in a trade-off in mechanical properties. At HA loadings > 10 vol %, the tensile properties are severely compromised due to HA particle debonding [179, 182] (Figure 1.10).

Additions of high weight fractions of bioceramic particles in a polymeric matrix can result in a brittle material, diminishing mechanical performance of such composites. In the absence of strong interfacial interactions between the bioceramic and polymer matrix, forces are unable to transfer effectively between brittle additive and the surrounding ductile matrix, causing the particulates to act as stress-raisers. Indeed, HAPEX^{TM}, a 40 % HA in 60 % high density polyethylene blend, is brittle due to high amount of filler, however, it is only bioactive at 40 % HA incorporation [184]. Moreover, high levels of HA incorporation can result in the formation of filler particle agglomerates, which display weak interactions at the polymer filler interface [179, 182].

Therefore, improving the strength of the interface between the HA and PEEK polymeric matrix beyond simple mechanical interlocking should enable the production of a stronger composite material at greater HA loadings.

1.9.5 Metallic biomaterials

Metals have the longest history amongst modern biomaterials and are generally used for replacement of hard tissues [185].

Metallic plates were first employed for the fixation of long bones over a century ago [186, 187]. Metals continue to be used as biomedical screws and

fixative aids in orthopaedic surgery. Because of their high strength and stiffness, metallic biomaterials are also routinely employed in replacement and repair applications associated with high biomechanical stresses, such as hip replacement, knee replacement and spinal fusion [188, 189].

Common metal and metal alloys for used for biomaterials application includes stainless steel, cobalt alloys, and titanium alloys (e.g. Ti6Al4V).

1.9.5.1 Stainless steel

A combination of mechanical properties, corrosion resistance and cost effectiveness means stainless steel is a desired material for fixation devices [190]. It possesses a high ductility compared to other metallic biomaterials, which makes it an ideal candidate for forming bone plates [191].

1.9.5.2 Cobalt alloys

The first cobalt-based alloys were found to resist degradation within an oral environment and so were used for dental implants [192]. Cobalt alloys are currently utilised in prosthesis of the knee, shoulder and hip [192]. However, there is growing body of evidence that the release of cobalt wear debris from metal-on-metal implants has adverse consequences toward adjacent tissues and potentially introduces cytotoxic levels of cobalt ions into the bloodstream [193, 194].

1.9.5.3 Titanium and titanium alloys

Titanium plates and screws are commonly employed as implant fixation aids [190]. The unalloyed metal is very biocompatible and rarely initiates allergic reactions when inside the body [195].

Titanium alloys were developed in order to improve upon the properties of titanium to ultimately improve an implant's longevity and performance. Ti6Al4V is considered a dominant titanium alloy in the biomedical field (Ratner, 2004). The pro-osteogenic potential of Ti6Al4V coatings and titanium foams is highly promising for developing more effective spinal fusion devices [196, 197].

In fact, compared to PEEK polymer surfaces, both smooth and roughened Ti6Al4V surfaces have been shown to stimulate the secretion of bone morphogenic proteins (BMPs) 2, 4, and 7 at significantly high levels from human MG63 osteoblast-like cells. These molecules promote the development of an osteogenic bone-forming environment [196].

1.10 THESIS OVERVIEW

In this thesis, several calcium based composite biomaterials will be developed for bone graft and spinal fusion applications. Each chapter will disseminate the formulation and characterisation of the systems. The main body of the thesis consists of four research chapters that are presented as published papers or papers in submission (Chapters 2 through to 5).

Chapter 2 is titled "Characterisation of novel poly (ether ether ketone)/calcium sulphate composite for bone augmentation" and will focus on

the reinforcement of biomedical calcium sulphate (CS) cement for use as a bone graft material. Chapter 3 is titled “Biologically analogous calcium phosphate tubes from a chemical garden” and will investigate the interface between calcium loaded agar based hydrogel and phosphate solutions that is able to produce tubular calcium phosphate structures. Chapter 4 is titled “Interfacial mineral fusion and tubule entanglement as a means to harden a bone augmentation material” and will explore the formulation of a bone graft technology that is able to harden *in situ* through generating biologically analogous tubular calcium phosphate structures introduced in Chapter 3. Chapter 5 is titled “Development of a covalently bonded hydroxyapatite and poly(ether ether ketone) composite” and will explore the development of a covalently linked PEEK and hydroxyapatite (HA) composite material for spinal fusion devices.

Lastly, Chapter 6 provides an account of the overall conclusions of the research, and provides avenues for further work in order to build upon the findings.

1.11 REFERENCES

1. Dimitriou R, Jones E, McGonagle D, Giannoudis PV. Bone regeneration: current concepts and future directions. BMC medicine. 2011;9:66.

2. United Nations. World Population Prospects - The 2017 Revision. Website: https://www.un.org/development/desa/publications/world-population-prospects-the-2017-revision.html

3. HM Government. Healthy Lives, Healthy People: Our strategy for public health in England. 2010. Website: https://www.gov.uk/government/publications/healthy-lives-healthy-people-our-strategy-for-public-health-in-england

4. International Osteoporosis Foundation. Facts and Statistics. 2015. Website: https://www.iofbonehealth.org/facts-statistics

5. Arthritis Research UK. Arthritis Information Data and Statistics. 2017. Website: https://www.arthritisresearchuk.org/arthritis-information/data-and-statistics.aspx

6. Rosemont IL. Musculoskeletal injuries report: incidence, risk factors and prevention. American Academy of Orthopedic Surgeons, 2000.

7. Aitken S, Court-Brown CM. The epidemiology of sports-related fractures of the hand. Injury. 2008;39(12):1377-83.

8. Rubin G, Peleg K, Givon A, Rozen N. Upper extremity fractures among hospitalized road traffic accident adults. The American Journal of Emergency Medicine. 2015;33(2):250-3.

9. Warren MP. Health issues for women athletes: exercise-induced amenorrhea. J Clin Endocrinol Metab. 1999;84:1892.

10. Lin JT, Lane JM. Osteoporosis: A Review. . Clinical Orthopaedics & Related Research. 2004;425:126-34.

11. Nation Osteoporosis Society. The Osteoporosis Agenda England. 2015. Website: https://nos.org.uk/media/1959/agenda-for-osteoporosis-england-final.pdf

12. Riggs BL, Melton LJ. The worldwide problem of osteoporosis: insights afforded by epidemiology. Bone. 1995;17(5):505-11.

13. Department of Health Do. Fracture prevention services - An economic evaluation. 2009. Website: http://www.cawt.com/Site/11/Documents/Publications/Population%20Health/Economics%20of%20Health%20Improvement/fractures.pdf

14. Medtronic. Degenerative Disc Disease. 2002. Website: http://www.medtronic.com/downloadablefiles/InFuse%20-%20Degenerative%20Disc%20Disease%20Fact%20Sheet.pdf

15. National institute for health and care excellence. Low back pain and sciatica. 2013. Website: https://www.nice.org.uk/guidance/ng59/documents/low-back-pain-and-sciatica-final-scope2

16. Jordan JL, Konstantinou K, O'Dowd J. Herniated lumbar disc. BMJ Clinical Evidence. 2011;2011:1118.

17. Mitchell PJ. Fracture Liaison Services: the UK experience. Osteoporosis International. 2011;22(3):487.

18. Farmer RP, Herbert B, Cuellar DO, Hao J, Stahel PF, Yasui R, et al. Osteoporosis and the orthopaedic surgeon: basic concepts for successful co-management of patients' bone health. International Orthopaedics. 2014;38(8):1731-8.

19. Lindsay R, Pack S, Li Z. Longitudinal progression of fracture prevalence through a population of postmenopausal women with osteoporosis. Osteoporosis International. 2005;16(3):306-12.

20. Kanis JA, McCloskey EV, Johansson H, Cooper C, Rizzoli R, Reginster JY, et al. European guidance for the diagnosis and management of osteoporosis in postmenopausal women. Osteoporosis International. 2013;24(1):23-57.

21. British Heart Foundation. Active for later life. 2006. Website: http://www.laterlifetraining.co.uk/wp-content/uploads/2017/08/BHFAFLLPDFSec1.pdf 22. Brooke-Wavell K, Jones PRM, Hardman AE, Tsuritani I, Yamada Y. Commencing, Continuing and Stopping Brisk Walking: Effects on Bone Mineral Density, Quantitative Ultrasound of Bone and Markers of Bone Metabolism in Postmenopausal Women. Osteoporosis International. 2001;12(7):581-7.

23. Bonaiuti D, Shea B, Iovine R, Negrini S, Welch V, Kemper HHCG, et al. Exercise for preventing and treating osteoporosis in postmenopausal women. Cochrane Database of Systematic Reviews. 2002(2).

24. Karlsson M. Has exercise an antifracture efficacy in women? Scandinavian Journal of Medicine & Science in Sports. 2004;14(1):2-15.

25. Sato Y, Iwamoto J, Kanoko T, Satoh K. Amelioration of Osteoporosis and Hypovitaminosis D by Sunlight Exposure in Hospitalized Elderly Women With Alzheimer's Disease: A Randomized Controlled Trial. Journal of Bone and Mineral Research. 2015;30(9):1745-.

26. McCombs JS, Thiebaud P, McLaughlin-Miley C, Shi J. Compliance with drug therapies for the treatment and prevention of osteoporosis. Maturitas. 2004;48(3):271-87.

27. Leal J, Gray AM, Prieto-Alhambra D, Arden NK, Cooper C, Javaid MK, et al. Impact of hip fracture on hospital care costs: a population-based study. Osteoporosis International. 2016;27(2):549-58.

28. McCrory DC, Turner DA, Patwardhan MB, Richardson WJ. Spinal Fusion for Treatment of Degenerative Disease Affecting the Lumbar Spine Agency for Healthcare Research and Quality, 2006.

29. Porter RW. Should one operate on the elderly spine? . In: Hukins DWL, Nelson M, editors. The Ageing Spine: Manchester University Press; 1987.

30. NICE. Hip fracture: Management - Costings report 2017.

31. Colaço HB, Shah Z, Back D, Davies A, Ajuied A. (iv) Xenograft in orthopaedics. Orthopaedics and Trauma. 2015;29(4):253-60.

32. Svedbom A, Hernlund E, Ivergård M, Compston J, Cooper C, Stenmark J, et al. Osteoporosis in the European Union: a compendium of country-specific reports. Archives of Osteoporosis. 2013;8(1-2):137.

33. Osteoporosis Canada. General Information On Pain After A Fracture. 2017. Website: https://osteoporosis.ca/bone-health-osteoporosis/living-with-the-disease/after-the-fracture/general-information-about-pain-after-a-fracture/

34. Boos N. The impact of economic evaluation on quality management in spine surgery. Eur Spine J. 2009;18 Suppl 3:338-47.

35. Clarke B. Normal Bone Anatomy and Physiology. Clinical Journal of the American Society of Nephrology : CJASN. 2008;3(Suppl 3):S131-S9.

36. Rodan GA. Bone homeostasis. Proceedings of the National Academy of Sciences of the United States of America. 1998;95(23):13361-2.

37. Nawawi AN, Alqap ASF, Sopyan I. Recent Progress on Hydroxyapatite-Based Dense Biomaterials for Load Bearing Bone Substitutes. Recent Patents on Materials Science 2011;4(1):63-80.

38. Tzaphlidou M. Bone Architecture: Collagen Structure and Calcium/Phosphorus Maps. Journal of Biological Physics. 2008;34(1-2):39-49.

39. Hadjidakis DJ, Androulakis II. Bone Remodeling. Annals of the New York Academy of Sciences. 2006;1092(1):385-96.

40. Wegst UGK, Bai H, Saiz E, Tomsia AP, Ritchie RO. Bioinspired structural materials. Nature Materials. 2014;14(1):23-36.

41. Ricard-Blum S, Ville G. Collagen Cross-Linking. Int J Biochem. 1989;21(11):1185-9.

42. Wegst UGK, Ashby MF. The mechanical efficiency of natural materials. Philosophical Magazine. 2004;84(21):2167-86.

43. de Jong WF. La substance minerale dans les os. Recl Trav Chim Pays – Bas Belg. 1926;45:445-8.

44. Roseberry HH, Hastings AB, Morse JK. X-ray analysis of bone and teeth. J Biol Chem 1931;90:395–407.

45. Ibrahim DM, Mostafa AA, Korowash SI. Chemical characterization of some substituted hydroxyapatites. Chemistry Central Journal. 2011;5:74-.

46. Driessens FCM. The mineral in bone, dentin and tooth enamel. Bulletin des Sociétés Chimiques Belges. 1980;89(8):663-89.

47. Bigi A, Cojazzi G, Panzavolta S, Ripamonti A, Roveri N, Romanello M, et al. Chemical and structural characterization of the mineral phase from

cortical and trabecular bone. Journal of Inorganic Biochemistry. 1997;68(1):45-51.

48. Johnsson MS, Nancollas GH. The role of brushite and octacalcium phosphate in apatite formation. Critical reviews in oral biology and medicine : an official publication of the American Association of Oral Biologists. 1992;3(1-2):61-82.

49. Querido W, Rossi AL, Campos APC, Rossi AM, Farina M. Does crystallinity of extracted bone mineral increase over storage time? Materials Research. 2013;16(5):970-4.

50. Racila M, Crolet JM. Nano and Macro Structure of Cortical Bone: Numerical Investigations. Mechanics of Advanced Materials and Structures. 2007;14(8):655-63.

51. Landis WJ, Song MJ, Leith A, McEwen L, McEwen BF. Mineral and Organic Matrix Interaction in Normally Calcifying Tendon Visualized in Three Dimensions by High-Voltage Electron Microscopic Tomography and Graphic Image Reconstruction. Journal of Structural Biology. 1993;110(1):39-54.

52. Stock SR. The Mineral-Collagen Interface in Bone. Calcif Tissue Int. 2015;97(3):262-80.

53. Nudelman F, Pieterse K, George A, Bomans PHH, Friedrich H, Brylka LJ, et al. The role of collagen in bone apatite formation in the presence of hydroxyapatite nucleation inhibitors. Nat Mater. 2010;9(12):1004-9.

54. Andrea Di L, Alessia L, Giuseppe C, Carlos M, Clemens van B, Lorenzo M. Toward mimicking the bone structure: design of novel hierarchical

scaffolds with a tailored radial porosity gradient. Biofabrication. 2016;8(4):045007.

55. Georgiadis M, Muller R, Schneider P. Techniques to assess bone ultrastructure organization: orientation and arrangement of mineralized collagen fibrils. J R Soc Interface. 2016;13(119).

56. Weiner S, Traub W, Wagner HD. Lamellar bone: structure-function relations. J Struct Biol. 1999;126(3):241-55.

57. Maggiano IS, Maggiano CM, Clement JG, Thomas CDL, Carter Y, Cooper DML. Three-dimensional reconstruction of Haversian systems in human cortical bone using synchrotron radiation-based micro-CT: morphology and quantification of branching and transverse connections across age. Journal of Anatomy. 2016;228(5):719-32.

58. Florencio-Silva R, Sasso GRdS, Sasso-Cerri E, Simões MJ, Cerri PS. Biology of Bone Tissue: Structure, Function, and Factors That Influence Bone Cells. BioMed Research International. 2015;2015:421746.

59. Caetano-Lopes J, Canhão H, Fonseca JE. Osteoblasts and bone formation. Órgão Oficial da Sociedade Portuguesa de Reumatologia - Acta Reum Port. 2007;32:103-10.

60. Schaffler MB, Kennedy OD. Osteocyte Signaling in Bone. Current Osteoporosis Reports. 2012;10(2):118-25.

61. van Bezooijen RL, Roelen BAJ, Visser A, van der Wee-Pals L, de Wilt E, Karperien M, et al. Sclerostin Is an Osteocyte-expressed Negative Regulator of Bone Formation, But Not a Classical BMP Antagonist. The Journal of Experimental Medicine. 2004;199(6):805-14.

62. Boyce BF, Rosenberg E, de Papp AE, Duong LT. The osteoclast, bone remodelling and treatment of metabolic bone disease. European Journal of Clinical Investigation. 2012;42(12):1332-41.

63. Raggatt LJ, Partridge NC. Cellular and Molecular Mechanisms of Bone Remodeling. The Journal of Biological Chemistry. 2010;285(33):25103-8.

64. Cao Y, Zhou Z, de Combrugghe B, Nakashima K, Guan H, Duan X, et al. Osterix, a Transcription Factor for Osteoblast Differentiation, Mediates Antitumor Activity in Murine Osteosarcoma. Cancer Res 2005;65(4):1124-8.

65. Komori T. Regulation of Osteoblast Differentiation by Runx2. In: Choi Y, editor. Osteoimmunology: Interactions of the Immune and skeletal systems II. Boston, MA: Springer US; 2010. p. 43-9.

66. Bodine PVN, Komm BS. Wnt signaling and osteoblastogenesis. Reviews in Endocrine and Metabolic Disorders. 2006;7(1):33-9.

67. Komori T, Yagi H, Nomura S, Yamaguchi A, Sasaki K, Deguchi K, et al. Targeted Disruption of Cbfa1 Results in a Complete Lack of Bone Formation owing to Maturational Arrest of Osteoblasts. Cell. 1997;89(5):755-64.

68. Boyce BF, Xing L. Functions of RANKL/RANK/OPG in bone modeling and remodeling. Arch Biochem Biophys. 2008;473(2):139-46.

69. Klein-Nulend J, Nijweide PJ, Burger EH. Osteocyte and bone structure. Current Osteoporosis Reports. 2003;1(1):5-10.

70. Väänänen HK, Laitala-Leinonen T. Osteoclast lineage and function. Archives of Biochemistry and Biophysics. 2008;473(2):132-8.

71. Henriksen K, Tanko LB, Qvist P, Delmas PD, Christiansen C, Karsdal MA. Assessment of osteoclast number and function: application in the

development of new and improved treatment modalities for bone diseases. Osteoporos Int. 2007;18(5):681-5.

72. Boissy P, Saltel F, Bouniol C, Jurdic P, Machuca-Gayet I. Transcriptional Activity of Nuclei in Multinucleated Osteoclasts and Its Modulation by Calcitonin. Endocrinology. 2002;143(5):1913-21.

73. Roodman GD. Paget's disease and osteoclast biology. Bone. 1996;19(3):209-12.

74. Sims NA, Martin TJ. Coupling the activities of bone formation and resorption: a multitude of signals within the basic multicellular unit. BoneKEy reports. 2014;3.

75. Yoshiya T, Shingo N, Yosuke O. Osteoblasts and Osteoclasts in Bone Remodeling and Inflammation. Current Drug Targets - Inflammation & Allergy. 2005;4(3):325-8.

76. Burr DB. Targeted and nontargeted remodeling. Bone. 2002;30(1):2-4.

77. Martin RB. Targeted bone remodeling involves BMU steering as well as activation. Bone. 2007;40(6):1574-80.

78. Martínez-Reina J, Reina I, Domínguez J, García-Aznar JM. A bone remodelling model including the effect of damage on the steering of BMUs. Journal of the mechanical behavior of biomedical materials. 2014;32:99-112.

79. Delaisse J-M. The reversal phase of the bone-remodeling cycle: cellular prerequisites for coupling resorption and formation. BoneKEy reports. 2014;3:561.

80. Ferrier J, Xia S-L, Lagan E, Aubin JE, Heersche JNM. Displacement and translocation of osteoblast-like cells by osteoclasts. Journal of Bone and Mineral Research. 1994;9(9):1397-405.

81. Redey SA, Razzouk S, Rey C, Bernache-Assollant D, Leroy G, Nardin M, et al. Osteoclast adhesion and activity on synthetic hydroxyapatite, carbonated hydroxyapatite, and natural calcium carbonate: relationship to surface energies. J Biomed Mater Res. 1999;45(2):140-7.

82. Henriksen K, Bollerslev J, Everts V, Karsdal MA. Osteoclast Activity and Subtypes as a Function of Physiology and Pathology—Implications for Future Treatments of Osteoporosis. Endocrine Reviews. 2011;32(1):31-63.

83. Wenisch S, Stahl JP, Horas U, Heiss C, Kilian O, Trinkaus K, et al. In vivo mechanisms of hydroxyapatite ceramic degradation by osteoclasts: Fine structural microscopy. Journal of Biomedical Materials Research Part A. 2003;67A(3):713-8.

84. Sly WS, Hewett-Emmett D, Whyte MP, Yu YS, Tashian RE. Carbonic anhydrase II deficiency identified as the primary defect in the autosomal recessive syndrome of osteopetrosis with renal tubular acidosis and cerebral calcification. Proceedings of the National Academy of Sciences of the United States of America. 1983;80(9):2752-6.

85. Delaisse JM, Andersen TL, Engsig MT, Henriksen K, Troen T, Blavier L. Matrix metalloproteinases (MMP) and cathepsin K contribute differently to osteoclastic activities. Microscopy research and technique. 2003;61(6):504-13.

86. Hattner R, Epker BN, Frost HM. Suggested Sequential Mode of Control of Changes in Cell Behaviour in Adult Bone Remodelling. Nature. 1965;206(4983):489-90.

87. Boyce BF, Hughes DE, Wright KR, Xing L, Dai A. Apoptosis in Bone Cells. In: Russell RGG, Skerry TM, Kollenkirchen U, editors. Novel Approaches to Treatment of Osteoporosis. Berlin, Heidelberg: Springer Berlin Heidelberg; 1998. p. 61-82.

88. Lind M, Deleuran B, Thestrup-Pedersen K, Søballe K, Eriksen EF, Bunger C. Chemotaxis of human osteoblasts. APMIS. 1995;103:140-6.

89. Kini U, Nandeesh BN. Physiology of Bone Formation, Remodeling, and Metabolism. 2012:29-57.

90. Pazzaglia UE, Congiu T, Sibilia V, Quacci D. Osteoblast-osteocyte transformation. A SEM densitometric analysis of endosteal apposition in rabbit femur. J Anat. 2014;224(2):132-41.

91. Young B, Lowe JS, Stevens A, Heath JW. Wheater's Functional Histology: A Text and Colour Atlas: Elsevier Health Sciences; 2006.

92. Betz O, Vrahas M, Baltzer A, Lieberman JR, Robbins PD, Evans CH. Gene Transfer Approaches to Enhancing Bone Healing. 2005:157-68.

93. Einhorn TA. The Cell and Molecular Biology of Fracture Healing. Clin Orthop Relat Res 1998;355 Suppl:S7-21.

94. Tozzi G, De Mori A, Oliveira A, Roldo M. Composite Hydrogels for Bone Regeneration. Materials. 2016;9(4):267.

95. Victoria G, Petrisor B, Drew B, Dick D. Bone stimulation for fracture healing: What's all the fuss? Indian Journal of Orthopaedics. 2009;43(2):117-20.

96. Einhorn TA. Enhancement of fracture-healing. The Journal of Bone and Joint Surgery American volume. 1995;77(6):940-56.

97. Marzona L, Pavolini B. Play and players in bone fracture healing match. Clinical Cases in Mineral and Bone Metabolism. 2009;6(2):159-62.

98. Feghali CA, Wright TM. Cytokines in acute and chronic inflammation. Frontiers in bioscience : a journal and virtual library. 1997;2:d12-26.

99. Sfeir C, Ho L, Doll BA, Azari K, Hollinger JO. Fracture Repair. In: Lieberman JR, Friedlaender GE, editors. Bone Regeneration and Repair: Biology and Clinical Applications. Totowa, NJ: Humana Press; 2005. p. 21-44.

100. Spicer PP, Kretlow JD, Young S, Jansen JA, Kasper FK, Mikos AG. Evaluation of bone regeneration using the rat critical size calvarial defect. Nat Protocols. 2012;7(10):1918-29.

101. Pape HC, Evans A, Kobbe P. Autologous Bone Graft: Properties and Techniques. Journal of Orthopaedic Trauma. 2010;24.

102. Nemoto O, Asazuma T, Yato Y, Imabayashi H, Yasuoka H, Fujikawa A. Comparison of fusion rates following transforaminal lumbar interbody fusion using polyetheretherketone cages or titanium cages with transpedicular instrumentation. Eur Spine J. 2014;23(10):2150-5.

103. Emstad E, del Monaco DC, Fielding LC, Block JE. The VariLift(®) Interbody Fusion System: expandable, standalone interbody fusion. Medical Devices (Auckland, NZ). 2015;8:219-30.

104. Bagby GW. Arthrodesis by the distraction-compression method using stainless steel implant. Orthopedics 1988;11(6):931-4.

105. Liao JC, Niu CC, Chen WJ, Chen LH. Polyetheretherketone (PEEK) cage filled with cancellous allograft in anterior cervical discectomy and fusion. Int Orthop. 2008;32(5):643-8.

106. Mastronardi L, Ducati A, Ferrante L. Anterior cervical fusion with polyetheretherketone (PEEK) cages in the treatment of degenerative disc disease. Preliminary observations in 36 consecutive cases with a minimum 12-month follow-up. Acta neurochirurgica. 2006;148(3):307-12; discussion 12.

107. Sandhu HS, Grewal HS, Parvataneni H. Bone Grafting For Spinal Fusion. Orthopedic Clinics of North America. 1999;30(4):685-98.

108. Stryker. Solis Cervical Cage Surgical Technique. 2011. Website: http://vd-services.website.bg/storage/produkti/solis%20OpTech.pdf

109. Athanaslou VT, Papachristou DJ, Panagopoulos A, Saridis A, Scopa CD, Megas P. Histological comparison of autograft, allograft-DBM, xenograft, and synthetic grafts in a trabecular bone defect: An experimental study in rabbits. Med Sci Monit. 2010;16(1):24-31.

110. Roberts TT, Rosenbaum AJ. Bone grafts, bone substitutes and orthobiologics: the bridge between basic science and clinical advancements in fracture healing. Organogenesis. 2012;8(4):114-24.

111. Kumar P, Vinitha B, Fathima G. Bone grafts in dentistry. Journal of Pharmacy & Bioallied Sciences. 2013;5(Suppl 1):S125-S7.

112. Salyer KE, Gendler E, Menendez JL, Simon TR, Kelly KM, Bardach J. Demineralized perforated bone implants in craniofacial surgery. The Journal of craniofacial surgery. 1992;3(2):55-62.

113. Muscolo DL, Ayerza MA, Aponte-Tinao LA. Massive Allograft Use in Orthopedic Oncology. Orthopedic Clinics of North America. 2006;37(1):65-74.

114. Vangsness CT, Jr., Garcia IA, Mills CR, Kainer MA, Roberts MR, Moore TM. Allograft transplantation in the knee: tissue regulation, procurement, processing, and sterilization. The American journal of sports medicine. 2003;31(3):474-81.

115. Figueiredo A, Silva O, Cabrita S. Inflammatory reaction post implantation of bone graft materials. Experimental Pathology and Health Sciences. 2012;6(1):15-8.

116. Grover V, Kapoor A, Malhotra R, Sachdeva S. Bone allografts: A review of safety and efficacy. Indian Journal of Dental Research. 2011;22(3):496-.

117. Shapoff CA, Bowers GM, Levy B, Mellonig JT, Yukna RA. The effect of particle size on the osteogenic activity of composite grafts of allogeneic freeze-dried bone and autogenous marrow. Journal of periodontology. 1980;51(11):625-30.

118. McCarthy CR. Ethical Aspects of Animal-to-Human Xenografts. ILAR Journal. 1995;37(1):3-9.

119. Hughes J. Xenografting: ethical issues. Journal of Medical Ethics. 1998;24:18-24.

120. Schlegel AK, Donath K. BIO-OSS--a resorbable bone substitute? Journal of long-term effects of medical implants. 1998;8(3-4):201-9.

121. Leupold JA, Barfield WR, An YH, Hartsock LA. A comparison of ProOsteon, DBX, and collagraft in a rabbit model. J Biomed Mater Res B Appl Biomater. 2006;79(2):292-7.

122. Sonmez MM, Armagan R, Ugurlar M, Eren T. Allografts versus Equine Xenografts in Calcaneal Fracture Repair. The Journal of Foot and Ankle Surgery. 2017;56(3):510-3.

123. Li X, Shi J, Zhu Y, Shen W, Li H, Liang J, et al. A template route to the preparation of mesoporous amorphous calcium silicate with high in vitro bone-forming bioactivity. J Biomed Mater Res B Appl Biomater. 2007;83(2):431-9.

124. Ding S-J, Shie M-Y, Wang C-Y. Novel fast-setting calcium silicate bone cements with high bioactivity and enhanced osteogenesis in vitro. Journal of Materials Chemistry. 2009;19(8):1183-90.

125. Chen Q, Miyaji F, Kokubo T, Nakamura T. Apatite formation on PDMS-modified CaO–SiO2–TiO2 hybrids prepared by sol–gel process. Biomaterials. 1999;20(12):1127-32.

126. Dorozhkin SV. Calcium orthophosphate bioceramics. Ceramics International. 2015;41(10):13913-66.

127. Wang L, Nancollas GH. Calcium Orthophosphates: Crystallization and Dissolution. Chemical Reviews. 2008;108(11):4628-69.

128. Chow LC. Next generation calcium phosphate-based biomaterials. Dent Mater J. 2009;28(1):1-10.

129. Hughes E, Yanni T, Jamshidi P, Grover LM. Inorganic cements for biomedical application: calcium phosphate, calcium sulphate and calcium silicate. Advances in Applied Ceramics. 2015;114(2):65-76.

130. Lide DR, editor. CRC Handbook of Chemistry and Physics. 87th ed: CRC Press/Taylor and Francis Group; 2006.

131. Dressmann H. Ueber Knockenplombierung bei Hohlenforming Defekten des Knochens. Beitr Klin Chir. 1892;9:804-10.

132. Peltier LF, Bickel EY, Lillo R, Thein MS. The Use of Plaster of Paris to Fill Defects in Bone. Annals of Surgery. 1957;146(1):61-9.

133. Peltier LF, Jones RH. Treatment of unicameral bone cysts by curettage and packing with plaster-of-Paris pellets. The Journal of Bone & Joint Surgery. 1978;60(6):820.

134. Nilsson M, Wang JS, Wielanek L, Tanner KE, Lidgren L. Biodegradation and biocompatability of a calcium sulphate-hydroxyapatite bone substitute. The Journal of bone and joint surgery British volume. 2004;86(1):120-5.

135. Taddei P, Tinti A, Gandolfi MG, Rossi PL, Prati C. Ageing of calcium silicate cements for endodontic use in simulated body fluids: a micro-Raman study. Journal of Raman Spectroscopy. 2009;40(12):1858-66.

136. Wu J, Zhu Y-J, Chen F, Zhao X-Y, Zhao J, Qi C. Amorphous calcium silicate hydrate/block copolymer hybrid nanoparticles: synthesis and application as drug carriers. Dalton Transactions. 2013;42(19):7032-40.

137. Scarano A, Orsini G Fau - Pecora G, Pecora G Fau - Iezzi G, Iezzi G Fau - Perrotti V, Perrotti V Fau - Piattelli A, Piattelli A. Peri-implant bone

regeneration with calcium sulfate: a light and transmission electron microscopy case report. Implant Dentistry. 2007;16(2):195-203.

138. Kim SG, Yeo Hh Fau - Kim YK, Kim YK. Grafting of large defects of the jaws with a particulate dentin-plaster of paris combination. Oral Surg Oral Med Oral Pathol Oral Radiol Endod. 1999;88(1):22-5.

139. Hing KA, Wilson LF, Buckland T. Comparative performance of three ceramic bone graft substitutes. Spine J. 2007;7(4):475-90.

140. Robinson D, Alk D, Sandbank J, Farber R, Halperin N. Inflammatory reactions associated with a calcium sulfate bone substitute. Annals of transplantation. 1999;4(3-4):91-7.

141. Turner TM, Urban RM, Gitelis S, Haggard WO, Richelsoph K. Resorption evaluation of a large bolus of calcium sulfate in a canine medullary defect. Orthopedics. 2003;26(5 Suppl):s577-9.

142. Dewi AH, Ana ID, Wolke J, Jansen J. Behavior of plaster of Paris-calcium carbonate composite as bone substitute. A study in rats. Journal of biomedical materials research Part A. 2013;101(8):2143-50.

143. Wright Medical Technology I. OSTEOSET® T BONE GRAFT PRODUCTS. 2010.

144. Stubbs D, Deakin M, Chapman-Sheath P, Bruce W, Debes J, Gillies RM, et al. In vivo evaluation of resorbable bone graft substitutes in a rabbit tibial defect model. Biomaterials. 2004;25(20):5037-44.

145. Wilkins RM, Kelly CM, Giusti DE. Bioassayed demineralized bone matrix and calcium sulfate: use in bone-grafting procedures. Annales chirurgiae et gynaecologiae. 1999;88(3):180-5.

146. Finch CA. Acid–base cements: Their biomedical and industrial applications. Polymer International. 1994;35(2):215-.

147. Monma H, Kanazawa T. The hydration of α-tricalcium phosphate. Yogo-kyokai-shi. 1976;84:209-13.

148. Kingery WD. II, Cold-Setting Properties. Journal of the American Ceramic Society. 1950;33(8):242-6.

149. Brown WE, Chow LC. A new calcium phosphate, water setting cement. In: Brown PW, editor. Cements research progress Ohio: Proceedings of The American Ceramic Society 1986 p. 352-79.

150. Hofmann MP. Physikalische Charakterisierung von Calciumphosphat-Pulvern zur Einstellung von Prozessparametern für die Herstellung von Knochenzement: University of Wuerzburg; 2003.

151. Ishikawa K, Takagi S, Chow LC, Suzuki K. Reaction of calcium phosphate cements with different amounts of tetracalcium phosphate and dicalcium phosphate anhydrous. J Biomed Mater Res. 1999;46(4):504-10.

152. Lewry AJ, Williamson J. The setting of gypsum plaster. Journal of Materials Science. 1994;29(23):6085-90.

153. de Korte ACJ, Brouwers HJH, editors. Hydration Modeling of Calcium Sulphates. ICCBT; 2008.

154. Ridge MJ, Surkevicius H. Variations in the kinetics of setting of calcined gypsum. I. Effects of retarders and accelerators. Journal of Applied Chemistry. 1961;11(11):420-7.

155. Nicodemus GD, Bryant SJ. Cell Encapsulation in Biodegradable Hydrogels for Tissue Engineering Applications. Tissue Engineering Part B, Reviews. 2008;14(2):149-65.

156. Hunt NC, Shelton RM, Grover L. An alginate hydrogel matrix for the localised delivery of a fibroblast/keratinocyte co-culture. Biotechnology journal. 2009;4(5):730-7.

157. Thevenot P, Hu W, Tang L. Surface chemistry influences implant biocompatibility. Current topics in medicinal chemistry. 2008;8(4):270-80.

158. Kim D-N, Park J, Koh W-G. Control of cell adhesion on poly(ethylene glycol) hydrogel surfaces using photochemical modification and micropatterning techniques. Journal of Industrial and Engineering Chemistry. 2009;15(1):124-8.

159. Elliott JE, Macdonald M, Nie J, Bowman CN. Structure and swelling of poly(acrylic acid) hydrogels: effect of pH, ionic strength, and dilution on the crosslinked polymer structure. Polymer. 2004;45(5):1503-10.

160. Hughes EA, Williams RL, Cox SC, Grover LM. Biologically Analogous Calcium Phosphate Tubes from a Chemical Garden. Langmuir. 2017;33(8):2059-67.

161. Bjornoy SH, Bassett DC, Ucar S, Andreassen JP, Sikorski P. Controlled mineralisation and recrystallisation of brushite within alginate hydrogels. Biomed Mater. 2016;11(1):015013.

162. Watanabe J, Kashii M, Hirao M, Oka K, Sugamoto K, Yoshikawa H, et al. Quick-forming hydroxyapatite/agarose gel composites induce bone

regeneration. Journal of biomedical materials research Part A. 2007;83(3):845-52.

163. Hu J, Zhu Y, Tong H, Shen X, Chen L, Ran J. A detailed study of homogeneous agarose/hydroxyapatite nanocomposites for load-bearing bone tissue. Int J Biol Macromol. 2016;82:134-43.

164. Charnley J. Anchorage of the femoral head prosthesis to the shaft of the femur. The Journal of bone and joint surgery British volume. 1960;42-B:28-30.

165. Vaishya R, Chauhan M, Vaish A. Bone cement. Journal of Clinical Orthopaedics and Trauma. 2013;4(4):157-63.

166. Chu KT, Oshida Y, Hancock EB, Kowolik MJ, Barco T, Zunt SL. Hydroxyapatite/PMMA composites as bone cements. Bio-medical Materials and Engineering. 2004;14(1):87-105.

167. McMahon S, Hawdon G, Bare J, Sim Y, Bertollo N, Walsh WR. Thermal Necrosis And PMMA - A Cause For Concern? Orthopaedic Proceedings. 2012;94-B(SUPP XXIII)(64).

168. Shukla D, Negi YS, Uppadhyaya JS, Kumar V. Synthesis and Modification of Poly(ether ether ketone) and their Properties: A Review. Polymer Reviews. 2012;52(2):189-228.

169. Kurtz SM, Devine JN. PEEK Biomaterials In Trauma, Orthopedic, And Spinal Implants. Biomaterials. 2007;28(32):4845-69.

170. Panayotov IV, Orti V, Cuisinier F, Yachouh J. Polyetheretherketone (PEEK) for medical applications. J Mater Sci: Mater Med. 2016;27(7):118.

171. Ni J, Zheng Y, Liu N, Wang X, Fang X, Phukan R, et al. Radiological evaluation of anterior lumbar fusion using PEEK cages with adjacent vertebral autograft in spinal deformity long fusion surgeries. Eur Spine J. 2015;24(4):791-9.

172. Roeder RK, Smith SM. Porous And Bioactive PEEK Implants For Interbody Spinal Fusion Advanced materials and processes. 2009:46-8.

173. Ferguson S, Visser JA, Polikeit A. The long-term mechanical integrity of non-reinforced PEEK-OPTIMA polymer for demanding spinal applications: experimental and finite-element analysis. Eur Spine J. 2006;15(2):149-56.

174. Kahraman S, Daneyemez M, Kayali H, Solmaz I, Bedük A, Akay M. Polyetheretherketone (Peek) Cages For Cervical Interbody Replacement: Clinical Experience. Turkish Neurosurgury. 2006;16(3):120-3.

175. Walsh WR, Pelletier MH, Bertollo N, Christou C, Tan C. Does PEEK/HA Enhance Bone Formation Compared With PEEK in a Sheep Cervical Fusion Model? Clin Orthop Relat Res. 2016;474(11):2364-72.

176. Ma R, Tang T. Current strategies to improve the bioactivity of PEEK. Int J Mol Sci. 2014;15(4):5426-45.

177. Heary RF, Kheterpal A, Mammis A, Kumar S. Stackable Carbon Fiber Cages for Thoracolumbar Interbody Fusion After Corpectomy: Long-term Outcome Analysis. Neurosurgery. 2011;68(3):810-9.

178. Pokorný D, Fulín P, Slouf M, Jahoda D, Landor I, Sosna A. Polyetheretherketone (PEEK). Part II: application in clinical practice. Acta Chir Orthop Traumatol Cech. 2010;77(6):470-8.

179. Wang L, Weng L, Song S, Sun Q. Mechanical properties and microstructure of polyetheretherketone–hydroxyapatite nanocomposite materials. Materials Letters. 2010;64(20):2201-4.

180. Yu S, Hariram KP, Kumar R, Cheang P, Aik KK. In vitro apatite formation and its growth kinetics on hydroxyapatite/polyetheretherketone biocomposites. Biomaterials. 2005;26(15):2343-52.

181. Kim IY, Sugino A, Kikuta K, Ohtsuki C, Cho SB. Bioactive composites consisting of PEEK and calcium silicate powders. J Biomater Appl. 2009;24(2):105-18.

182. Abu Bakar MS, Cheng MHW, Tang SM, Yu SC, Liao K, Tan CT, et al. Tensile properties, tension–tension fatigue and biological response of polyetheretherketone–hydroxyapatite composites for load-bearing orthopedic implants. Biomaterials. 2003;24(13):2245-50.

183. Roeder R, Converse G, Kane R, Yue W. Hydroxyapatite-reinforced polymer biocomposites for synthetic bone substitutes. JOM. 2008;60(3):38-45.

184. Di Silvio L, Dalby MJ, Bonfield W. Osteoblast behaviour on HA/PE composite surfaces with different HA volumes. Biomaterials. 2002;23(1):101-7.

185. Niinomi M. Recent metallic materials for biomedical applications. Metallurgical and Materials Transactions A. 2002;33(3):477.

186. Chen Q, Thouas GA. Metallic implant biomaterials. Materials Science and Engineering: R: Reports. 2015;87:1-57.

187. Lane WA. Some Remarks on the Treatment of Fractures. British Medical Journal. 1895;1(1790):861-3.

188. Hermawan H. Introduction to Metallic Biomaterials. In: Hermawan H, editor. Biodegradable Metals: From Concept to Applications. Berlin, Heidelberg: Springer Berlin Heidelberg; 2012. p. 1-11.

189. Geetha M, Singh AK, Asokamani R, Gogia AK. Ti based biomaterials, the ultimate choice for orthopaedic implants – A review. Progress in Materials Science. 2009;54(3):397-425.

190. Frosch K-H, Stürmer KM. Metallic Biomaterials in Skeletal Repair. European Journal of Trauma. 2006;32(2):149-59.

191. Ganesh VK, Ramakrishna K, Ghista DN. Biomechanics of bone-fracture fixation by stiffness-graded plates in comparison with stainless-steel plates. BioMedical Engineering OnLine. 2005;4(1):46.

192. Marti A. Cobalt-base alloys used in bone surgery. Injury. 2000;31:D18-D21.

193. Posada O, Tate R, Meek RM, Grant M. In Vitro Analyses of the Toxicity, Immunological, and Gene Expression Effects of Cobalt-Chromium Alloy Wear Debris and Co Ions Derived from Metal-on-Metal Hip Implants. Lubricants. 2015;3(3):539-68.

194. Jantzen C, Jørgensen HL, Duus BR, Sporring SL, Lauritzen JB. Chromium and cobalt ion concentrations in blood and serum following various types of metal-on-metal hip arthroplasties: A literature overview. Acta Orthopaedica. 2013;84(3):229-36.

195. Pohler OEM. Unalloyed titanium for implants in bone surgery. Injury. 2000;31:D7-D13.

196. Olivares-Navarrete R, Gittens RA, Schneider JM, Hyzy SL, Haithcock DA, Ullrich PF, et al. Osteoblasts exhibit a more differentiated phenotype and increased bone morphogenetic protein production on titanium alloy substrates than on poly-ether-ether-ketone. The spine journal : official journal of the North American Spine Society. 2012;12(3):265-72.

197. Müller U, Imwinkelried T, Horst M, Sievers M, Graf-Hausner U. Do human osteoblasts grow into open-porous titanium? European Cells and Materials. 2006;11:8-15.

Chapter 2. Characterisation of a novel poly (ether ether ketone)/calcium sulphate composite for bone augmentation

Adapted from:

Hughes EAB, Grover LM. Characterisation of a novel poly (ether ether ketone)/calcium sulphate composite for bone augmentation. Biomaterials Research. 2017;21(7).

Authors: Erik A. B. Hughes[1], and Prof. Liam M. Grover[1]

Affiliations: [1]School of Chemical Engineering, University of Birmingham, Edgbaston, B15 2TT, UK

Corresponding author: Prof. Liam Grover (l.m.grover@bham.ac.uk)

2.0 ABSTRACT

2.0.1 Background

Calcium sulphate (CS) has been used in bone grafting since the 1800s. It has not replaced autograft as the gold standard, however, since its dissolution occurs rapidly in bodily fluids, meaning that the material cannot support long-term bone growth. Here, the polymer poly(ether ether ketone) (PEEK) was used to slow dissolution in *in vitro* physiological environments and augment the mechanical properties of the material.

2.0.2 Experimental Methods

PEEK/CS specimens were fabricated by combining powders of PEEK and CS with water, resulting in a hardening paste. To enhance physical interactions between phases, cylindrical specimens were heat-treated to melt and fuse the PEEK. Following analysis of physical and chemical interactions by SEM and FT-IR respectively, dynamic ageing in PBS and compression testing was undertaken to measure how the PEEK influenced the mechanical properties of the final parts. Changes in structure and chemistry were determined using helium pycnometry, SEM and analysis of powder XRD patterns.

2.0.3 Results

Powders of PEEK and CS hemihydrate (CSH) ($CaSO_4.0.5H_2O$) were combined with PEEK at 0 wt%, 2.5 wt%, 20 wt%, 40 wt% and 80 wt% and at a P:L ratio of 0.85 g/mL. The subsequently hardened structures were heat-

treated, which initiated the melting of PEEK and dehydration of CSD ($CaSO_4.2H_2O$) to the CS anhydrite (CSA) ($CaSO_4$) phase, which changed colour and apparent volume. FT-IR and SEM analysis revealed heat treatment of PEEK/CS specimens facilitated both physical and chemical interactions between phases. Over a period of 21 days of ageing in PBS, the hydration of CS was determined by XRD and improved specimen longevity at all levels of PEEK wt% loading was measured compared with the control. Importantly, increasing PEEK wt% loading resulted in a marked increase in the mechanical properties of PEEK/CS specimens in terms of both compressive strength and modulus.

2.0.4 Conclusions

Reinforcement of CS with PEEK significantly enhanced *in vitro* dissolution resistance, in addition to enhancing mechanical properties. This composite therefore has significant future potential as a bone graft replacement.

2.1 INTRODUCTION

Bone graft materials should support the attachment and proliferation of osteoblast cells, and facilitate the deposition of new hard tissue in bone defects [1]. Ideally, these materials allow for the conduction of new mineral deposition and demonstrate good integration with adjacent bony tissues [2]. Increasingly, synthetic minerals are chosen over bone harvested from the patient's own body. This is despite autologous bone graft being considered

the “gold standard” graft material, due to the low risk of immunological rejection associated with its use [3, 4]. The reasons for alternative bone graft selection are that the volume of autologous bone is limited and requires additional surgery to obtain, which poses further risk to a patient in terms of contracting an infection, blood loss and experiencing unnecessary discomfort thereafter [4]. In addition, allograft tissue suffers drawbacks in terms of disease transmission and possible rejection [4].

Synthetic bioceramic materials, particularly calcium (Ca^{2+}) salts of phosphate (PO_4^{3-}), pyrophosphate ($P_2O_7^{4-}$), sulphate (SO_4^{2-}) and silicate (SiO_4^{4-}) are proven examples of minerals that are able to regenerate areas of removed or diseased hard tissue [5-11]. Moreover, these materials can be employed directly and are available in a variety of forms that includes granules and injectable cementitious pastes, allowing surgeons to select the most appropriate product on a case-by-case basis.

The first ceramic material in widespread use for skeletal regeneration was calcium sulphate (CS). The ability of CS to be set *in situ* or applied directly as granules means that the material can be delivered in a number of ways [12, 13]. CS hemihydrate (CSH) ($CaSO_4.0.5H_2O$) and CS anhydrite (CSA) ($CaSO_4$) forms cement when mixed with water, which hardens to form CS dihydrate (CSD) ($CaSO_4.2H_2O$) (Equation 2.1 and 2.2). The interaction between phases is reversible, as the water of crystallization can be removed by heating CSD ($CaSO_4.2H_2O$) (Equation 2.3 and 2.4). CS was first used at the end of the 19^{th} century to provide a fully resorbable osteoconductive scaffold capable of facilitating new bone formation in the diseased tissue of

human tuberculosis sufferers [9]. CS is able to facilitate cavity healing incurred from curettage of bone cysts, as well as being used successfully to augment osteoportic bone to allow for mechanical fixation of pedicle screws [10, 11, 14].

$CaSO_4.0.5H_2O + 1.5H_2O \rightarrow CaSO_4.2H_2O + heat$ (Equation 2.1)

$CaSO_4 + 2H_2O \rightarrow CaSO_4.2H_2O + heat$ (Equation 2.2)

$CaSO_4.2H_2O + heat \rightarrow CaSO_4.0.5H_2O + 1.5H_2O$ (Equation 2.3)

$CaSO_4.2H_2O + heat \rightarrow CaSO_4 + 2H_2O$ (Equation 2.4)

Whilst resorbable graft materials are desirable, CS has been limited in its application since it undergoes rapid dissolution by hydrolytically driven degradation when placed in the body [15-17]. In contrast, biominerals such as hydroxyapatite ($Ca_5(PO_4)_3OH$) (HA) are considerably less soluble in physiological conditions, offering a more stable network to support bone formation [18, 19]. Given that newly forming bone may take several weeks to fill a defect, these more stable calcium phosphate ceramics are favoured over CS for defect augmentation [6, 13].

Strategies to improve the degradation behavior of CS include combination with less soluble mineral phases and additives to form composites that possess enhanced properties. In combination with β-tricalcium phosphate (β-TCP) CS still undergoes dissolution but the calcium phosphate mineral is able to remain at the implant site for a longer period [20].

Composites containing CS can be modified to adjust degradation rate whilst dampening the production of acidic dissolution products [17, 21]. The addition of other phases can also augment the mechanical properties of the graft materials, with previous work showing that HA addition to CS may significantly enhance mechanical properties [22]. Attempts to combine CS with carboxymethylcellulose and hyaluronan improved mechanical properties of the material but at a cost of faster dissolution [23].

It was postulated that combination of CS with an engineering polymer phase could allow for tunable hydrolytic degradation and mechanical attributes without trade-off, extending the capability of CS as a bone graft. One such polymer is poly(ether ether ketone) (PEEK) (Figure 2.1a). PEEK is a high strength, high performance aromatic thermoplastic polymer that is widely considered to cause no detrimental biological response when implanted in the body and is resistant to both hydrolytic and oxidative degradation mechanisms at temperatures far exceeding that required for medical materials within the body [24, 25]. It is utilised widely for load bearing and high-wear resistant medical devices such as spinal implants and acetabular cups [25, 26]. Availability of powdered PEEK means combination with CS powders is a viable strategy for the fabrication of reinforced composites that has not yet been reported. This work describes the production of a composite PEEK/CS material through the combination of PEEK and CS powders prior to hardening and consolidation of the PEEK phase through heating. We describe how the addition of PEEK in this manner modifies the degradation and mechanical properties of the materials.

2.2 EXPERIMENTAL METHODS

2.2.1 Standard fabrication of PEEK/CS cylinders

Double Ground Alpha Base Crystacal (calcium sulphate hemihydrate, CSH) ($CaSO_4.0.5H_2O$) (Saint-Gobain Formula, France) and 150XF PEEK (Victrex, UK) powders were combined with 0 wt%, 2.5 wt%, 20 wt%, 40 wt% and 80 wt% PEEK by mass. Pastes of each mixture were produced under manual stirring with distilled water acquired from an arium® advance EDI pure water system (Sartorius, Germany) at a powder:liquid (P:L) ratio of 0.85 g/mL, before being poured into a mold to create cylindrical specimens of dimensions 12 mm x 6 mm. The mold was then placed upon a Denstar-500 vibrating plate (Denstar, South Korea) set at high frequency to remove air bubbles. After 10 minutes, the mold was transferred to an Incu-line incubator (VWR International, UK) at 37^{o}C. After 1 hour, specimens were carefully removed from the mold and heated at a ramp rate of 5 ^{o}C and held at 380 ^{o}C for 2.5 hours in a CWF 1300 furnace (Carbolite, UK). Specimens were then stored in ambient conditions.

2.2.2 Volumetric shrinkage

Cylinder volume of PEEK/CS specimens (n=3) before heat treatment and following heat treatment was calculated from geometric measurements and % difference determined through calculation (Equation S2.1).

2.2.3 Scanning electron microscopy (SEM)

Secondary electron scanning electron microscopy (SEM) images of the fracture surfaces were obtained using a Sigma FE-SEM (Zeiss, Germany) operating at 15 kV under vacuum. PEEK/CS specimens with fracture surface exposed were secured firmly upon double adhesive carbon tapes attached to aluminium stubs and gold coated under vacuum for 2 minutes using a K550X sputter coater (Quorum Technologies, UK) before images were acquired.

2.2.4 Fourier transform infrared (FT-IR) spectroscopy

Fourier transform infrared spectroscopy between 500 cm^{-1} and 4000 cm^{-1} was undertaken using a Nicolet 380 FT-IR spectrometer (Thermo-Scientific, USA). For sample preparation, 2 mg starting powders and powdered PEEK/CS specimens were mixed with 198 mg KBr (99.99 % trace metals basis, Sigma-Aldrich, UK) and pressed into 13 mm diameter discs using a evacuable pellet die (Specac, UK) under a 10 ton force for 30 seconds with a hydraulic press (Specac, UK).

2.2.5 Dynamic ageing protocol

Ageing was undertaken on n=33 specimens per composition prepared as standard, with a further n=10 specimens per composition not subjected to ageing as a control group. Individual PEEK/CS specimens were submerged in 10 mL of calcium and magnesium free Dulbecco's phosphate buffered saline (PBS) solution (Sigma-Aldrich, UK) in screw cap 60 mL capacity clear vessels. For a fixed set of n=3 specimens, a daily record of PBS supernatant

pH value, wet mass, dry mass, wet height, dry height, wet mid-diameter, dry mid-diameter, wet end-diameter and dry end-diameter was recorded. Supernatant pH values were measured using a S220 SevenCompact™ pH/Ion meter (Mettler Toledo, USA) equipped with InLab Expert Pro-ISM pH electrode (Mettler Toledo, USA). PBS supernatant was drained from every specimen vessel and replenished with a further 10 mL. At 7 day intervals, n=10 specimens per composition were removed from the ageing protocol until day 21.

2.2.6 X-ray diffraction (XRD)

Powder X-ray diffraction (XRD) patterns were acquired using a D8 Autosampler Powder Diffractometer (Bruker, USA) with Cu Kα line (0.154 nm). Data was collected between 5 ^{o} and 60 ^{o} 2θ with a 0.02 ^{o} step-size and a step time of 0.5 s/^{o}. Background signal was removed and intensity normalised for each scan. Patterns were matched to those stored by the International Centre for Diffraction Data (ICDD) database.

2.2.7 Porosity

Apparent specimen density was calculated from geometrical measurements of n=10 heat-treated PEEK/CS specimens before and during ageing. True specimen density was obtained for the same specimens using an AccuPyc II 1340 helium pycnometer (Micrometrics, USA) over 5 cycles of 5 purges. The relative density and porosity were then calculated (Equation S2.2 and S2.3).

2.2.8 Mechanical testing

Prior to mechanical testing, geometrical measurements of PEEK/CS specimen diameter and height were made to allow for calculations of contact area and test start height. Compression tests were undertaken on n=10 specimens per composition with their long-axis perpendicular to the compression platen using a Z030 universal testing rig (Zwick/Roell, USA) equipped with a 50 kN load cell at a compression rate of 2 mm/min until specimen failure. Compressive strength values were determined by converting values of force into stress and plotting stress vs. strain curves from which the maximum value of stress corresponding to specimen failure could be obtained (Equations S2.4 and S2.5)(Figure S2.1). Compressive modulus was determined by obtaining the slope of the aforementioned curves within the elastic region (Equation S2.6)(Figure S2.1).

2.2.9 Statistical analysis

Statistical analysis of data sets was conducted using StatPlus software. One-way ANOVA and post-hoc Tukey honest significant difference (HSD) testing was applied to compare volumetric shrinkage of specimens after heat treatment based on PEEK wt% loading. Two-way ANOVA and post-hoc Tukey HSD testing was applied to compare mechanical data of specimens based on PEEK wt% loading and ageing time. Differences were deemed significant if $p<0.05$.

2.3 RESULTS AND DISCUSSION

2.3.1 Physical and chemical assessment of PEEK/CS cylinders

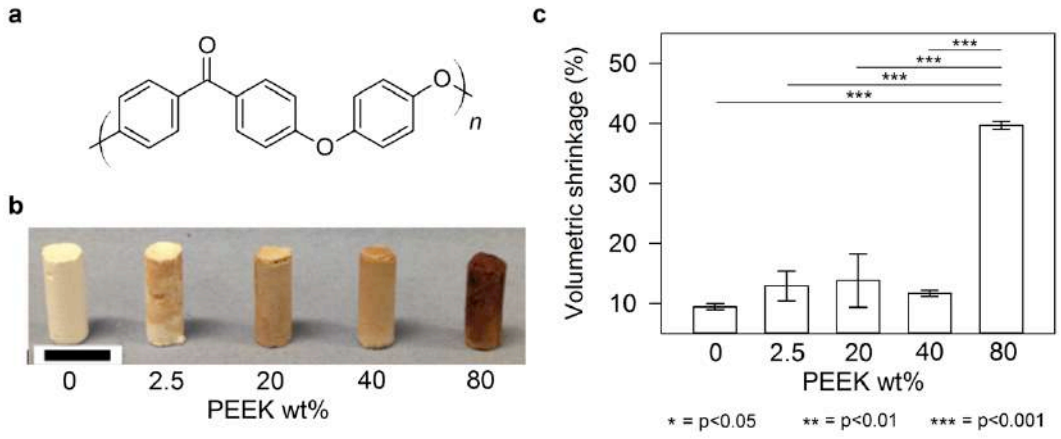

Figure 2.1 (a) Chemical structure of the poly(ether ether ketone) repeat monomer unit. **(b)** PEEK/CS specimens post heat treatment (Scale bar is equal to 10 mm). **(c)** Volumetric shrinkage of PEEK/CS specimens due to heat treatment. Error bars represent standard deviation (n=3) and lines above data columns represent significant differences between groups based on PEEK wt% loading as found by post-hoc Tukey HSD tests following one-way ANOVA analysis.

Following addition of water to starting powders a paste was formed, which hardened to form the composite material in accordance with Equation 2.1. Prior to heat treatment, cylindrical specimens of each composition appeared almost identical up to the point of heat treatment (Figure 2.1b). Heat treatment of PEEK/CS specimens initiated melting of PEEK and dehydration of CSD ($CaSO_4.2H_2O$) to CSA ($CaSO_4$) (Equation 2.4). These changes resulted in an alteration in both colour and apparent volume. Starting

powders of both CSH ($CaSO_4.0.5H_2O$) and PEEK were both cream in colouration. Specimens containing no PEEK (0% PEEK/100%CS) remained similar in appearance after heat treatment. Specimens of 2.5%PEEKCS acquired brown speckles but still retained some cream colouration. Specimens of 20%PEEK/80%CS and 40%PEEK/60%CS became fully brown, whilst specimens of 80%PEEK/20%CS became dark brown. Although the recommended processing temperature for PEEK of 380 ^oC was employed, polymer chain degradation can still occur leading to discoloration, which was evidently more extensive with greater loadings of PEEK (Figure 2.1b).

Volumetric shrinkage of specimens also occurred as a consequence of heat treatment (Figure 2.1c). Specimens with PEEK loading between 0 wt% and 40 wt% underwent a volumetric shrinkage of between approximately 9 % and 15 %. Specimens of 80%PEEK/20%CS however appeared significantly smaller and were confirmed to undergo the greatest extent volumetric shrinkage of 39.7±0.7 %. One-way ANOVA analysis confirmed that significant differences in volumetric shrinkage existed between groups based on PEEK wt% loading ($F(4,10) = 87.3$, $p=9.8x10^{-8}$). Post-hoc analysis utilising Tukey HSD tests found no significant differences between groups with PEEK loading between 0 wt% and 40 wt% ($p>0.05$), however significant differences did exist between these groups and that of specimens loaded with 80 wt% PEEK ($p<0.001$). It is recommended that fractions of CS between 60 to 100 wt% are required to maintain volumetric structure that undergoes no significant geometrical changes as a result of melting PEEK compared to unreinforced material.

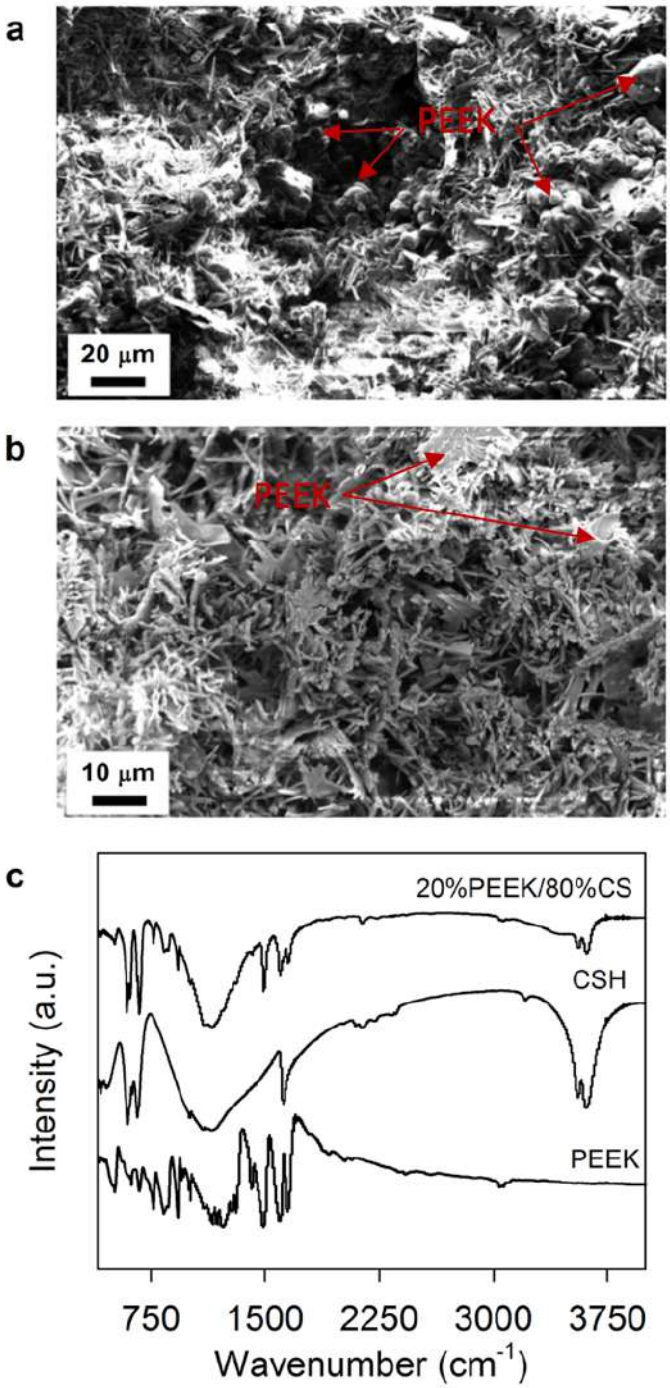

Figure 2.2 SEM micrographs of a fracture surface of a 20%PEEK/80%CS specimen prepared at a P:L ratio of 0.85 g/mL **(a)** prior to heat treatment and **(b)** after heat treatment. **(c)** FT-IR spectra between 500 cm^{-1} and 4000 cm^{-1} wavenumbers of PEEK and CSH ($CaSO_4.0.5H_2O$) starting powders, and a powdered 20%PEEK/80%CS specimen after heat treatment.

Fracture surfaces of a 20%PEEK/80%CS specimen showed good dispersion of globular PEEK particles (approximately 5 μm to 10 μm) situated within a dense network of needles with high aspect ratio (approximately 20 μm by 2 μm) typical of the reported morphology for CSD ($CaSO_4.2H_2O$) (Figure 2.2a). Following heat treatment, there was a change to a more flake-like morphology in addition to needles (Figure 2.2b). The powdered polymeric particles were no longer apparent, since the PEEK phase had fully melted and integrated with CS crystals.

FT-IR spectra of PEEK contained peaks indicative of the chemical moieties present in its chemical structure (Figure 2.1a and 2.2c), including aromatic and carbonyl groups [27-30]. Peaks associated with aromatic groups are located at 3072 cm^{-1} and 3034 cm^{-1} representative of =C-H stretching, and at 1592 cm^{-1} and 1486 cm^{-1} due to C=C stretching. Additional peaks at 850 cm^{-1} and 832 cm^{-1} are indicative of ring deformation vibrational modes. Peaks corresponding to carbonyl groups are found at 1652 cm^{-1}, 1647 cm^{-1} and 1257 cm^{-1}. Due to peak overlap at 1652cm^{-1} and 1647cm^{-1}, separate bands are hard to distinguish, but indicates carbonyl stretching in amorphous and crystalline regions of PEEK respectively.

Vibrational modes of the SO_4^{2-} anion within CSH ($CaSO_4.0.5H_2O$) were identified on the corresponding FT-IR spectrum [31-33] (Figure 2.2c). A peak at approximately 1010 cm^{-1} can be assigned to SO_3^{2-} symmetric stretching. Peaks at 1114 cm^{-1} and 1080 cm^{-1} are assignable to SO_4^{2-} anti-symmetric stretching, whilst peaks at 658 cm^{-1} and 596 cm^{-1} are present due to SO_4^{2-} anti-symmetric bending. Peaks relating to O-H stretching can be found

between 3000 cm^{-1} and 3800 cm^{-1}; peaks in the spectrum of $CaSO_4.0.5H_2O$ are located at 3603 cm^{-1} and 3551 cm^{-1}. A singular O-H vibrational band is also present at 1620 cm^{-1}, indicative of CSH ($CaSO_4.0.5H_2O$) hydration degree.

Vibrational bands relating to both PEEK and SO_4^{2-} anions are present in the spectrum of 20%PEEK/80%CS. The symmetric stretching peak of SO_4^{2-} remains located at approximately 1010 cm^{-1}, consistent with spectra of both CSA ($CaSO_4$) and CSH ($CaSO_4.0.5H_2O$). Substantial reduction of O-H stretching peak intensity between 3000 cm^{-1} and 3800 cm^{-1} indicates dehydration of CS phase as expected (Equation 2.4). The singular O-H vibrational band found at 1620 cm^{-1} in the spectrum of CSH ($CaSO_4.0.5H_2O$) is no longer visible and is instead overlapped by peaks indicative of C=C stretching (1592 cm^{-1}) and carbonyl stretching (1652 and 1647 cm^{-1}) of PEEK polymer chains. Shaping of antisymmetric SO_4^{2-} bending modes between 550 cm^{-1} and 750 cm^{-1}, consisting of 4 overlapping bands (591 cm^{-1}, 612 cm^{-1}, 667 cm^{-1} and 671 cm^{-1}) suggests a mixture of CSA ($CaSO_4$) and CSH ($CaSO_4.0.5H_2O$). Peaks previously assigned within the FT-IR spectrum of PEEK are visible in the spectrum of 20%PEEK/80%CS including ring deformation peaks at 850 cm^{-1} and 832 cm^{-1}, the C=C stretching peak at 1592 cm^{-1} and carbonyl stretching peaks 1652 cm^{-1} and 1647 cm^{-1} appeared at a relatively lower intensity, compared to in the spectrum of PEEK starting powder (Figure 2.2c). Unexpectedly, this suggests PEEK is able to interact with CSA ($CaSO_4$) not only physically, but also chemically through highly

electron rich regions of PEEK polymer, including aromatic rings and carbonyl groups.

2.3.2 Characterisation of dynamically aged PEEK/CS specimens

Fracture surfaces of 20%PEEK/80%CS specimens after ageing in PBS undergo extensive microstructural transformations (Figure 2.3a-c). Ageing promotes development of plate like crystal structures that are visible at Day 7 onwards, indicative of newly forming crystalline phases. This may be due to the hydrating environment provided by PBS media, promoting CS conversion from CSA ($CaSO_4$) to CSD ($CaSO_4.2H_2O$) (Equation 2.2). Crystal structures are surrounded by a polymeric network of PEEK, distinguished by non-crystalline material interacting with crystal structures through both direct contact and coating.

Powder XRD patterns were acquired in order to assess CS phase changes as a consequence of ageing (Figure 2.3d). The powder XRD pattern for PEEK consisted of broad peaks in keeping with PEEK's semi-crystalline nature. Peaks located at 2θ values of 19 °, 21 °, 23 ° and 29 ° are in-keeping with those reported in the literature for PEEK [30]. Sharp and narrow peaks within the CSH ($CaSO_4.0.5H_2O$) pattern indicated a crystalline material that matched to ICDD pattern 01-081-1448. Following heat treatment, the corresponding powder XRD pattern of a 20%PEEK/80%CS specimen contained peaks corresponding to both PEEK and CS phase components, namely CSA ($CaSO_4$) and CSH ($CaSO_4.0.5H_2O$) matching ICDD patterns 01-070-0909 and 01-081-1448 respectively. After 7, 14 and 21 days of ageing,

powder XRD patterns of 20%PEEK/80%CS specimens possessed peaks corresponding to CSD ($CaSO_4.2H_2O$), which were matched to ICDD pattern 00-033-0311, in addition to peaks corresponding to PEEK.

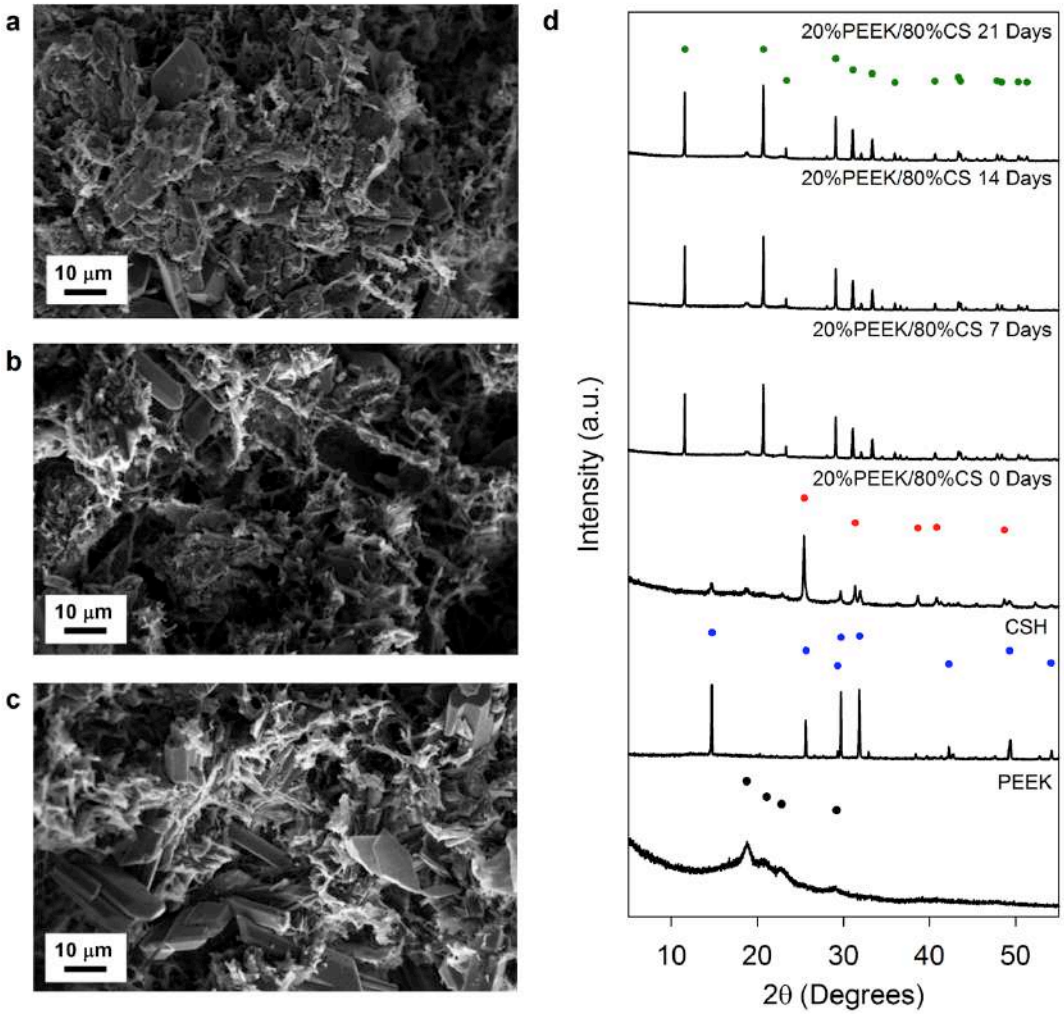

Figure 2.3 SEM images of 20%PEEK/80%CS specimens after ageing in PBS media for **(a)** 7 Days, **(b)** 14 Days and **(c)** 21 Days. **(d)** XRD diffraction patterns between 2θ values of 5 ° and 60 ° of PEEK and CSH ($CaSO_4.0.5H_2O$) starting powders, and powdered 20%PEEK/80%CS specimens after heat treatment prior to ageing (0 Days), and after 7 Days, 14 Days and 21 Days of ageing. An XRD pattern for PEEK from the literature confirmed the crystal structure of the polymer (•, see [30]). ICDD patterns

matching CSH ($CaSO_4.0.5H_2O$) (•, ICDD pattern 01-081-1448), CSA ($CaSO_4$) (•, ICDD pattern 01-070-0909) and CSD ($CaSO_4.2H_2O$) (•, ICDD pattern 00-033-0311) ($CaSO_4.0.5H_2O$, $CaSO_4$ and $CaSO_4.2H_2O$ phases respectively) are also provided to aid in CS phase identification.

Submergence of heat treated PEEK/CS specimens in PBS media initiated an immediate degradation state in specimens loaded with 0 % and 2.5 % PEEK, however a low loading level of 2.5 %, PEEK increased calcium CS longevity overall; complete deterioration of 2.5%PEEK/97.5%CS specimens did not occur until day 17 (Figure S2.2). Mass remaining profiles calculated from dry measurements showed consistent day to day mass loss with regards to 0%PEEK/100%CS and 2.5%PEEK/97.5%CS specimens, equivalent to degradation rates of 14.1 %/day of ageing (r^2 = 0.99) and 7.9 %/day of ageing (r^2 = 0.97) respectively. This resulted in 16.9±5.4 % mass remaining after 6 days and 25.4±15.5 % mass remaining after 9 days of unreinforced PEEK/CS specimens and 2.5 wt% PEEK loaded specimens respectively (Figure 2.4a). In contrast, 20%PEEK/80%CS and 40%PEEK/60%CS specimens increased in mass up to 17.6±1.9 % and 9.7±1.8 % respectively over the course of ageing duration (Figure 2.4a). Deterioration of 20%PEEK/80%CS, 40%PEEK/60%CS and 80%PEEK/20%CS specimens was not evident at any stage of ageing, due to increased physical and chemical interactions between PEEK and CS (Figure S2.2). Interestingly, PEEK reinforcement was shown to facilitate CS phase change from CSA ($CaSO_4$) and CSH ($CaSO_4.0.5H_2O$) to CSD ($CaSO_4.2H_2O$)

leading to a mass increase (Equation 2.1 and 2.2)(Figure 2.3d and 2.4a). Theoretically, from known mass of CSA ($CaSO_4$) consistuting each composite composition, calculations of maximum mass increase due to crystal hydration were 21.2 % for 20%PEEK/80%CS and 15.8 % for 40%PEEK/60%CS specimens, which is consistent with observed increases of 17.6±1.9 % and 9.7±1.8 % respectively. Mass changes experienced by 80%PEEK/20%CS specimens were found to be negligible, and never deviated by more than 0.5 % either side of 100 % of original specimen mass (Figure 2.4a). Simultaneously, between 5 % to 10 % decreases in porosity were measured for 20%PEEK/80%CS, 40%PEEK/60%CS and 80%PEEK/20%CS specimens after 21 days ageing (Table 2.1), possibly arising from crystal hydration of CS and a decrease in microstructure free volume.

Table 2.1 Porosity (%) of PEEK/CS specimens after heat treatment and during ageing (n=10).

Ageing time (Days)	**PEEK content (%)**				
	0	**2.5**	**20**	**40**	**80**
0	70.7±3.15	72.1±0.49	73.9±1.3	73.5±1.6	54.6±3.4
7	-	-	65.8±2.4	67.7±1.4	52.0±3.9
14	-	-	68.0±1.0	68.2±2.9	50.0±2.8
21	-	-	65.9±1.7	66.5±1.4	49.7±3.7

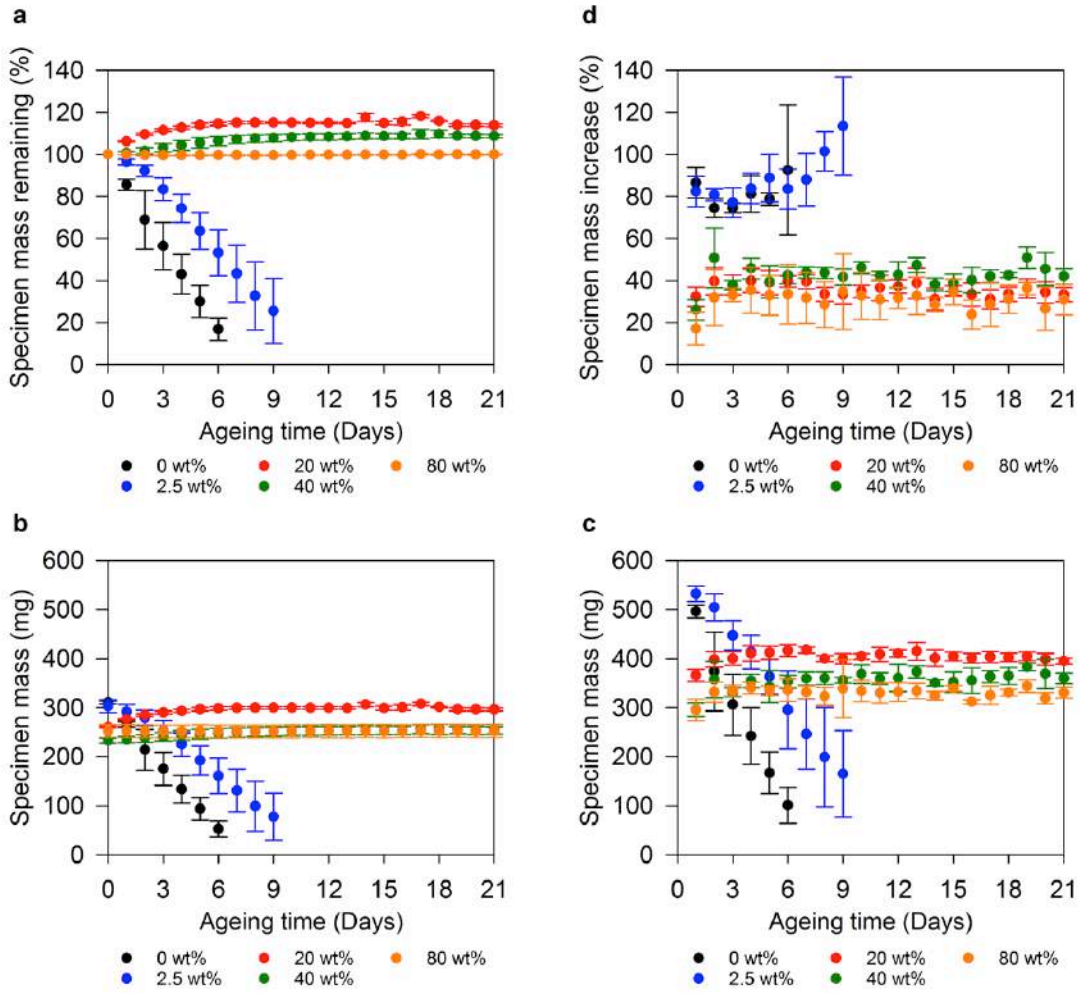

Figure 2.4 (a) PEEK/CS specimen mass remaining expressed as percentage (%) calculated from dry measurements. **(b)** Changes in PEEK/CS specimen mass measured dry and **(c)** wet. **(d)** PEEK/CS specimen mass increase expressed as a percentage (%) calculated between difference in dry and wet mass measurements. Error bars represent standard deviation (n=3).

PEEK/CS specimen mass was consistently greater with regards to wet measurements compared to dry measurements (Figure 2.4b,c). Specimens of 0%PEEK/100%CS and 2.5%PEEK/97.5%CS experienced daily increases in mass averaging 81.3±9.4 % over 6 days and 88.8±10.1 % over 9 days of ageing respectively (Figure 2.4d). Specimens of 20%PEEK/80%CS,

40%PEEK/60%CS and 80%PEEK/20%CS experienced lower average daily increases in mass of 35.7±1.3 %, 42.4±2.8 % and 30.8±3.8 % respectively over 21 days of ageing (Figure 2.4d). Nonetheless, this was considered as a reflection of absorptive capability and porous nature of PEEK/CS specimens, as PEEK/CS specimen height, mid-diameter and end-diameter showed no substantial differences between wet and dry measurements (Figure 2.5a-f). Exploitation of absorbance capacity *in situ* may facilitate localisation of nutrients from adjacent tissues beneficial to osteoblast viability [34]. A feasible avenue of further investigation may be the loading of soluble therapeutics through liquid exchange with PEEK/CS materials to aid bone regeneration [35, 36]. Specimens of 0%PEEK/100%CS and 2.5%PEEK/97.5%CS experienced substantial losses to cylindrical dimensions in terms of height and both mid-diameter and end-diameter.

Direct measurements of PBS pH were indicative of material degradation (Figure 2.6)(Figure S2.2). Specimens of 0%PEEK/100%CS and 2.5%PEEK/97.5%CS lowered PBS pH from 7.4 to between 5 and 6. Such an environment can beneficially demineralise adjacent bone, in-turn releasing growth factors (i.e. bone morphogenic protein) that contribute to mesenchymal cell differentiation into osteoblasts, which may encourage the deposition of new bone [37, 38]. However, rapid 0%PEEK/100%CS and 2.5%PEEK/97.5%CS degradation before bone formation can occur and would be a significant concern that would limit the application of these particular compositions of composite.

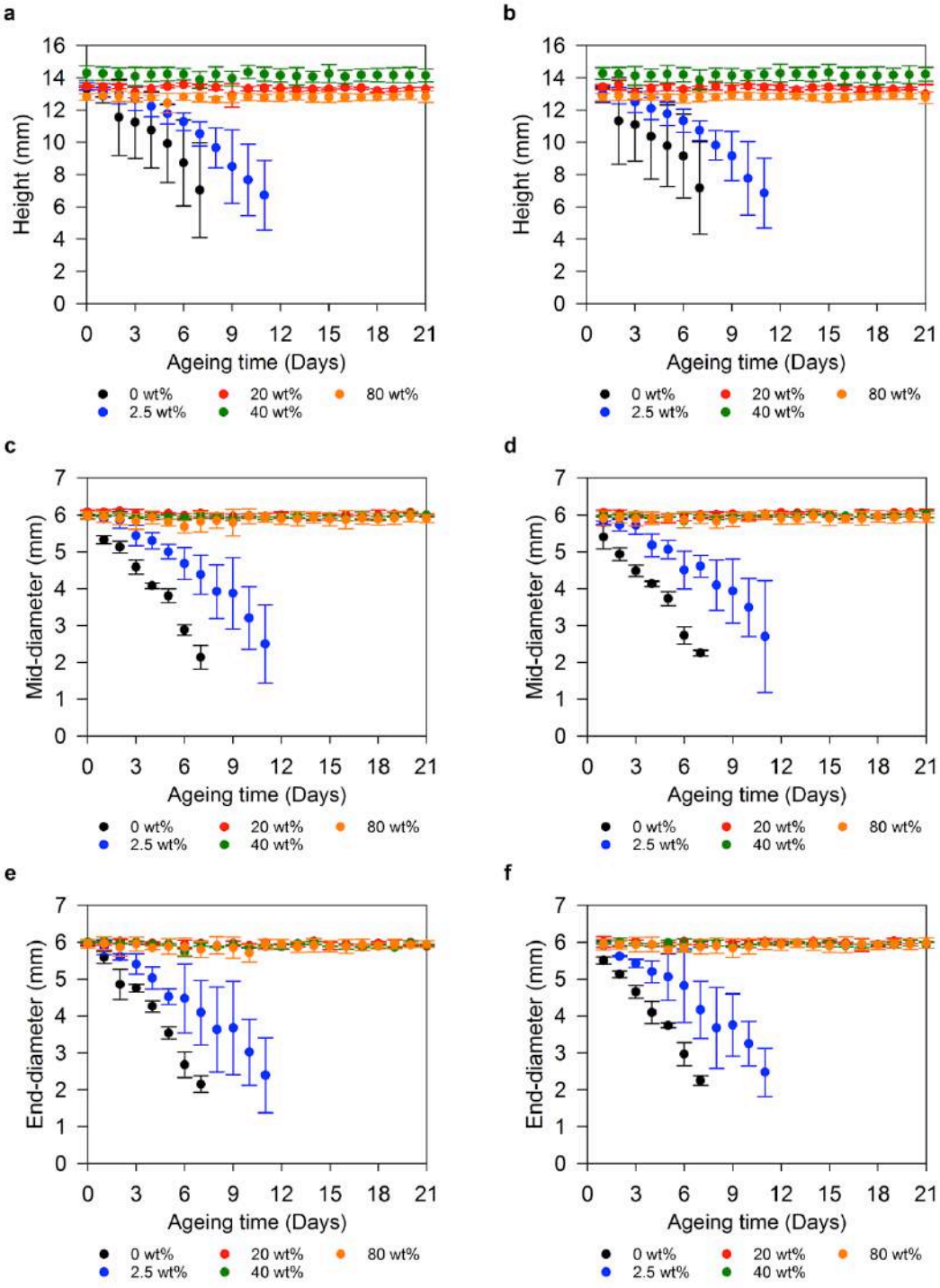

Figure 2.5 (a) Changes in PEEK/CS specimen height measured dry and **(b)** wet. **(c)** Changes in PEEK/CS specimen mid-diameter measured dry and (d) wet. **(e)** Changes in PEEK/CS specimen end-diameter measured dry and **(f)** wet. Error bars represent standard deviation (n=3).

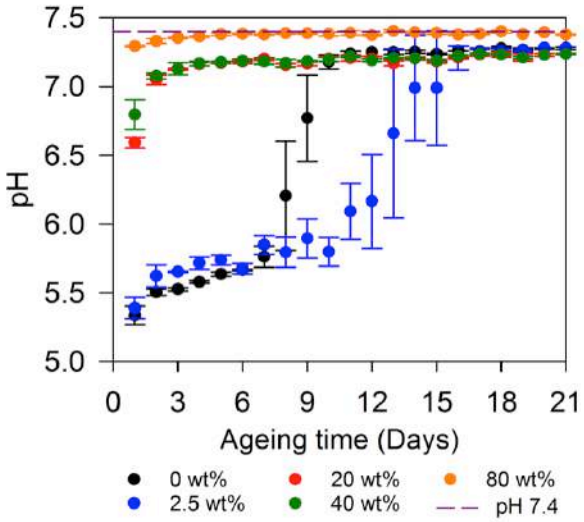

Figure 2.6 Direct pH measurements of PEEK/CS specimen PBS ageing supernatant before replenishment. PBS has a pH 7.4, and is shown in the figure by a purple dashed line as indicated by the legend. Error bars represent standard deviation (n=3).

With regards to 0%PEEK/100%CS and 2.5%PEEK/97.5%CS, the pH value of supernatant was found to decrease less extensively on a daily basis in accordance with the reducing mass of specimens due to dissolution of CS content and replenishment of PBS media (Figure 2.4a-c and 2.6)(Figure S2.2). Specimens of 20%PEEK/80%CS, 40%PEEK/60%CS and 80%PEEK/20%CS had little affect on pH of PBS ageing supernatant as values remained close to neutral throughout ageing (Figure 2.6)(Figure S2.2).

2.3.3 Mechanical properties of PEEK/CS specimens

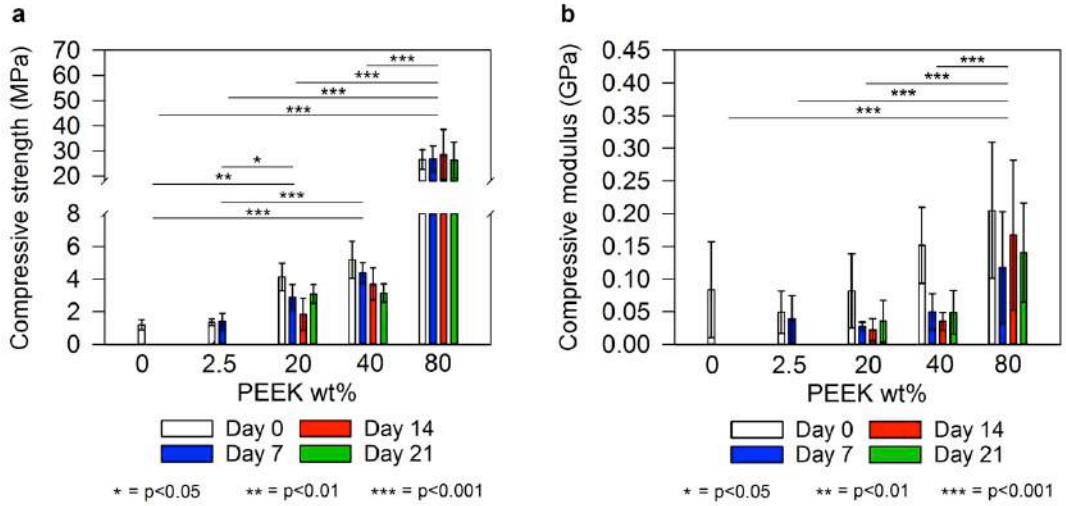

Figure 2.7 (a) Compressive strength and **(b)** Compressive modulus of PEEK/CS specimens after heat treatment and during ageing. Bar colouration is representative of ageing time as indicated by the legend. Error bars represent standard deviation (n=10) and lines above data columns represent significant differences between groups based on PEEK wt% loading as found by post-hoc Tukey HSD tests following two-way ANOVA analysis.

The compressive strength and modulus of CS (typically hydrated CSD ($CaSO_4.2H_2O$)) is typically in the range of 10 MPa to 20 MPa and between 3 GPa and 6 GPa respectively when prepared at P:L ratios between 1.5 g/mL and 2 g/mL [39, 40]. Critically, the mechanical properties of CS in this study were several orders of magnitude lower, resulting in compressive strength of 1.2±0.3 MPa and compressive modulus of 0.084±0.1 GPa. Preparation of pastes at P:L ratio of 0.85 g/mL (greater volume liquid fraction) evidently introduces porosity and areas of poor resistance to stress (Table 2.1). Further optimization of the composite may be enabled by increasing P:L ratio during

PEEK/CS fabrication [41]. Furthermore, compressing specimens prior to heat treatment, and preparing pastes under vacuum may both lower the relatively high porosity of structures prior to ageing and provide additional mechanical stability during exposure to *in vitro* physiological conditions [42, 43].

Importantly, our findings show PEEK is able to bring about significant gains in CS composite compressive strength based on PEEK wt% loading (Figure 2.7a). Specimens of 20%PEEK/80%CS and 40%PEEK/60%CS provided approximately 3-fold and 4-fold increases in compressive strength respectively prior to ageing. Interestingly, 80 wt% PEEK loading provides a further substantial rise in compressive strength of 26.6±3.9 MPa prior to ageing, equating to an approximate 22-fold gain. A significant increase was not found between groups of specimens based on ageing time ($F(3,12) = 2.1$, $p=0.16$), indicating specimens did not weaken notably due to prolonged submergence in PBS media in terms of compressive strength. Promisingly, ageing did not significantly alter compressive strength of specimens over 21 days (Figure 2.7a). Despite this, compressive modulus generally decreased with ageing time (Figure 2.7b). Evidently, a complex relationship exists between the physical and chemical interactions of PEEK with CS, such that mechanical reinforcement is provided but not necessarily maintained during facilitation of CS phase evolution and corresponding microstructural transformations.

2.3.4 Mechanism of PEEK reinforcement of CS

We propose that the strengthening and subsequent augmentation of degradation behaviour of PEEK/CS composites is due to enhanced interactions between CS crystals from the physical and chemical intercalation of PEEK following heat treatment. Without PEEK, CS is unable to retain its structure during microstructural and phase transitions initiated by PBS media. 0%PEEK/100%CS specimens likely fall apart from the infiltration of PBS solution that initiates dissolution. Heating the composites containing PEEK allows the polymer content to coat the CS crystal matrix. Even at low loadings of PEEK, such as 2.5 wt%, composites demonstrate enhanced strength and degradation response when compared to 0%PEEK/100%CS. However, the further physiochemical improvements observed at PEEK loadings of at least 20 wt% suggests that at these levels the polymer phase is able to infiltrate the entirety of structures and form a polymeric reinforcing network that binds to crystalline structures. As PEEK does not deteriorate in hydrolytic environments, the PEEK network retains structural dimensions of composites whilst protecting CS crystals from rapid deterioration in PBS media. Additionally, PEEK allows microstructural and compositional phase conversion of CS material from CSA ($CaSO_4$) to CSD ($CaSO_4.2H_2O$) (Equation 2.2), which suggests that some CS crystals remain exposed to PBS. Positively therefore, bone-forming cells may still utilise the resorbable CS content available within PEEK/CS composite materials as an osteogenic scaffold for bone deposition.

2.4 CONCLUSIONS

Physical interactions between PEEK and CS were achieved by heating of PEEK/CS specimens. Consequentially, this led to specimen discoloration regarding specimens that contained PEEK, as well as volumetric shrinkage. Excitingly however, evidence of chemical interactions between PEEK with CS through aromatic and carbonyl moieties of the polymer chain were found to exist. The nature of these interactions significantly retards *in vitro* dissolution and enhances physical attributes. As such, PEEK can be utilised to fundamentally improve CS attributes directly relevant to bone graft requirements, especially considering large defect volumes that require a protracted presence of osteogenic scaffold and mechanical stability.

2.5 ASSOCIATED CONTENT

Supporting figures and equations are included in Appendix Part 1.

2.6 REFERENCES

1. Hing HA. Bone repair in the twenty-first century: biology, chemistry or engineering? Philos Trans A Math Phys Eng Sci. 2004;362(1825):2821-50.

2. Kumar P, Vinitha B, Fathima G. Bone grafts in dentistry. Journal of Pharmacy & Bioallied Sciences. 2013;5(Suppl 1):S125-S7.

3. Shegarfi H, Reikeras O. Bone transplantation and immune response. Journal of Orthopaedic Surgery. 2009;17(2):206-11.

4. Figueiredo A, Silva O, Cabrita S. Inflammatory reaction post implantation of bone graft materials Experimental Pathology and Health Sciences. 2012;6(1):15-8.

5. Dorozhkin SV. Calcium orthophosphate bioceramics. Ceramics International. 2015;41(10):13913-66.

6. Hughes E, Yanni T, Jamshidi P, Grover LM. Inorganic cements for biomedical application: calcium phosphate, calcium sulphate and calcium silicate. Advances in Applied Ceramics. 2015;114(2):65-76.

7. Grover LM, Wright AJ, Gbureck U, Bolarinwa A, Song J, Liu Y, et al. The effect of amorphous pyrophosphate on calcium phosphate cement resorption and bone generation. Biomaterials. 2013;34(28):6631-7.

8. Lee KS, Han HS, Kim YC, Lo Han JH, Seung R H, Lee HS, et al. Evaluation of porous β-calcium pyrophosphate as bioresorbable bone graft substitute material. Materials Research Innovations. 2014;19(2):86-90.

9. Dressmann H. Ueber Knockenplombierung bei Hohlenforming Defekten des Knochens. Beitr Klin Chir. 1892;9:804-10.

10. Clayer M. Injectable Form Of Calcium Sulphate As Treatment Of Aneurysmal Bone Cysts. ANZ Journal of Surgery. 2008;78(5):366-70.

11. Liu D, Lei W, Wu Z-x, Gao M-x, Wan S-y, Fu S-c, et al. Augmentation of Pedicle Screw Stability With Calcium Sulfate Cement in Osteoporotic Sheep: Biomechanical and Screw-bone Interfacial Evaluation. Clinical Spine Surgery. 2011;24(4).

12. Orsini G, Ricci J, Scarano A, Pecora G, Petrone G, Iezzi G, et al. Bone-defect healing with calcium-sulfate particles and cement: An

experimental study in rabbit. Journal of Biomedical Materials Research Part B: Applied Biomaterials. 2004;68B(2):199-208.

13. Stubbs D, Deakin M, Chapman-Sheath P, Bruce W, Debes J, Gillies RM, et al. In vivo evaluation of resorbable bone graft substitutes in a rabbit tibial defect model. Biomaterials. 2004;25(20):5037-44.

14. Peltier LF, Jones RH. Treatment of unicameral bone cysts by curettage and packing with plaster-of-Paris pellets. The Journal of Bone & Joint Surgery. 1978;60(6):820.

15. Hing KA, Wilson LF, Buckland T. Comparative performance of three ceramic bone graft substitutes. Spine J. 2007;7(4):475-90.

16. Jamali A, Hilpert A, Debes J, Afshar P, Rahban S, Holmes R. Hydroxyapatite/calcium carbonate (HA/CC) vs. plaster of Paris: a histomorphometric and radiographic study in a rabbit tibial defect model. Calcif Tissue Int. 2002;71(2):172-8.

17. Zhou J, Yuan F, Peng S, Xie H, Wu P, Feng P, et al. Tunable Degradation Rate and Favorable Bioactivity of Porous Calcium Sulfate Scaffolds by Introducing Nano-Hydroxyapatite. Applied Sciences. 2016;6(12).

18. Liljensten E, Adolfsson E, Strid K-G, Thomsen P. Resorbable and Nonresorbable Hydroxyapatite Granules as Bone Graft Substitutes in Rabbit Cortical Defects. Clinical Implant Dentistry and Related Research. 2003;5(2):95-102.

19. Poinern GEJ, Brundavanam RK, Thi Le X, Nicholls PK, Cake MA, Fawcett D. The synthesis, characterisation and in vivo study of a bioceramic for potential tissue regeneration applications. Scientific Reports. 2014;4:6235.

20. Podaropoulos L, Veis AA, Papadimitriou S, Alexandridis C, Kalyvas D. Bone Regeneration Using B-Tricalcium Phosphate in a Calcium Sulfate Matrix. Journal of Oral Implantology. 2009;35(1):28-36.

21. Hu G, Xiao L, Fu H, Bi D, Ma H, Tong P. Study on injectable and degradable cement of calcium sulphate and calcium phosphate for bone repair. J Mater Sci: Mater Med. 2010;21(2):627-34.

22. Nilsson M, Fernández E, Sarda S, Lidgren L, Planell JA. Characterization of a novel calcium phosphate/sulphate bone cement. Journal of Biomedical Materials Research. 2002;61(4):600-7.

23. Lewis KN, Thomas MV, Puleo DA. Mechanical and degradation behavior of polymer-calcium sulfate composites. J Mater Sci: Mater Med. 2006;17(6):531-7.

24. Dandy LO, Oliveux G, Wood J, Jenkins MJ, Leeke GA. Accelerated degradation of Polyetheretherketone (PEEK) composite materials for recycling applications. Polymer Degradation and Stability. 2015;112:52-62.

25. Kurtz SM, Devine JN. PEEK Biomaterials In Trauma, Orthopedic, And Spinal Implants. Biomaterials. 2007;28(32):4845-69.

26. Kahraman S, Daneyemez M, Kayali H, Solmaz I, Bedük A, Akay M. Polyetheretherketone (Peek) Cages For Cervical Interbody Replacement: Clinical Experience. Turkish Neurosurgury. 2006;16(3):120-3.

27. Ellis G, Naffakh M, Marco C, Hendra PJ. Fourier transform Raman spectroscopy in the study of technological polymers Part 1: poly(aryl ether ketones), their composites and blends. Spectrochima Acta Part A. 1997;53:2279-94.

28. Henneuse C, Goret B, Marchand-Brynaert J. Surface carboxylation of PEEK film by selective wet-chemistry. Polymer. 1998;39(4):835-44.

29. Henneuse C, Boxus T, Duliere E, Pringalle C, Tesolin L, Adriaensen Y, et al. Surface amination of PEEK film by selective wet-chemistry. Polymer 1998;39(22):5359-69.

30. Díez-Pascual AM, Martinez G, Gómez, MA. Synthesis and Characterization of Poly(ether ether ketone) Derivatives Obtained by Carbonyl Reduction. Macromolecules. 2009;42(18):6885-92.

31. Bensted J, Varma SP. Infrared Spectroscopic Studies of Calcium Sulphate heated to High Temperatures. Z Naturforsch. 1971;26:690-3.

32. Putnis A, Winkler B, Fernandez-Diaz L. In situ IR spectroscopic and thermogravimetric study of the dehydration of gypsum. Mineralogical Magazine. 1990;54:123-8.

33. Fernandez-Carrasco L, Torrens-Martín D, Morales LM, Martínez-Ramírez S. Infrared Spectroscopy in the Analysis of Building and Construction Materials. Infrared Spectroscopy - Materials Science, Engineering and Technology: InTech; 2012.

34. Balaji SM. Recent Advances in Oral Surgery. Textbook of Oral & Maxillofacial Surgery: Elsevier; 2007.

35. Baradari H, Damia C, Dutreih-Colas M, Laborde E, Pécout N, Champion E, et al. Calcium phosphate porous pellets as drug delivery systems: Effect of drug carrier composition on drug loading and in vitro release. Journal of the European Ceramic Society. 2012;32(11):2679-90.

36. Shah MR, Patel RR, Solanki RV, Gupta SH. Estimation of drug absorption in antibiotic soaked bone grafts. Indian Journal of Orthopaedics. 2016;50(6):669-76.

37. Kameda T, Mano H, Yamada Y, Takai H, Amizuka N, Kobori M, et al. Calcium-Sensing Receptor in Mature Osteoclasts, Which Are Bone Resorbing Cells. Biochemical and Biophysical Research Communications. 1998;245:419-22.

38. Walsh WR, Morberg P, Yu Y, Yang JL, Haggard W, Sheath PC, et al. Response of a calcium sulfate bone graft substitute in a confined cancellous defect. Clin Orthop Relat Res. 2003(406):228-36.

39. Liu W, Wu C, Liu W, Zhai W, Chang J. The effect of plaster (CaSO4 .1/2H2O) on the compressive strength, self-setting property, and in vitro bioactivity of silicate-based bone cement. J Biomed Mater Res B Appl Biomater. 2013;101(2):279-86.

40. Koh I, Lopez A, Helgason B, Ferguson SJ. The compressive modulus and strength of saturated calcium sulphate dihydrate cements: implications for testing standards. Journal of the mechanical behavior of biomedical materials. 2014;34:187-98.

41. Fleming G. Influence of powder/liquid mixing ratio on the performance of a restorative glass-ionomer dental cement. Biomaterials. 2003;24(23):4173-9.

42. Barralet JE, Grover LM, Gbureck U. Ionic modification of calcium phosphate cement viscosity. Part II: hypodermic injection and strength improvement of brushite cement. Biomaterials. 2004;25(11):2197-203.

43. Macaulay W, DiGiovanni CW, Restrepo A, Saleh KJ, Walsh H, Crossett LS, et al. Differences in bone–cement porosity by vacuum mixing, centrifugation, and hand mixing. The Journal of Arthroplasty. 2002;17(5):569-75.

Chapter 3. Biologically analogous calcium phosphate tubes from a chemical garden

Adapted from:

Hughes EAB, Williams RL, Cox SC, Grover LM. Biologically Analogous Calcium Phosphate Tubes from a Chemical Garden. Langmuir. 2017;33(8):2059-67.

Authors: Erik A. B. Hughes[1], Dr. Richard L. Williams[1], Dr. Sophie C. Cox[1], and Prof. Liam M. Grover[1]

Affiliations: [1]School of Chemical Engineering, University of Birmingham, Edgbaston, B15 2TT, UK

Corresponding author: Prof. Liam Grover (l.m.grover@bham.ac.uk)

Table of contents (TOC) image

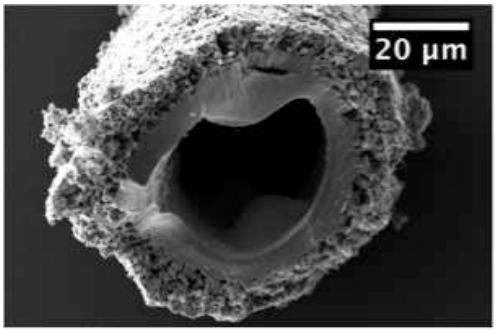

3.0 ABSTRACT

Calcium phosphate ($CaPO_4$) tubes with features comparable to mineralised biological microstructures, such as Haversian canals, were grown from a calcium gel/phosphate solution chemical garden system. A significant difference in gel mass in response to high and low solute phosphate equivalent environments existed within 30 minutes of solution layering upon gel (p = 0.0067), suggesting the nature of advective movement between gel and solution is dependent on solution concentration. Transport of Ca^{2+} and PO_4^{3-} was quantified and changes in pH were monitored to explain preferential formation of tubes within a PO_4^{3-} concentration range of 0.75-1.25 M. Ingress from the anionic solution phase into the gel followed by liberation of Ca^{2+} ions from the gel was found to be essential for acquiring self-assembled tubular $CaPO_4$ structures. Tube analysis by scanning electron microscopy (SEM), X-ray diffraction (XRD), and micro X-ray florescence (μ-XRF) revealed hydroxyapatite (HA, $Ca_{10}(PO_4)_6(OH)_2$) and dicalcium phosphate dihydrate (DCPD, $CaHPO_4.2H_2O$) phases organised in a hierarchical manner. Notably the tubule diameters ranged from 100 to 150 μm, an ideal size for permeation of vasculature in biological hard tissue.

3.1 INTRODUCTION

Tubular mineralised structures that contribute to intricate arrangements and networks are found throughout nature, forming in bamboo, coccolithophores, corals, and exotic architectures such as the central rose of water-pot shell [1-7]. Tube-like motifs are also found in the hard tissues of

mammals, including dentinal tubules in teeth and Haversian canals in bone [1-4]. These features are not random, functioning to enable gases and nutrients to pass through tissues of relatively low pore volume and maintain the viability of embedded cell populations. Many presume that the formation of these tubes is entirely biologically driven by cellular processes [8, 9]. Odontoblasts for instance are thought to play a significant role in guiding the formation of dentinal tubules [10]. Although often over looked, physical processes, such as the fluid flow, play a crucial role in the development of ear, kidney and brain tissue [11]. A better understanding of these processes in terms of guiding mineral formations is desirable and may even assist in attempts to replicate hard tissue structure more closely for the purpose of advanced regenerative biomaterials. Disease processes may also be better understood. Osteophytes for instance are organised extrusions of mineral that extend from subchondral bone into the joint space and are pathological in osteoarthritis [12].

A chemical garden commonly refers to solid elongated structures that form from the surface of a metal ion monolith when added to silicate solution [13]. Such systems remain of great interest to scientists since their conception in the early 17th century, having first been observed by German-Dutch alchemist Johann Glauber in 1646 [14]. Fascination stems from their likeness to aforementioned mineralised structures that originate from both biotic and abiotic systems. Many combinations of reactive species can be combined in these systems, including but not limited to metallic cations of calcium, strontium, copper, iron and cobalt with anionic species of silicate, carbonate, borate and phosphate [13-18]. Complex osmotic processes drive the

formation of these life-like tubular precipitates, as understood through research predominantly undertaken in the 19th and 20th centuries [14, 19]. Work by Kamiya *et al.,* and more recently Steenbjerg Ibsen *et al.,* disseminated important mechanistic understanding of tubular architectures grown from at a gel/solution interface, which form similarly to that of a chemical garden [20, 21]. Formation begins when a semi-permeable membrane is formed over the gel phase due to the initial reaction between cationic species in the gel and anions in the solution phase resulting in an insoluble reaction product. When osmotic forces allow, fluid rich in metal ions is liberated from the gel into the ionic solution phase, which self assembles into hollow tubes whereby the gel pores serve as an initial template [20, 22]. Continuous growth is confirmed to occur at the tips of already established tubes, maintained through repeating cyclic build-ups of osmotic pressure and release of cation rich solution through a point of rupture. The necessary mass transport is facilitated by dis-equilibrium between species present on either side of the established semi-permeable membrane [18].

Despite this understanding, quantitative analysis surrounding chemical gardens remains unfortunately sparse [23-25]. Factors that determine tube growth rate are poorly understood, but may be better explained through studying the rates of precipitation and advective transport, providing complementary data to previous work on how precipitates form at gel/solution interfaces [20, 21, 26]. The gel/solution set-up offers the opportunity for quantitative parameters to be measured that can be linked back to theoretical expectations of tube formation. In this paper, the formation of tubules of

calcium phosphate ($CaPO_4$) at the gel/solution interface was investigated. Solution movement in and out of a 1 M calcium (Ca^{2+}) loaded agar gel was monitored in a phosphate (PO_4^{3-}) rich environment, and the dependence of this exchange on tubule development by differing solute potential environments was investigated.

Whilst osseous tissue scaffolds that are able to support the production of bone extra cellular matrix (ECM) have been developed, they suffer from poor vascularisation [27-29]. $CaPO_4$ tubes however may possess high surface area, narrow pore distribution, and mass transport viability, offering enhanced cellular ingress and facilitation of directed angiogenesis and tubulogenesis for generation of bony tissue in comparison to the current cohort of scaffold and unstructured calcium based augmentation minerals [29-32]. Recent work regarding calcium silicate-phosphate tubes demonstrates the high potential of chemical garden structures to support the attachment and viability of mammalian cell cultures [33]. Microstructural and compositional characterisation of $CaPO_4$ tubes was undertaken to assess their similarity to chemical garden structures, understand how they develop during formation and assess their potential suitability to be explored further as an osteogenic self-assembling biomaterial.

3.2 EXPERIMENTAL METHODS

3.2.1 Materials

Calcium nitrate tetrahydrate ($Ca(NO_3)_2.4H_2O$, 99 %, ACS reagent), agar ($(C_{12}H_{18}O_9)_n$, for microbiology), ammonium phosphate dibasic

($(NH_4)_2HPO_4$, ≥98.0 %, reagent grade), and sodium chloride (NaCl, ≥99 %, ReagentPlus®) were acquired from Sigma-Aldrich (UK). Distilled water was acquired from an Arium® advance EDI system.

3.2.2 Preparation of $CaPO_4$ tubes

$Ca(NO_3)_2.4H_2O$ was dissolved in 0.1 L distilled water to the concentration of 1 M (or NaCl in the case of PO_4^{3-} in gel measurements to the concentration of 2 M) and 5 g of agar added (with 250 μL of universal pH indicator (British Drug Houses Ltd, UK) for a selection of studies). The mixture was stirred at 250 rpm and heated to 80-90 ^oC on a MR Hei-Standard magnetic stirrer hotplate (Heidolph, Germany). After sufficient time to allow for the dissolution of the gel precursor, 2.5 mL of the gel mixture was syphoned into clear cylindrical tubes. The mixture was given 24 hours to complete gelation. $(NH_4)_2HPO_4$ (or NaCl for Ca^{2+} elution measurements) solutions were prepared as required and 3 mL was layered over the set Ca^{2+} containing gel. pH was monitored using a calibrated S220 Seven Compact™ pH/ion meter equipped with an InLab Expert Pro pH probe (Mettler Toledo, USA).

3.2.3 Measuring the gel mass gain/loss

Ca^{2+} gel mixture was syphoned into an in house mold to produce 6 mm x12 mm cylindrical specimens that were easy to handle (Figure S3.1a). Specimens were first individually weighed before submerging in 7.5 mL of either 0.5 M or 5 M NaCl solutions (Figure S3.1b). After desired times of submersion, specimens were dabbed dry and re-weighed.

3.2.4 Measuring elution of Ca^{2+}

Ca^{2+} gels prepared as standard were layered with 20 mL NaCl solutions of 0.5 M, 1 M, 2 M, 3 M, 4 M and 5 M (n=3 per NaCl solution employed). In each system, the elution of Ca^{2+} into solution phase was tracked by collecting a 2 mL solution sample at a desired time point and directly measuring the Ca^{2+} concentration using a S220 Seven Compact™ pH/ion meter equipped with a perfectION™ comb Ca Combination Electrode (Mettler Toledo, USA). The electrode reference electrolyte (Ion Electrolyte A) was refreshed and a calibration curve for Ca^{2+} at 1000 mg/L, 100 mg/L and 10 mg/L following the probe manufacturers guidelines was collected for conversion of mV reading to mg/L (Figure S3.2). Replenishment of the solution phase was undertaken appropriately after collection of each sample aliquot. This was considered a dilution factor and was accounted for in the final Ca^{2+} concentration calculation (Equation S3.1). Finally, concentration units were converted to mM.

3.2.5 Measuring PO_4^{3-} in gel phase

NaCl 2 M gels of the standard system were investigated layered with 20 mL PO_4^{3-} solutions of 0 M, 0.25 M, 0.5 M, 1 M, 1.5 M, 2 M and 2.5 M (n=2 per PO_4^{3-} solution employed). After 15 minutes, the solution phase was tipped away and the gel surface rinsed briefly with distilled water. A corer (2 cm diameter) was used to retrieve a sample of gel that was cut to produce a cylindrical gel specimen of 65 mm length including gel surface. The gels were then submerged in 35 mL of distilled water, broken down and left overnight to

soak. It was assumed that any PO_4^{3-} in the gel phase would leach out of the gel network and be diluted from the soaking solution. The dilution factor of the leaching volume of water was accounted for to give the measured PO_4^{3-} in gel phase (Equation S3.2). A Phosphate assay (Sigma-Aldrich Phosphate Colourmetric kit, MAK030) was then used to find the concentration of PO_4^{3-}. The calibration curve is provided (Figure S3.3), and was used to directly measure PO_4^{3-} concentration.

3.2.6 Scanning electron microscopy (SEM)

SEM micrographs were collected for intact tube structures placed on double adhesive carbon tapes attached to aluminium stubs. All sample were gold sputter coated. Secondary electron images of the tubes were obtained using a Sigma SEM (Carl Zeiss AG, Germany) operating at 10 kV.

3.2.7 X-ray diffraction (XRD)

Powder XRD patterns were acquired using a Powder Diffractometer D8 Autosampler (Bruker, USA) using the Cu Kα line. Pattern data was collected from between $2\theta = 5^{o}$ to 60^{o} with a 0.02^{o} step-size and a step time of 0.5 $s/^{o}$. The background signal was removed and intensity normalised. Patterns were matched to those in the International Centre for Diffraction Data (ICDD) database.

3.2.8 Micro- X-ray fluorescence (μ-XRF)

μ-XRF was performed using a M4 Tornado instrument (Bruker, USA) in mapping mode. The scan area measured 900 μm x 645 μm. The X-ray tube was operated at 50 kV voltage with anode current of 300 mA. The mapping scan was acquired over 20 frames with a time of 5 ms/pixel. The chamber was kept under a vacuum of 30 mbar.

3.3 RESULTS AND DISCUSSION

3.3.1 Initial observations and understanding $CaPO_4$ chemical garden growth regimes

Nodular and unstructured $CaPO_4$ precipitate was observed at the gel/solution interface at PO_4^{3-} solution concentrations between 0.25 and 0.5 M (Figure 3.1a,b). Generally, solutions between 0.5 and 1.5 M PO_4^{3-} resulted in substantially faster rates of tube formation and in larger number (75-125 tubules per 236 mm^2) (Figure 3.1a). The macromorphology of these tubes is typically straight with kinks, suggesting a jetting and popping regime of growth. Different growth regimes occur as a consequence of variations in anionic solution density. Low density Ca^{2+} solution entering the PO_4^{3-} solution phase can either rise quickly producing a jet that catches to form a straight tube section or lead to oscillatory tube growth characterised by budding architectures and alterations in tube growth direction [15]. Tube length was observed to reach several centimeters within 15 minutes and within 2 hours it appeared some tubes had begun to agglomerate due to a lack of free growth space that resulted in wall bound features after several days (Figure 3.1c).

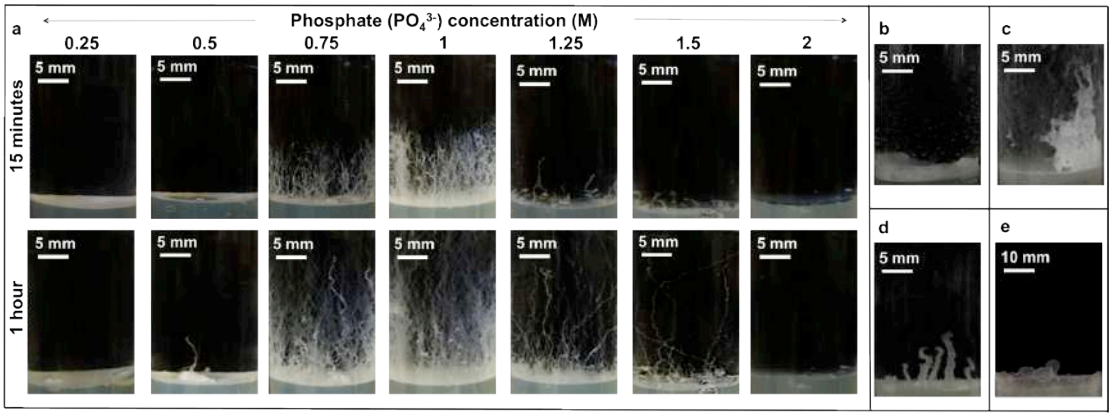

Figure 3.1 Influence of PO_4^{3-} concentration on $CaPO_4$ tube formation. Visualisation of tube growth after 15 minutes, and 1 hour in 0.25-2 M PO_4^{3-} solutions **(a)**, unstructured precipitate in 0.25 M PO_4^{3-} solution after 4 days **(b)**, tube agglomeration and wall bound growth in 1 M PO_4^{3-} solution after 4 days **(c)**, thick budding tubes grown in 2 M PO_4^{3-} solution after 4 days **(d)**, sack-like morphologies grown in 2 M PO_4^{3-} solution after 4 days **(e)**.

Initially, layering of 2 M PO_4^{3-} solutions upon the gel phase produces no $CaPO_4$ precipitate. On occasion, relatively thick tubes were observed in 2 M PO_4^{3-} solutions after a few days (Figure 3.1d). These tubes were evidently wider than those grown in 0.5-1.5 M PO_4^{3-} solutions and synonymous with a budding regime of tube growth, forming from the release of less buoyant cationic solution providing a wider tube girth at the origin of growth [13-16]. Similarly thick tubes that formed in a chemical garden consisting of a calcium chloride ($CaCl_2$) seed in 6 M silicate solution have been reported [15]. It is suggested that air bubbles developed in the concentrated (6 M) and viscous silicate solutions used, acting as templates for wide tubes at the origin of growth [15]. Although air bubbles were not observed to aid the formation of

$CaPO_4$ structures, they provide an interesting means for controlling tube growth parameters that has been explored elsewhere [34, 35]. As well as thick tubes, $CaPO_4$ sack-like morphologies arose in some 2 M PO_4^{3-} solutions, which likely formed through inflation of the precipitate membrane with Ca^{2+} rich liquid without sufficient osmotic force to cause rupture (Figure 3.1e).

The growth behaviour and resulting morphology of tubules between thin shoots of material, thicker tubules and inflated sacks is partially linked to the development of a semi-permeable precipitate membrane upon the gel/solution interface due to the reaction between metal ions and reactive anions in solution. For the analogous classical set-up, it is believed that concentrated anionic solutions produce a firmer colloidal membrane that is more difficult to rupture promoting membrane inflation, whilst relatively lower concentrations produce a comparably thinner membrane that can be more easily penetrated by metal-ion streams to go to form tubes [13-16]. Similar tube morphology and growth characteristics are observed for $CaPO_4$ tubes grown in low (0.25 M) and high (2 M) PO_4^{3-} solution concentrations (Figure 3.1a). The growth mechanism that results in $CaPO_4$ morphologies is further discussed in this work alongside the fundamental experimental data.

When PO_4^{3-} solutions were layered upon the Ca^{2+} gel phase, a concentration dependent coverage of precipitation was observed. Between 0.25 and 0.5 M PO_4^{3-}, a membrane of precipitate formed that occupied 99.6 % and 63 % of the gel/solution interface respectively (Figure 3.2). At 0.25 M PO_4^{3-}, membrane rupture results in jetting streams of $CaPO_4$ material that fail to form tubes, consistent with the proposition of a weak rupture membrane

[13-16]. In relatively low concentrations of PO_4^{3-} solutions (0.25-0.5 M), the $CaPO_4$ membrane may take longer to form, as the initial precipitate membrane disappears within 2 hours and tubes are only visible after this time. For PO_4^{3-} solutions in the concentration range between 0.75 and 1.25 M, localised spots of precipitate were visible upon the gel solution interface, which provided the origin of tubes that formed immediately. Despite the expectation of a precipitate membrane when solutions of 2 M PO_4^{3-} were employed, no precipitate coverage was observed upon the gel/solution surface. It is possible that the required levels of Ca^{2+} and PO_4^{3-} ions are insufficient to induce precipitation when 2 M PO_4^{3-} is immediately layered upon gel. Alternatively, the ionic concentration of both species may well be sufficient for precipitation, however the increased concentration of non-precipitate counter ions may decrease the effective concentration of Ca^{2+} and PO_4^{3-} in solution through ionic shielding phenomena [36]. Ionic shielding involves counter ions surrounding reactant ions of opposite change in solution, preventing them from reacting even in concentrated solutions where products would be expected to form [36]. An extended induction time is evidently required for the precipitate reaction of Ca^{2+} and PO_4^{3-} ions in these systems, eventually resulting in structures (Figure 3.1d,e). The inflated nature of constructs that are produced suggests that despite taking longer to develop, the resulting precipitate membrane can resist rupture to an extent beyond that formed in solutions >2 M. However, whilst optimum solution concentration ranges for inducing tubules have been explored in different chemical garden systems, the observation and quantification of a

concentration dependent precipitate coverage upon the cationic source, in this case the Ca^{2+} loaded gel, has not previously been reported for chemical garden systems. The colour similarity between the newly forming precipitate and that of the crystal seed make this differentiation difficult in the classical set-up. Hence the use of a gel/solution system may enable us to gather further mechanistic insights into spontaneous tube formation gardens.

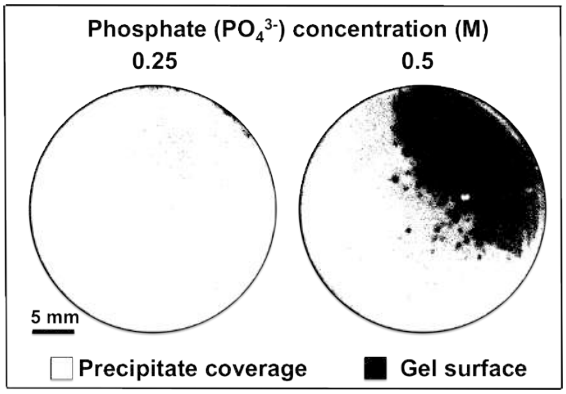

Figure 3.2 Top down view binary image of the typical $CaPO_4$ precipitation coverage formed upon the gel/solution interface for PO_4^{3-} solutions of 0.25 and 0.5 M 1 minute after layering upon the gel surface.

3.3.2 Response of the gel phase to varying solute potential

Gel mass change experiments were conducted in solutions of 1 and 5 M NaCl as opposed to PO_4^{3-} in order to avoid initiating precipitation; selected solutions exhibit an equivalent solute potential to PO_4^{3-} solutions of 0.5 and 2.5 M respectively, calculated using the van't Hoff equation (Equation S3.3 and Table S3.1). Gel mass gain/loss profiles were dynamic in both 1 and 5 M NaCl solutions (Figure 3.3). As expected, a 1 M NaCl solution brought about an initial gradual gel mass increase in the first 3 minutes (+2.7±0.2 %), measured at its most substantial after 10 minutes (+3.2±1.6 %), due to the

potential gradient favouring the net movement of solution into the gel from solution phase. Gels in 5 M NaCl solutions decreased in mass by 0.7±0.3 % after 10 minutes due to the potential gradient favouring the net movement of Ca^{2+} rich solution out of the gel into the solution phase (Figure 3.3). At 30 minutes, despite gaining some mass, the gels in 5 M PO_4^{3-} solution remained in a net mass loss regime (-0.1±0.5 %) before further mass decrease at 2 hours (-1.4±1.7 %). Statistical analysis performed using a two-way ANOVA revealed a significant difference in the gel mass gain/loss response from employment of low concentration (1 M NaCl) and high concentration (5 M NaCl) solution environments (F (1, 4) = 26.57, p = 0.0067) within the first 30 minutes of gel exposure to solution. Post hoc t-tests revealed significance between the mass gain/loss gel response at 1 minute (p = 0.0067), 3 minutes (p = 0.037) and 10 minutes (p = 0.012).

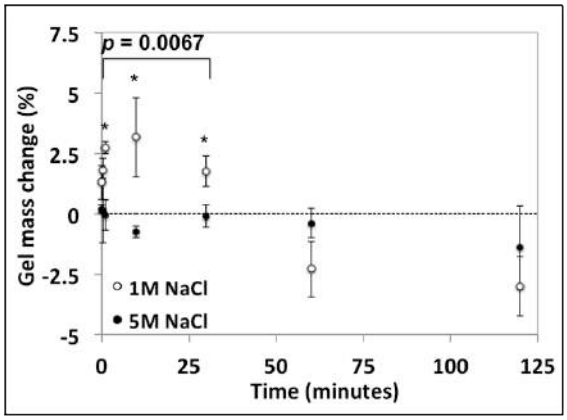

Figure 3.3 Mass gain/loss profile of gels exposed to 1 and 5 M NaCl solutions between 0-120 minutes (error bars represent standard deviation for n = 3 measurements of individual samples, * = significance as determined by post hoc t-test analysis, where $p = < 0.05$).

These results go some way to understanding the preferential formation of $CaPO_4$ tubes in PO_4^{3-} solutions between 0.5-2.5 M. Between these concentrations, osmotic driving forces appear to drive movement of solution across the semi-permeable precipitate barrier, the coverage taking the form of a sheet or localised spots upon the gel/solution interface, towards the gel. Consequently, the gel mass increase leads to a build-up in osmotic pressure. In order to counteract this, the pressure is relieved through rupturing the precipitate membrane, which releases streams of Ca^{2+} rich solution into the corresponding solution of PO_4^{3-}. The jetting and occasional oscillatory nature of these Ca^{2+} streams provides a template for the growth of tubular constructs with straight and kinked macromorphology (Figure 3.1a). Solutions of PO_4^{3-} either side of the 0.5-1.5 M concentration range as investigated through NaCl solutions with matching solute potentials, appear not to elicit a gel mass increase, but rather a decrease, indicating that solution is expelled. As such, the build up of osmotic pressure within the gel does not take place and tubes are not immediately formed from the employment of 0.25 and 2 M PO_4^{3-} solutions.

3.3.3 Ca^{2+} and PO_4^{3-} ion transport

Release of Ca^{2+} ions occurred in all NaCl solutions in the range 0.5-5 M and progressed steadily with time (Figure 3.4a). Expectedly, elution rate increased gradually with increasing NaCl solution concentration as the potential for ionic Ca^{2+} movement from gel into solution phase proportionally intensifies in more concentrated solution environments.

Before layering with PO_4^{3-}solutions, the PO_4^{3-} concentration found in the gel existed at a comparatively low concentration of 0.11±0.00 mM (Figure 3.4b). After 30 minutes, concentration of PO_4^{3-} in the gel peaked at 34.30±5.87 mM when PO_4^{3-} concentration of the solution was 1 M, and decreased at higher PO_4^{3-} concentrations of solution phase; ingression of PO_4^{3-} into the gel as a function of initial PO_4^{3-}concentration in solution was therefore not monotonic and did not follow the same trend as Ca^{2+} release into the anionic solution phase (Figure 3.4b).

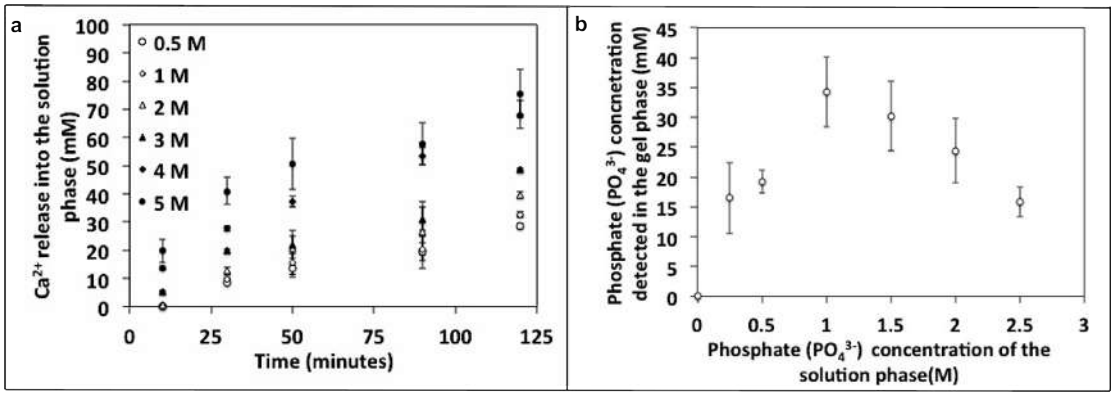

Figure 3.4 Ca^{2+} release into bulk solution dependent on NaCl solution concentration (error bars represent standard deviation for n = 3 measurements of individual samples) **(a)** and PO_4^{3-} ingress into the gel dependent on PO_4^{3-} solution concentration (error bars represent standard deviation for n = 2 measurements of individual samples) **(b)**.

3.3.4 Observing pH change as an indicator of ionic movement

A capillary tube was inserted just below the gel/solution interface allowing the collection of ejected calcium rich solution from the gel (Figure 3.5a). Universal pH indicator revealed the acidic nature of the Ca^{2+} rich fluid in

contrast to the neutral-alkali nature of the PO_4^{3-} solution that had also been collected on pull out (Figure 3.5b). The pH of the gel mixture before heating and setting was determined to be 4.5-5.5 and gels stained with universal pH indicator became orange due to the acidic cationic environment. PO_4^{3-} solution pH was between 8 and 9.

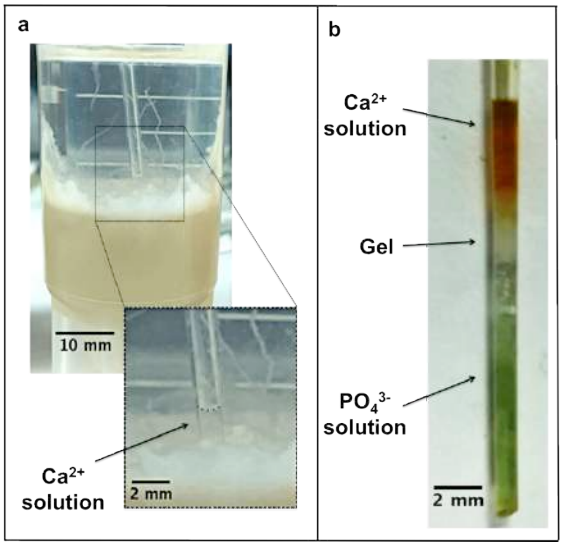

Figure 3.5 Ca^{2+} rich solution as collected in a capillary tube placed at the gel/solution interface **(a)**, followed by removal of the capillary tube and staining of the collected contents with universal pH indicator **(b)** (PO_4^{3-} solution was drawn up the capillary tube on pull out).

$CaPO_4$ tubes form preferentially in regions where the pH at the gel/solution interface experiences a substantial shift to alkalinity by turning blue or purple in the gel phase, suggestive of an environment at pH 8 to 10 (Figure 3.6a and S3.4)(Movie S3.1). Regions that did not experience this shift resulted in little or poor $CaPO_4$ tubular growth, but sometimes developed a red colouration band at the gel/solution interface (Figure 3.6a)(Movie S3.1). Similar experiments have shown that although shifts in pH are not a trigger for

tubule formation, but rather a by-product of precipitate development, measurements of pH can be utilised as an indicator of solution exchange and tubule formation [21].

Layering of 0.25 and 0.5 M PO_4^{3-} solutions facilitated a red (acidic) band at the gel/solution interface (Figure 3.6b) that was more prominent in gels layered with 0.25 M solutions (Figure 3.6c). From Ca^{2+} release measurements (Figure 3.3a), release of Ca^{2+} ions was less extensive in equivalent 0.25 M PO_4^{3-} solutions compared to 0.5 M PO_4^{3-} solutions. Therefore, red colouration represents a build-up of unreleased acidic Ca^{2+} ions just below the gel/solution interface, which ultimately delays the onset of tubules (Figure 3.1a). Red (acidic) banding eventually turned blue in colour (increasingly alkaline) when both 0.25 and 0.5 M PO_4^{3-} solutions were used, and coincided with the onset of $CaPO_4$ nodular precipitate and tubular structure formation, respectively (Figure 3.1a and 3.6a). Colouration at the gel/solution interface for gels layered with 0.75 and 1 M PO_4^{3-} solutions was blue (alkali) initially before appearing purple (stronger alkali). Gels layered with solutions between 1.25 and 2.5 M PO_4^{3-} developed a purple band immediately.

Depth of the alkaline colouration bands increased with increasing PO_4^{3-} solution concentration in the range 0.75-2 M (Figure 3.6b,c), which correlates to the exodus of Ca^{2+} ions and ingress of PO_4^{3-} anions into the gel by solution movement (Figure 3.3 and 3.4a,b). The resulting exchange of ions promotes the induction of tubule formation above the gel/solution interface in 0.75-1.5 M PO_4^{3-} solutions (Figure 3.1a). This doesn't necessarily correlate with the

formation of precipitate in 2 M PO_4^{3-} solutions. Although a relatively high concentration of Ca^{2+} ions are released into a 4 M NaCl solution with a comparable osmotic potential to 2 M PO_4^{3-} solution suggests that super saturation criteria for $CaPO_4$ precipitation are met (Figure 3.4a), previously alluded to ionic shielding effects ultimately diminish the effective concentration of ions available to react [36].

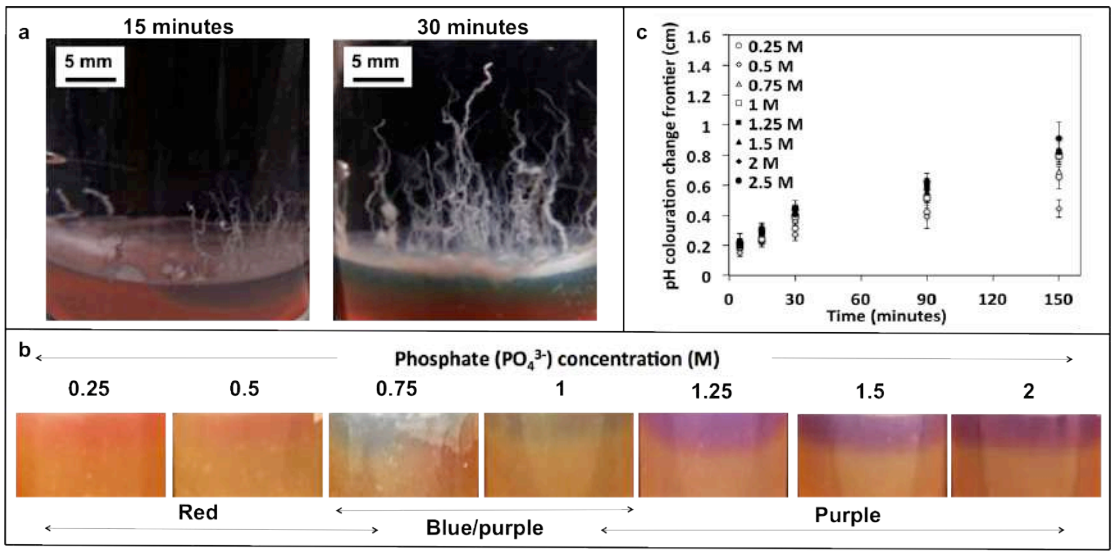

Figure 3.6 Universal pH indicator stained gel layered with 0.5 M PO_4^{3-} solution changing colouration in response to $CaPO_4$ tubular formation **(a)**. Gels stained with universal pH indicator and layered with 0.25-5 M PO_4^{3-} solutions at 30 mins (Field of view ~30 mm) **(b)** and quantification of the colouration band depth (error bars represent standard deviation for n = 3 measurements of individual samples) **(c)**.

3.3.5 Microstructural and compositional evolution of $CaPO_4$ tubes

A tube widening phenomena was observed from micrographs of $CaPO_4$ tubes grown in 0.5 M PO_4^{3-} solutions over 24 hours. Tubes typically matured to a final diameter of 100-150 μm, and possessed a bilayer wall

consisting of a porous outer layer (~10 μm) and continuous inner layer (~10 μm) that is consistent with the microstructure of chemical gardens [18] (Figure 3.7a). This arrangement is comparable to the structuring of micron width dentinal tubules, although existing at length scales typical of Haversian canals which at maturity exhibit an average diameter between 50 and 200 μm in human bone [1, 4, 9, 37, 38].

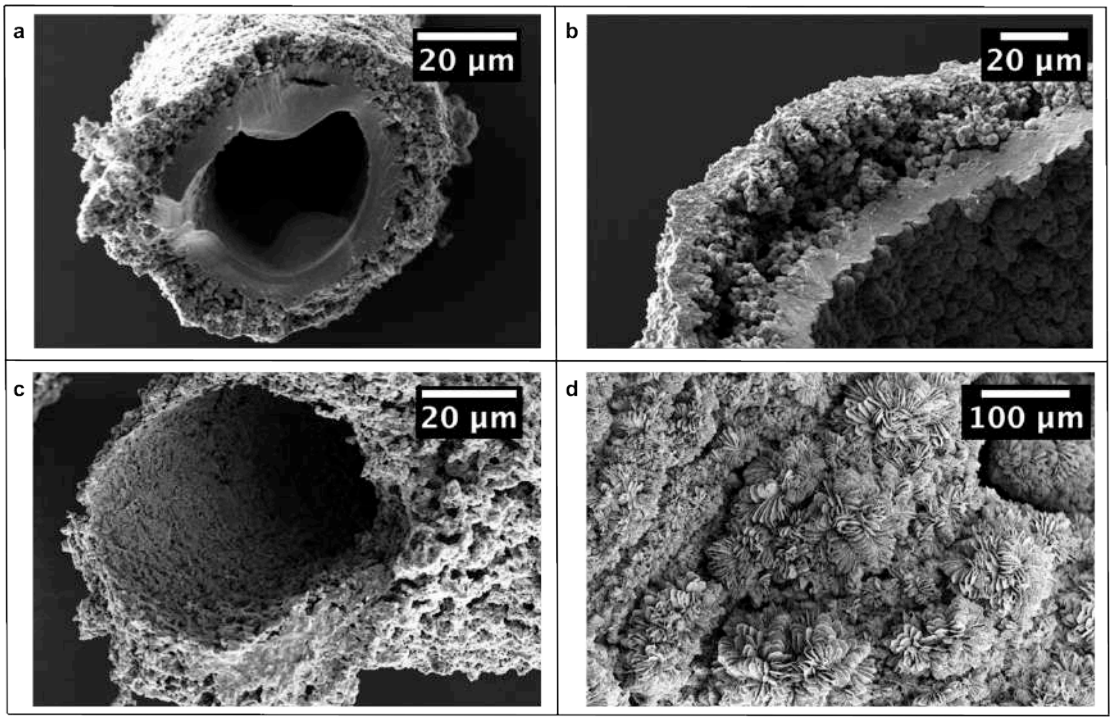

Figure 3.7 Micrographs of $CaPO_4$ tubes grown in 0.5 M PO_4^{3-} solutions extracted at 5 hours **(a)** and 24 hours **(b)**, $CaPO_4$ tubes grown in 1.25 M PO_4^{3-} solutions **(c)**, and $CaPO_4$ tubes grown in 2 M PO_4^{3-} solutions **(d)** extracted at 10 days.

At 24 hours, widened tubes possessed a diameter >300 μm and a gap space developed between the outer and inner tube layers suggesting

immiscible material phase separation (Figure 3.7b). Close inspection of the walls of typical and widened tubes revealed that both the inner and outer thickness remained ~10 μm per layer. Wall thickness may be maintained through a spontaneous self-healing mechanism that allows for total tube widening whilst maintaining the thickness of the tube walls in order to support structural integrity and microstructural evolution [14]. In response to increased periods of cationic fluid flow, that are dependent on solution potential differences between cationic and anionic phases, tubes may expand.

The diameter of $CaPO_4$ tubes from PO_4^{3-} solutions between 0.75 - 1.5 M ranged from 100 - 150 μm (Figure 3.7c). Tubes grown in 0.75 and 1 M PO_4^{3-} solutions shared similar microstructure to those grown in 0.5 M PO_4^{3-}, possessing a porous outer layer and continuous inner layer. In contrast, tubes grown in 1.25 and 1.5 M PO_4^{3-} solutions possessed a single porous wall that was microstructurally similar to the outer wall of tubes that exhibited a bilayer structure (Figure 3.7c). Tubes grown in 2 M PO_4^{3-} had a strikingly different microstructure that consisted of organized flowering flake clusters (Figure 3.7d). The diameter of these tubes was also considerably wider (500-600 μm).

It is evident that the scale and microstructure of these tubes mimics intrinsic features of natural bone tissue at the length scale of Haversian canals that house vascular networks. As such, the fabrication of $CaPO_4$ tubules may be of interest for replicating these structures through physical phenomena at gel/solution interfaces.

X-ray diffraction patterns were collected to study the evolution of crystallinity and crystalline phase during initial precipitate formation in 0.5 M PO_4^{3-} solutions (Figure 3.8a). After 3 and 5 hours, the precipitate consisted of poorly crystalline apatite, as suggested by the broad peaks, which correlate well with the diffraction pattern of hydroxyapatite (HA - $Ca_{10}(PO_4)_6(OH)_2$ - ICDD – 01-074-9761). After 24 hours, peaks matching dicalcium phosphate dihydrate (DCPD - $CaHPO_4.2H_2O$ - ICDD - 04-013-3344) were detected, which became noticeably more pronounced and sharper with increasing time.

Crystalline composition of tubes grown in PO_4^{3-} solutions of 0.25-1.5 M was also assessed after 30 days of ageing (Figure 3.8b). Peaks corresponding to both HA and DCPD were still present in the diffraction pattern of 0.5 M PO_4^{3-} precipitate (Figure 3.8b). Patterns collected for all other solution concentrations also matched to HA and DCPD references (Figure 3.8c). The phase composition of similarly prepared $CaPO_4$ tubes was previously determined to consist of a mixture of HA and DCPD phases [20, 22]. The resulting $CaPO_4$ phase is highly dependent on solution environment, with prominent factors, including pH and solubility, influencing the formation of minerals. Both of these phases are of biological importance within mammalian systems. For instance, HA is the primary mineral component of hard tissue and provides a physiological stable phase that can support the growth and proliferation of osteogenic bone forming cells [1, 27].

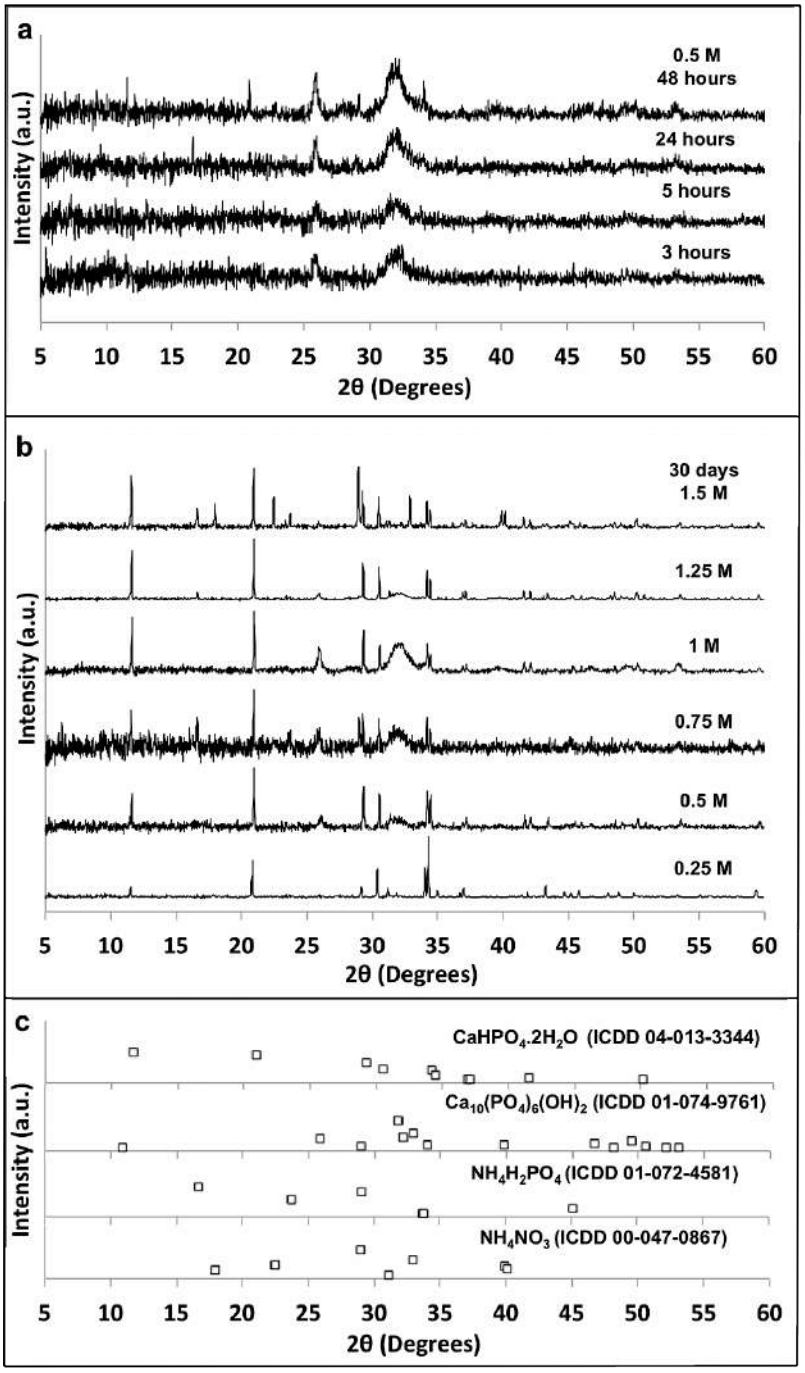

Figure 3.8 XRD diffraction patterns of the development of $CaPO_4$ precipitate grown for up to 48 hours in PO_4^{3-} 0.5 M solutions **(a)**, and after 30 days for $CaPO_4$ precipitates grown in 0.25-1.5 M PO_4^{3-} solutions **(b)**. ICDD reference patterns for $CaHPO_4.2H_2O$, $Ca_{10}(PO_4)_6(OH)_2$, $NH_4H_2PO_4$ and NH_4NO_3 matched to collected patterns **(c)**.

The presence of highly soluble phases was also detected; biphosphammite ($NH_4H_2PO_4$ - ICDD – 01-072-4581) in precipitates grown in 0.75 and 1.5 M PO_4^{3-} solutions, and nitrammite (NH_4NO_3 - ICDD – 00-047-0867) found in precipitates grown in 1.5 M PO_4^{3-} solutions (Figure 3.8b,c). The reagent salts employed in tube formation experiments provide ions required to produce such phases, which have not been fully washed away after precipitate extraction.

$CaPO_4$ tube structures are compositionally heterogeneous in nature during growth: a growing acidic Ca^{2+} rich core that evolves through an alkali PO_4^{3-} solution phase. Bilayer tube wall formation, best observed in micrographs of $CaPO_4$ tubes grown in 0.5 M PO_4^{3-} solution after 5 hours and 24 hours (Figure 3.7a,b), can therefore be explained. An amorphous outer wall of the $CaPO_4$ tubes is likely to comprise of low crystallinity HA precipitate which is the first to develop, before formation of an inner wall composed of DCPD since XRD patterns show that amorphous HA phase development precedes that of DCPD whilst also being consistent with the fact that chemical garden tube wall thickness develops inwards via propagating reaction-diffusion front and pH profile [18].

Similar to synthesis of mineral phases in many organisms, self-assembling $CaPO_4$ tubes evidently exhibit exceptional thermodynamic and kinetic control of precipitating amorphous and crystalline mineral phases [39]. As such, employment of a gel/solution model for creating structured mineral far surpasses many synthetic mineral synthesis pathways associated with

combining ionic solutions that result in the precipitation of mineral crystals, being as the precipitate does not possess regulated macroscopic structuring.

Elemental analysis was undertaken on tubes grown in 0.5 M PO_4^{3-} solutions to further understand tube wall composition using a μ-XRF mapping instrument. The scan area was selected in order to reveal the chemical composition along the tube length. The major elemental components of the tubes were calcium and phosphorus distinguished by Kα lines appearing in the expected vicinity of 3.69 keV and 2.01 keV, respectively and an additional line for Ca (Kβ at 4.01keV) was also observed (Figure S3.5). Mapping of the additional elements detected, namely Aluminum (Al), Silicon (Si), Sulphur (S), Chlorine (Cl), Potassium (K), Iron (Fe) and Copper (Cu) showed these elements to reside outside of the tube structure, originating from the background material upon which the tubule sample is supported.

Elemental maps of calcium (Figure 3.9a) and phosphorus (Figure 3.9b) were combined and a line scan collected across the diameter of the tube (Figure 3.9c). This allowed the Ca and P signal intensity to be plotted along the selected line scan. The outer tube wall was found to be relatively P rich (Figure 3.9c), which supports the proposed compositional hierarchy of a HA outer layer that develops into a DCPD inner layer. This biphasic ordering of compositional phases is obtained through exposure of developing precipitate to an acidic Ca^{2+} rich core and an alkaline PO_4^{3-} exterior, shedding light on how the creation of similar structures may be obtained from physical driving forces that are currently only possible in biological systems.

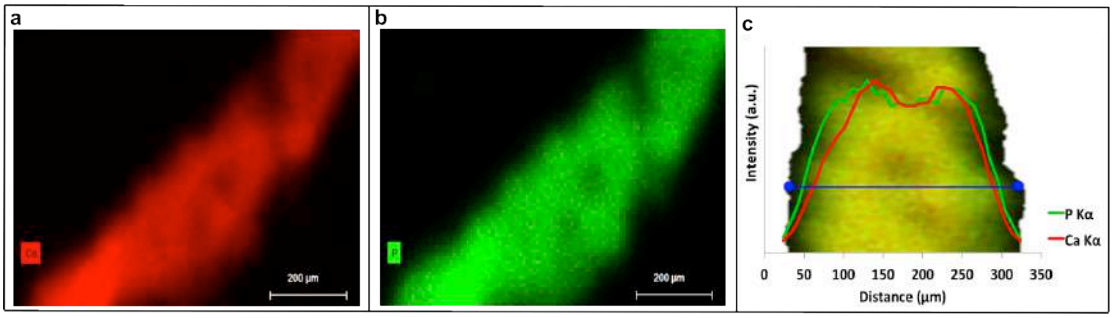

Figure 3.9 μ-XRF maps of a $CaPO_4$ tube structure grown in 0.5 M PO_4^{3-} solution. Elemental mapping of calcium **(a)** and phosphorous **(b)**. Elemental maps of calcium and phosphorus were combined; calcium and phosphorus Kα signal intensity of both elements was plotted from a line scan (blue) taken along the tube circumference **(c)**.

Acquiring control of these structuring processes may allow for designer $CaPO_4$ regenerative biomaterials. Desirable features include similar composition and architecture to naturally occurring dentinal tubules and Haversian canals capable of directing angiogenesis and tubulogenisis processes beyond synthetic systems through provision of high surface area, porosity and mass transport facilitation [28-32]. Promisingly, mineral tubular constructs can support the viability of cell cultures and further ways in which to incorporate biological cells during tube fabrication are active areas of research, bridging the gap between chemical gardens and tissue engineering applications [33, 40].

3.4 CONCLUSIONS

Long standing interest in chemical garden structures goes back as far as the 17th century, and stems from their resemblance to a number of

naturally occurring formations, such as hydrothermal vents upon the sea floor, and mineralised biological structures such as corals, shells and mammalian bone. Here we generate $CaPO_4$ tubules that resemble dentinal tubules and Haversian canals found in human hard tissues. This supports the notion that not only biological processes, but also physical driving forces play a fundamental role in biotic structuring.

Compiling results associated with the mechanism of $CaPO_4$ precipitation and tubular formation in a gel/solution set-up, it is evident there is a complex relationship between Ca^{2+} gel and PO_4^{3-} solution phases that allows for the formation of chemical garden structures. $CaPO_4$ tube morphology was only initiated by specific PO_4^{3-} solutions in a range of 0.5-1.5 M. A significant difference was found in gel response to either high or low solute environments of 1 and 5 M NaCl solutions, respectively within 30 minutes. Conditions that facilitate self-assembly of $CaPO_4$ tubular structures are an increase in gel mass followed by decrease, representative of an influx of solution into the gel driven by osmotic forces and subsequent release of Ca^{2+} rich fluid to relieve osmotic pressure, as supported by gel Ca^{2+} release and PO_4^{3-} ingress measurements. Although gels layered with 2 M experience substantial exodus of Ca^{2+} as determined by direct measurement and observation of gel pH change, $CaPO_4$ precipitate and tube formation are likely initially inhibited by ionic shielding.

Presence of contrasting pH environments, namely acidic Ca^{2+} rich fluid travelling through $CaPO_4$ tube structures and alkali PO_4^{3-} ion solution external to $CaPO_4$ tubes, drives the development of differing crystalline phases that

constitutes the observed hierarchical tube microstructure. Typical $CaPO_4$ tubes possessed a bilayer structure composed of outer layer of HA and an inner layer of DCPD. Mastering control over the generation of these structures may allow creation of regenerative biomaterials that are comparable to human tissue architecture and composition.

3.5 ASSOCIATED CONTENT

Supporting figures and equations are included in Appendix Part 2. Supporting movies are provided in Electronic Appendix Part 1.

3.6 REFERENCES

1. Wegst UGK, Bai H, Saiz E, Tomsia AP, Ritchie RO. Bioinspired structural materials. Nature Materials. 2014;14(1):23-36.

2. Pazzaglia UE, Congiu T, Raspanti M, Ranchetti F, Quacci D. Anatomy of the Intracortical Canal System: Scanning Electron Microscopy Study in Rabbit Femur. Clinical Orthopaedics and Related Research. 2009;467(9):2446-56.

3. Enderle JD, Bronzino JD. Introduction to Biomedical Engineering: Academic Press; 2012.

4. Earl JS, Leary RK, Perrin JS, Brydson R, Harrington JP, Markowitz K, et al. Characterization of dentine structure in three dimensions using FIB-SEM. Journal of Microscopy. 2010;240(1):1-5.

5. Marsh ME. Regulation of CaCO3 formation in coccolithophores. Comparative Biochemistry and Physiology Part B: Biochemistry and Molecular Biology. 2003;136(4):743-54.

6. Liu P-J. Burrow Architecture of the Spionid Polychaete Polydora villosa in the Corals Montipora and Porites. Zoological studies. 2000;39(1):47-54.

7. Cardoso SS, Cartwright JH, Checa AG, Sainz-Díaz CI. Fluid-flow-templated self-assembly of calcium carbonate tubes in the laboratory and in biomineralization: The tubules of the watering-pot shells, Clavagelloidea. Acta biomaterialia. 2016;43:338-47.

8. Frost HM. Bone remodelling dynamics: Thomas; 1963.

9. Maggiano IS, Maggiano CM, Clement JG, Thomas CDL, Carter Y, Cooper DML. Three-dimensional reconstruction of Haversian systems in human cortical bone using synchrotron radiation-based micro-CT: morphology and quantification of branching and transverse connections across age. Journal of Anatomy. 2016;228(5):719-32.

10. Arana-Chavez VE, Massa LF. Odontoblasts: the cells forming and maintaining dentine. The International Journal of Biochemistry & Cell Biology. 2004;36(8):1367-73.

11. Cartwright JHE, Piro O, Tuval I. Fluid dynamics in developmental biology: moving fluids that shape ontogeny. HFSP Journal. 2009;3(2):77-93.

12. van der Kraan PM, van den Berg WB. Osteophytes: relevance and biology. Osteoarthritis Cartilage. 2007;15(3):237-44.

13. Cartwright JH, Garcia-Ruiz JM, Novella ML, Otalora F. Formation of Chemical Gardens. J Colloid Interface Sci. 2002;256:351-9.

14. Barge LM, Cardoso SS, Cartwright JH, Cooper GJ, Cronin L, De Wit A, et al. From Chemical Gardens to Chemobrionics. Chem Rev. 2015;115(16):8652-703.

15. Cartwright JH, Escribano B, Sainz-Daz CI. Chemical-garden formation, morphology, and composition. I. Effect of the nature of the cations. Langmuir. 2011;27(7):3286-93.

16. Coatman RD, Thomas NL, Double DD. Studies of the growth of "silicate gardens" and related phenomena. Journal of Materials Science 1980;15:2017-26.

17. Barge LM, Doloboff IJ, White LM, Stucky GD, Russell MJ, Kanik I. Characterization of iron-phosphate-silicate chemical garden structures. Langmuir. 2012;28(8):3714-21.

18. Steinbock O, Cartwright JHE, Barge LM. The fertile physics of chemical gardens. Physics Today. 2016;69(3):44-51.

19. Hazlehurst TH. Structural Precipitates: The Silicate Garden Type. Journal of Chemical Education. 1941;18:286-9.

20. Kamiya K, Yoko T, Tanaka K, Fujiyama Y. Growth of fibrous hydroxyapatite in the gel system. Journal of Materials Science. 1989;24(3):827-32.

21. Steenbjerg Ibsen CJ, Mikladal BF, Bjornholt Jensen U, Birkedal H. Hierarchical tubular structures grown from the gel/liquid interface. Chemistry. 2014;20(49):16112-20.

22. Tanahashi M, Kamiya K, Suzuki T, Nasu H. Fibrous hydroxyapatite grown in the gel system: effects of pH of the solution on the growth rate and morphology. J Mater Sci: Mater Med. 1992;3(1):48-53.

23. Haudin F, Cartwright JH, Brau F, De Wit A. Spiral precipitation patterns in confined chemical gardens. Proc Natl Acad Sci U S A. 2014;111(49):17363-7.

24. Thouvenel-Romans S, van Saarloos W, Steinbock O. Silica tubes in chemical gardens: Radius selection and its hydrodynamic origin. Europhys Lett. 2004;67(1):42-8.

25. Roszol L, Steinbock O. Controlling the wall thickness and composition of hollow precipitation tubes. Phys Chem Chem Phys. 2011;13(45):20100-3.

26. Batista BC, Steinbock O. Chemical gardens without silica: the formation of pure metal hydroxide tubes. Chem Commun (Camb). 2015;51(65):12962-5.

27. Ohgushi H, Dohi Y, Tamai S, Tabata S. Osteogenic differentiation of marrow stromal stem cells in porous hydroxyapatite ceramics. Journal of Biomedical Materials Research. 1993;27(11):1401-7.

28. Lovett M, Lee K, Edwards A, Kaplan DL. Vascularization Strategies for Tissue Engineering. Tissue Engineering Part B, Reviews. 2009;15(3):353-70.

29. Nguyen LH, Annabi N, Nikkhah M, Bae H, Binan L, Park S, et al. Vascularized Bone Tissue Engineering: Approaches for Potential Improvement. Tissue Engineering Part B, Reviews. 2012;18(5):363-82.

30. Hwang K-J, Hwang C-H, Lee I-H, Kim T, Jin S, Park J-Y. Synthesis and characterization of hollow metal oxide micro-tubes using a biomaterial template. Biomass and Bioenergy. 2014;68:62-6.

31. Iruela-Arispe ML, Beitel GJ. Tubulogenesis. Development (Cambridge, England). 2013;140(14):2851-5.

32. Raghavan S, Nelson CM, Baranski JD, Lim E, Chen CS. Geometrically Controlled Endothelial Tubulogenesis in Micropatterned Gels. Tissue Engineering Part A. 2010;16(7):2255-63.

33. Punia K, Bucaro M, Mancuso A, Cuttitta C, Marsillo A, Bykov A, et al. Rediscovering Chemical Gardens: Self-Assembling Cytocompatible Protein-Intercalated Silicate-Phosphate Sponge-Mimetic Tubules. Langmuir. 2016;32(34):8748-58.

34. Makki R, Al-Humiari M, Dutta S, Steinbock O. Hollow Microtubes and Shells from Reactant-Loaded Polymer Beads. Angewandte Chemie International Edition. 2009;48(46):8752-6.

35. Thouvenel-Romans S, Pagano JJ, Steinbock O. Bubble guidance of tubular growth in reaction-precipitation systems. Physical Chemistry Chemical Physics. 2005;7(13):2610-5.

36. Deutsch WJ. Groundwater Geochemistry: Fundamentals and Applications to Contamination: CRC Press; 1997.

37. Jowsey J. Studies of Haversian systems in man and some animals. Journal of Anatomy. 1966;100(Pt 4):857-64.

38. Cooper DM, Thomas CD, Clement JG, Turinsky AL, Sensen CW, Hallgrimsson B. Age-dependent change in the 3D structure of cortical porosity at the human femoral midshaft. Bone. 2007;40(4):957-65.

39. Addadi L, Weiner S. Control and Design Principles in Biological Mineralization. Angew Chem Int Ed Engl. 1992;31:153-69.

40. Batista BC, Cruz P, Steinbock O. Self-Alignment of Beads and Cell Trapping in Precipitate Tubes. ChemPhysChem. 2015;16(11):2299-303.

Chapter 4. Interfacial mineral fusion and tubule entanglement as a means to harden a bone augmentation material

Adapted from:

Hughes EAB, Cox SC, Cooke ME, Williams RL, Hall TJ, Grover LM. Interfacial mineral fusion and tubule entanglement as a means to harden a bone augmentation material. *Submitted.*

Authors: Erik A. B. Hughes[1], Dr. Sophie C. Cox[1], Megan E. Cooke[1,2], Dr. Richard L. Williams[1], Thomas J. Hall[1], and Prof. Liam M. Grover[1]

Affiliations: [1]School of Chemical Engineering, University of Birmingham, Edgbaston, B15 2TT, UK and [2]Institute of Inflammation and Ageing, MRC Musculoskeletal Ageing Centre, QE Hospital, B15 2TT, UK

Corresponding author: Prof. Liam Grover (l.m.grover@bham.ac.uk)

Table of contents (TOC) image

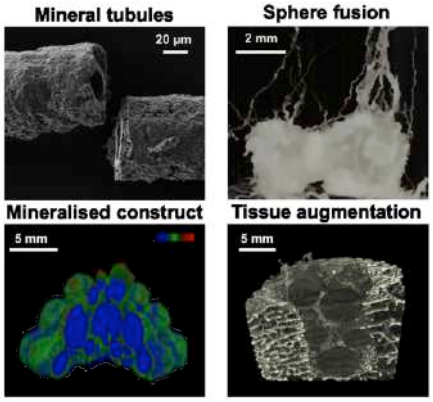

4.0 ABSTRACT

A new bone augmenting material is reported which is formed from calcium-loaded hydrogel-based spheres. On immersion of these spheres in a physiological medium, they become surrounded with a sheath of precipitate, which ruptures due to a build-up in osmotic pressure, resulting in the formation of mineral tubes that protrude from the sphere surface. When brought into close contact with one another, these spheres become fused through the entanglement and subsequent interstitial mineralisation of the mineral tubules. This is the first report of a bioceramic material that is formed in its entirety *in situ* and is therefore likely to provide a better proxy for biological mineral than other existing synthethic alternatives to bone grafts.

4.1 INTRODUCTION

A range of synthetic materials have been developed that are capable of filling hard tissue defects to overcome the issues that are often associated with autologous tissue harvesting, such as local tissue morbidity and lack of availability [1, 2]. In particular, there have been many ceramic-based materials used for hard tissue augmentation. Calcium phosphate and sulphate-based products are available commercially, but are yet to replace autograft as the so-called “gold-standard” [3, 4]. The ceramic materials used for the augmentation of hard tissues are often produced using high-temperature treatment processes, meaning that they are of high-crystallinity and relatively low specific surface area [5-7]. Consequently, synthetic ceramic bone replacements often bare little resemblance to native bone mineral, which is

predominantly nano-crystalline structured hydroxyapatite (HA, $Ca_5(PO_4)_3OH$) that is compositionally poorly crystalline overall [8]. Even in the case of cements, which harden through reprecipitation in the body, much of the hardened structure is formed in the presence of excess micro crystalline reactant [9, 10]. Moreover, conventional regenerative materials do not feature channels to support the penetration of surrounding vascular and nervous networks [11, 12]. The level of structuring that is possible with synthetic alternatives to bone graft is limited to the production of biomimetic corals and sponge-like structures that provide an interporous network for bone regeneration, but replicate none of the microstructural organisation of hard tissue at the osteonal level [13-15]. Hard tissues exhibit precisely defined hierarchical architectures, with organisation from the molecular level through to the macroscale. It is this well preserved architecture that is critical to the extraordinary mechanical performance of bone – which is stronger and tougher per unit weight than steel [13]. One preserved feature of hard tissue is the presence of intricate tubular networks, such as canaliculi, Haversian and Volkman's canals found in mature bone, as well as dentinal tubules within teeth, that are critical to the function of such tissues [16-18]. Tubular channels like these are essential for transporting chemicals, gases and nutrients in order to maintain the viability of cells cocooned within typically dense mineralised tissue. Mimicking the natural structural features of bone is a major challenge but one that is subject to substantial research effort. A prerequisite to facilitating the development of vascular networks throughout hard tissue scaffolds may be the provision of tubular structures similar in nature to those

found in mineralised tissues. It has been shown that mineralised tubular frameworks provide an ideal framework to mediate revascularisation of bone *in vivo* [19].

Mineral tubes similar to those found in bone and teeth may be formed using a system that is analogous to a chemical garden, where hollow tubular precipitates form at the interface between a cationic seed crystal and an anionic solution [20, 21]. These structures have been likened to a range of tubular minerals found throughout nature [22, 23]. Surprisingly, there is relatively little work that examines the use of such systems for biotechnology applications despite the fact that they have been shown to support the entrapment and growth of cells [24, 25]. With the exception of calcium silicates, phosphates and carbonates, the majority of salts traditionally generated in chemical gardens would not be compatible with implantation into the body, including but not limited to cobalt, copper, iron, manganese and nickel compounds [20-22, 24, 26]. There has recently been work that has shown it is possible to produce biologically relevant calcium phosphate structures at the interface between a cation loaded hydrogel and anionic solution [27-30]. Indeed, we recently reported on the formation of tubular calcium phosphate that resembles tubular architectures found in bone both structurally and compositionally [30].

This paper describes the production of a hardening material formed from hydrogel-based spheres that can be packed into defects similar to those encountered *in vivo*. On immersion in phosphate rich physiological media, a sheath of precipitate forms around the spheres, which ruptures due to an

increase in osmotic pressure. This release of pressure drives the formation of tubular mineral from the gel surface. The mineral tubules become intermeshed, which ultimately causes the spheres to fuse. Formation of the calcium loaded spheres and their capacity to fill an *ex-vivo* defect in retrieved human bone, in addition to the morphology, structure and composition of the precipitated mineral phase, are investigated.

4.2 EXPERIMENTAL METHODS

4.2.1 Calcium loaded hydrogel fabrication and mineral initiation

Calcium loaded gels were made by adding 5 wt% agar powder (for microbiology, Sigma-Aldrich, UK) to 1 M calcium solutions prepared from calcium nitrate tetrahydrate crystals (99 %, ACS reagent, Sigma-Aldrich, UK) and distilled water before heating the mixture to 80-90 ^{o}C. For conventional set-up, a layer of gel was set in clear cylindrical containers and allowed to cool to room temperature. For calcium loaded spheres, warm gel was added drop-wise to an insulated chamber of liquid nitrogen. Spheres were collected after dissipation of the nitrogen. Self-mineralisation was initiated upon gel surfaces, calcium loaded sphere constructs, and within an *ex vivo* bone defect using phosphate solutions prepared by dissolving crystals of dibasic ammonium phosphate (≥ 98.0 %, reagent grade, Sigma-Aldrich, UK) at concentrations between 500 mM and 1 M.

4.2.2 Human tissue model

Bone tissue was collected from patients undergoing elective knee replacement surgery. The United Kingdom National Research Ethics Service (East of Scotland Research Ethics Service) provided ethical approval (11/ES/1044). Tissues were washed using phosphate buffered saline (PBS) (calcium and magnesium free, Sigma-Aldrich, UK) before defects 10 mm wide and a minimum of 10 mm deep were introduced using a surgical drill. Calcium loaded spheres were gently packed into defect spaces and self-mineralisation initiated as detailed above.

4.2.3 Scanning electron microscopy (SEM)

Samples were placed on an aluminum stub using double-sided sticky carbon discs. Gold sputter coating was performed prior to imaging using a K550X sputter coater (Quorum Technologies, U.K.). SEM images were then acquired using an EVO MA 10 scanning electron microscope operating at 10 kV (Carl Zeiss AG, Germany).

4.2.4 Micro- X-Ray Fluorescence (μ-XRF)

Specimens were elementally mapped using an M4 Tornado instrument (Bruker, U.S.A.). Measurement settings of 20 ms/pixel over 25 frames in the case of Figure 1f, and 2 frames in the case of Figure 2b and 3c, were employed with the instrument operating at 50 kV with anode current of 300 mA. During measurements, the chamber was maintained at 500 mbar in the case of Figure 1e.

4.2.5 Micro- computed tomography (*μ*-CT) scanning

Samples were transferred to a sealed low X-ray attenuation tube. Structures were scanned using a Skyscan1172 microcomputed tomography (*μ*-CT) instrument (Bruker, U.S.A) with 60 kV maximum X-ray energy, 6 W beam power, 2000 ms exposure per projection, and 12.44 *μ*m pixel size. Slice data was reconstructed using *NRecon* (Version 1.6.10, Bruker) and visualised using *CTVox* (Version 3.0, Bruker). For self-mineralising sphere pyramid constructs, greyscale images were artificially coloured by assigning blue, green, and red transfer functions to grey scale ranges matching the calcium loaded spheres (blue) and mineralised regions (green and red). For the mineralised human defect model, an opacity transfer function was applied to best segment the greyscale range corresponding to the tubules from the rest of the structure to render 3D images of deposited mineral within the defect.

4.3 RESULTS AND DISCUSSION

The generation of tubule structures results from the exposure of calcium loaded agarose layered with a phosphate rich solution, which ultimately produces a forest of hollow white precipitate tubes (Figure 4.1a). Initially, a precipitate is formed at the gel-liquid interface, which impedes dissolution and creates an osmotic pressure. When the osmotic pressure causes localised rupture of the precipitate layer, calcium ions are able to diffuse into the liquid phases where a tubular calcium phosphate based precipitate forms [30, 31]. Growth of these tubes is maintained through cyclic build-ups in osmotic pressure and release, which drives calcium ions through

the established tubule to the tip where it ruptures and a new section of tubule is formed [30, 31]. The mineral from which these tubules are formed is a poorly crystalline calcium phosphate, similar to that found in the body.

The tubular precipitate did not only form on planar surfaces, but also formed when spheres of hydrogel loaded with a 1M calcium nitrate solution were placed into a 0.5 M phosphate solution. The spheres were produced through the drop-wise addition of hot (80 - 90^{o}C) calcium-loaded agarose gel mixture through a 2 mm wide pipette aperture into a reservoir of liquid nitrogen (Figure 4.1b). Upon contact with the liquid nitrogen, the gel droplets quickly solidified through the inverse Leidenfrost effect [32]. The resulting spheres had an average diameter of 3.7 ± 0.4 mm (n = 10). The use of this method of manufacture meant that spherical agarose particles could be produced loaded with relatively high concentrations of calcium ions (>1 M), which would be very difficult to achieve using standard processing methods or soaking pre-formed spheres in a cation containing solutions [33]. Agarose was selected as the soft material of choice as a consequence of its neutral charge, meaning that it does not impeded diffusion of the calcium ions. Furthermore, others have reported the use of mineralised agarose for bone augmentation [34, 35].

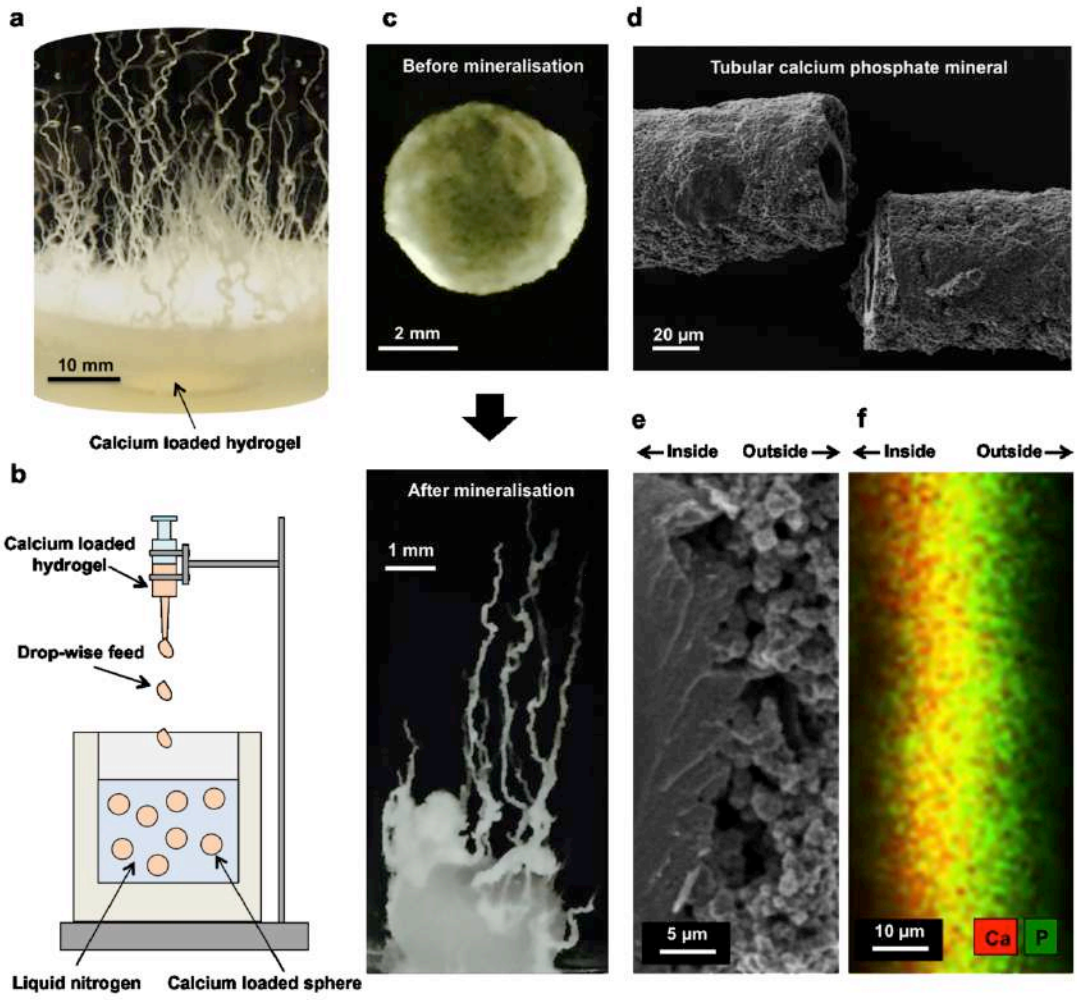

Figure 4.1 (a) Conventional experimental set-up (Reported in reference 30), which produces calcium phosphate tubules that are structurally and compositionally similar to bone, providing the starting point for the work reported herein. **(b)** Schematic of fabrication method of calcium-loaded spheres, involving drop-wise addition of calcium loaded agarose hydrogel into a reservoir of liquid nitrogen. **(c)** Calcium loaded spheres before and after mineralisation, showing the ejection of tubular calcium phosphate mineral. **(d)** SEM micrograph showing the tubule microstructure, consisting of a bilayer tubule wall surrounding a hollow core. **(e)** SEM micrograph of tube wall bilayer structuring. **(f)** μ-XRF elemental mapping of a calcium phosphate tubule

cross-section (Kα channels for calcium (red) and phosphorous (green) shown).

When the calcium loaded spheres were immersed in phosphate solutions, tubules precipitated around the periphery of the particles but grow preferentially upward due to buoyancy effects (Figure 4.1c) [21]. Altering the concentration of the metal and reactive counter ions directly influences the kinetic driving forces of self-assembly of the tube like structures by changing osmotic, diffusion and pH gradients within the material. This influences the gross morphology of the tubes and can also be used to tailor the rate of formation. Increasing phosphate solution concentration from 500 mM to 1 M allows control over mineral tubular growth rate between 0.3 mm/min (18 mm/h) to 0.5 mm/min (30 mm/h) (Figure S4.1).

The tubules typically exhibit diameters between 100 and 150 μm, which is ideal for ingress of osteogenic cells (Figure 4.1d) [36]. They also exhibit a hierarchical bilayer wall structure comprised of low crystallinity HA ($Ca_5(PO_4)_3OH$) and dicalcium phosphate dihydrate (DCPD, $CaHPO_4.2H_2O$) (Figures 4.1e and S4.2). This structure develops inwards as a consequence of the contrasting environments inside and outside of the tube resulting in a steep concentration gradient of reactive species across the tube wall. This ultimately results in a calcium rich inner wall, and phosphate rich outer wall (Figure 4.1f) [37].

In the presence of phosphate, calcium loaded spheres placed in close contact with one another fuse through the formation of mineral and the

development of interweaving tubes at their periphery (Figure 4.2a). The interactions formed between the spheres were of sufficient strength to allow for the fusion of multiple spheres to form a larger structure (Movie S4.1).

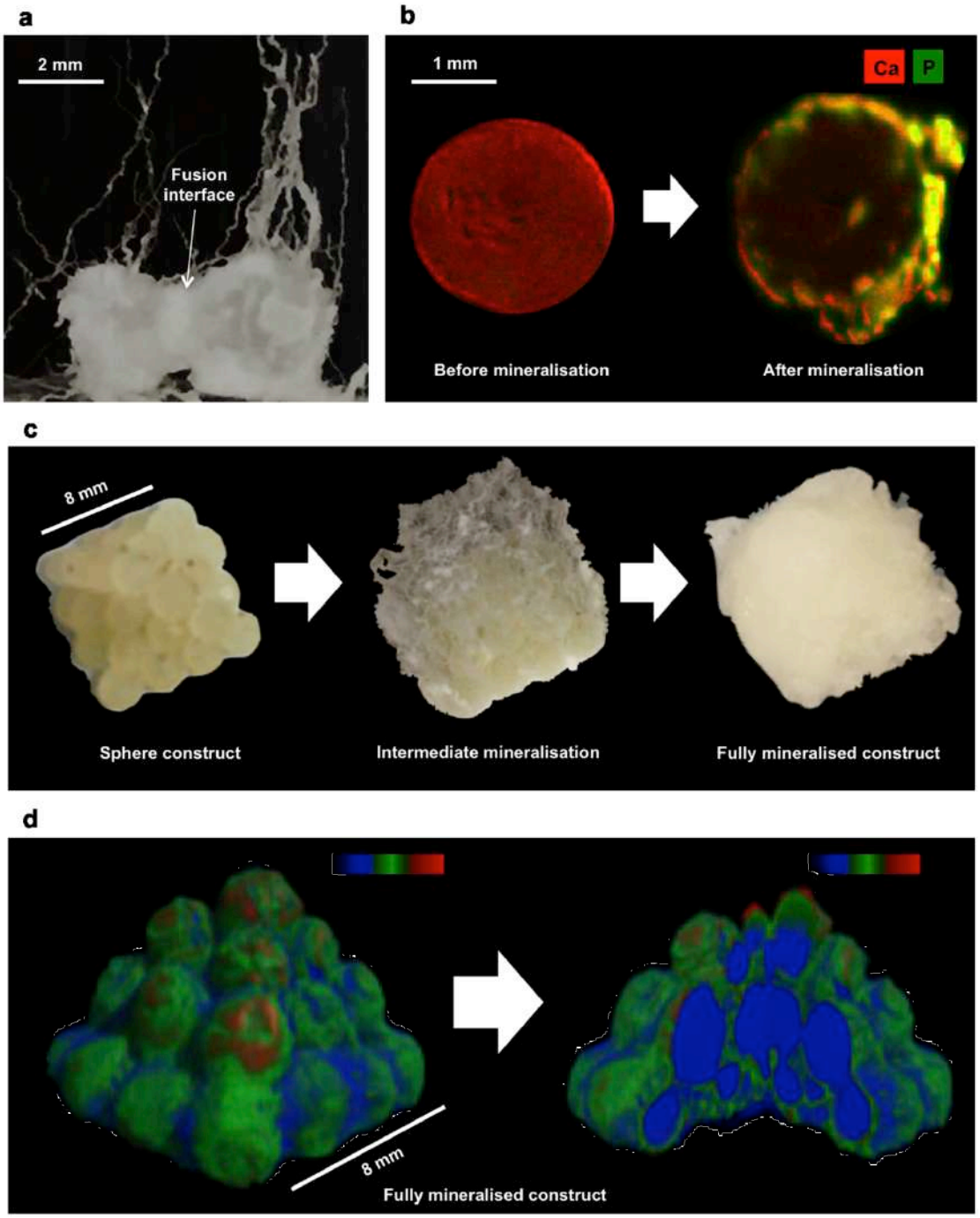

Figure 4.2 (a) Fusion of two calcium loaded spheres in close proximity to one another during self-mineralisation. **(b)** μ-XRF elemental mapping of a calcium loaded sphere cross-section before and after inducing self-mineralisation (Kα

channels for calcium (red) and phosphorous (green) shown) **(c)** Calcium loaded sphere pyramid construct before and after triggering self-mineralisation, leading to complete unification. **(d)** μ-CT of calcium loaded sphere pyramid after submersion in phosphate solution. Colour scales in-set represent an increase in relative density of material from blue (calcium loaded sphere) to green and red (mineral).

Elemental mapping using micro X-ray fluorescence (μ-XRF) confirmed that the particles were united by a calcium phosphate phase (Figure 4.2b). It was possible to assemble the gel spheres into relatively complex geometries, such as the pyramid shown in Figure 4.2c. 3D micro-computed tomography (μ-CT) reconstructions of this structure show that mineral coverage (red and green) occurs extensively across the surfaces of hydrogel spheres (blue), and even in the centre of the structure (Figure 4.2d).

To demonstrate that this approach could be used for the augmentation of a hard tissue defect, a cylindrical defect approximately 10 mm wide and 15 mm deep was introduced into an *ex vivo* human tissue model which was packed with calcium loaded spheres (Figure 4.3a). The filled defect was then placed into a phosphate rich medium (1 M phosphate solution) and mineral was observed to form rapidly across the surface with the formation of tubes becoming apparent soon thereafter.

After 24h this structure could be inverted and irrigated with water without a loss of mechanical integrity (Movie S4.2). μ-CT revealed the extent of mineral deposition within the defect (Figure 4.3b). Cross-sectional images

show mineral around the surface of spheres and tubular structures within the defect, filling the inter particulate spaces with a mineral phase.

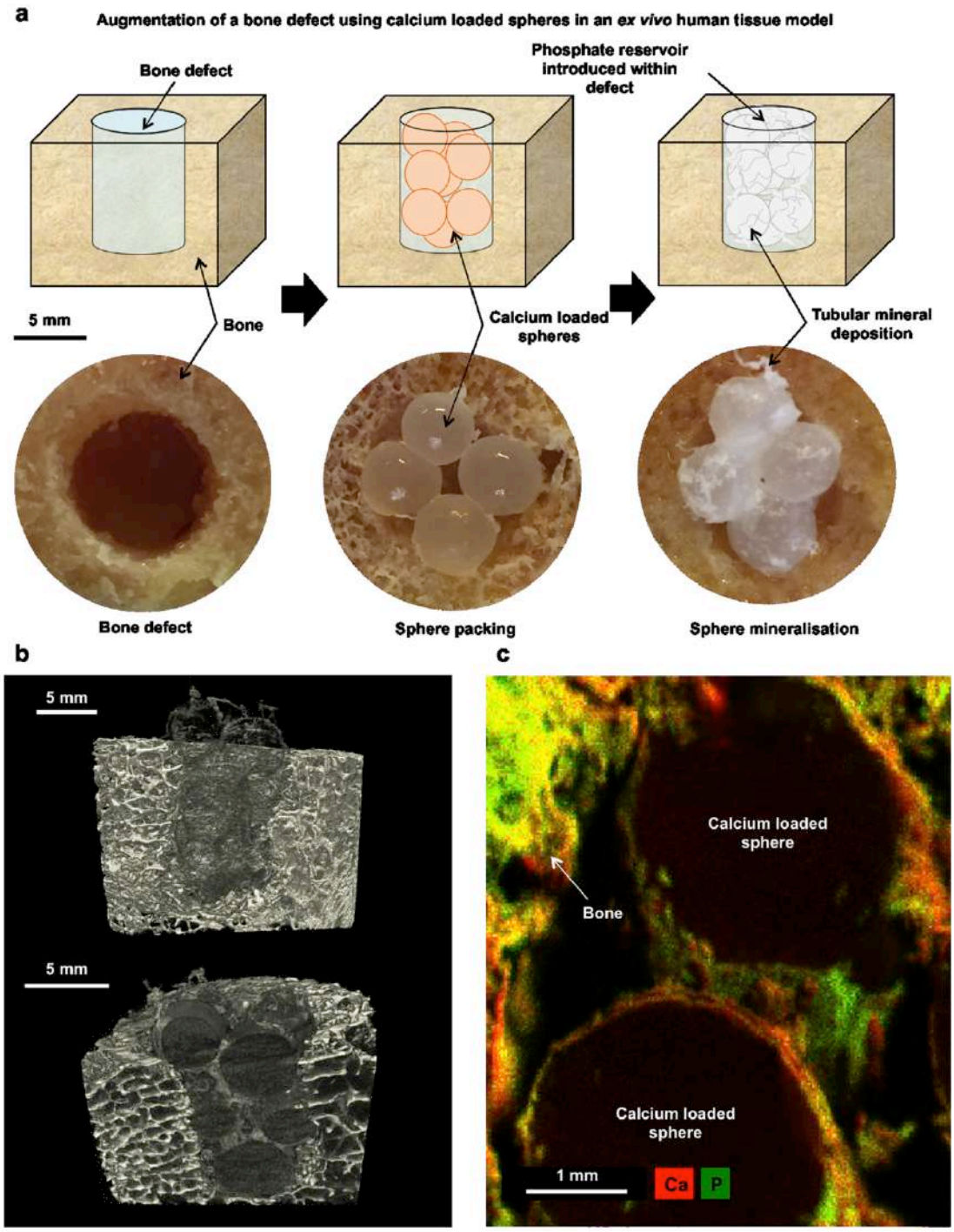

Figure 4.3 (a) Schematic of calcium loaded spheres augmenting an *ex vivo* human bone defect, showing an empty bone defect, the packing of spheres to augment the defect, and triggering of self-mineralisation with 1 M phosphate solution. **(b)** μ-CT of human hard tissue model containing mineralised calcium

loaded spheres that have deposited mineral and tubular structures within the defect. **(c)** μ-XRF elemental mapping of a cross-section of the human hard tissue defect (Kα channels for calcium (red) and phosphate (green) shown).

From μ-CT examination, the interfaces between the spheres and the mineral deposited are extremely difficult to differentiate from the apposing bone. μ-XRF analysis demonstrates that the elemental composition of precipitated calcium phosphate mineral is similar to the surrounding tissue, also making it difficult to distinguish a clear interface between bone and the spheres (Figures 4.3c and S4.3).

4.4 CONCLUSIONS

Inspired by processes that are able to mimic natural tubular mineral structures, we have developed a device capable of augmenting a hard tissue defect through the production of tubular mineral. The material consists of calcium loaded spheres manufactured using a process that allows for the incorporation of high concentrations of calcium. Immersion of these spheres in physiologically relevant solutions rich in phosphate stimulates tube formation, which means that they could be ideal for use in biological environments. Compared with the majority of synthetic bone substitutes that are typically dense and highly crystalline, this system enables: (1) the formation of tubular calcium phosphate mineral that is structurally and compositionally akin to the tubular features found in bone and tooth, providing a structured osteogenic scaffold, (2) mineral formation occurs *in situ* in the absence of microcrystalline

reactant, facilitating a low-crystallinity product comparable to the surrounding hard tissue, and (3) mineral synthesis can be tuned by the adjustment of precipitation parameters, enabling physical properties such as fusion time of spheres to one another and to bone to be modified. The microscale structural features of the mineral phase may also enable better vascularisation of the implant [19].

In summary, we present a strategy for directly delivering hierarchical tubular mineral into hard tissue defects using spheres of agarose hydrogel loaded with calcium. In phosphate solutions, these spherical structures fuse, forming a solid through the intermeshing of mineral tubules that are expelled from the surface of the soft material.

4.5 ASSOCIATED CONTENT

Supporting figures are included in Appendix Part 3. Supporting movies are provided in Electronic Appendix Part 2.

4.6 REFERENCES

1. LaPrade RF, Botker JC. Donor-site morbidity after osteochondral autograft transfer procedures. Arthroscopy: The Journal of Arthroscopic & Related Surgery. 2004;20(7):e69-e73.

2. Calori GM, Colombo M, Mazza EL, Mazzola S, Malagoli E, Mineo GV. Incidence of donor site morbidity following harvesting from iliac crest or RIA graft. Injury. 2014;45 Suppl 6:S116-20.

3. Dorozhkin SV. Calcium orthophosphate bioceramics. Ceramics International. 2015;41(10):13913-66.

4. Shegarfi H, Reikeras O. Bone transplantation and immune response. Journal of Orthopaedic Surgery. 2009;17(2):206-11.

5. Hazar Yoruç AB, Karakaş A, Koyun A, Yildiz T. Comparison of Properties of Hydroxyapatite Powders Synthesized by Chemical and Biomimetic Techniques. Acta Physica Polonica A. 2012;121(1):233-5.

6. Giraldo-Betancur AL, Espinosa-Arbelaez DG, Real-López Ad, Millan-Malo BM, Rivera-Muñoz EM, Gutierrez-Cortez E, et al. Comparison of physicochemical properties of bio and commercial hydroxyapatite. Current Applied Physics. 2013;13(7):1383-90.

7. Prakasam M, Locs J, Salma-Ancane K, Loca D, Largeteau A, Berzina-Cimdina L. Fabrication, Properties and Applications of Dense Hydroxyapatite: A Review. J Funct Biomater. 2015;6(4):1099-140.

8. Querido W, Rossi AL, Campos APC, Rossi AM, Farina M. Does crystallinity of extracted bone mineral increase over storage time? Materials Research. 2013;16(5):970-4.

9. Brunner TJ, Grass RN, Bohner M, Stark WJ. Effect of particle size, crystal phase and crystallinity on the reactivity of tricalcium phosphate cements for bone reconstruction. Journal of Materials Chemistry. 2007;17(38):4072.

10. Chow LC. Next generation calcium phosphate-based biomaterials. Dent Mater J. 2009;28(1):1-10.

11. Lovett M, Lee K, Edwards A, Kaplan DL. Vascularization Strategies for Tissue Engineering. Tissue Engineering Part B, Reviews. 2009;15(3):353-70.

12. Nguyen LH, Annabi N, Nikkhah M, Bae H, Binan L, Park S, et al. Vascularized Bone Tissue Engineering: Approaches for Potential Improvement. Tissue Engineering Part B, Reviews. 2012;18(5):363-82.

13. Wegst UGK, Bai H, Saiz E, Tomsia AP, Ritchie RO. Bioinspired structural materials. Nature Materials. 2014;14(1):23-36.

14. Green DW, Lai WF, Jung HS. Evolving marine biomimetics for regenerative dentistry. Mar Drugs. 2014;12(5):2877-912.

15. Green DW, Ben-Nissan B, Yoon KS, Milthorpe B, Jung HS. Natural and Synthetic Coral Biomineralization for Human Bone Revitalization. Trends Biotechnol. 2017;35(1):43-54.

16. Cooper DM, Thomas CD, Clement JG, Turinsky AL, Sensen CW, Hallgrimsson B. Age-dependent change in the 3D structure of cortical porosity at the human femoral midshaft. Bone. 2007;40(4):957-65.

17. Maggiano IS, Maggiano CM, Clement JG, Thomas CDL, Carter Y, Cooper DML. Three-dimensional reconstruction of Haversian systems in human cortical bone using synchrotron radiation-based micro-CT: morphology and quantification of branching and transverse connections across age. Journal of Anatomy. 2016;228(5):719-32.

18. Jowsey J. Studies of Haversian systems in man and some animals. Journal of Anatomy. 1966;100(Pt 4):857-64.

19. Krauss S, Wagermaier W, Estevez JA, Currey JD, Fratzl P. Tubular frameworks guiding orderly bone formation in the antler of the red deer (Cervus elaphus). J Struct Biol. 2011;175(3):457-64.

20. Coatman RD, Thomas NL, Double DD. Studies of the growth of "silicate gardens" and related phenomena. Journal of Materials Science 1980;15:2017-26.

21. Cartwright JH, Escribano B, Sainz-Daz CI. Chemical-garden formation, morphology, and composition. I. Effect of the nature of the cations. Langmuir. 2011;27(7):3286-93.

22. Barge LM, Cardoso SS, Cartwright JH, Cooper GJ, Cronin L, De Wit A, et al. From Chemical Gardens to Chemobrionics. Chem Rev. 2015;115(16):8652-703.

23. Cardoso SS, Cartwright JH, Checa AG, Sainz-Díaz CI. Fluid-flow-templated self-assembly of calcium carbonate tubes in the laboratory and in biomineralization: The tubules of the watering-pot shells, Clavagelloidea. Acta Biomaterialia. 2016;43:338-47.

24. Punia K, Bucaro M, Mancuso A, Cuttitta C, Marsillo A, Bykov A, et al. Rediscovering Chemical Gardens: Self-Assembling Cytocompatible Protein-Intercalated Silicate-Phosphate Sponge-Mimetic Tubules. Langmuir. 2016;32(34):8748-58.

25. Batista BC, Cruz P, Steinbock O. Self-Alignment of Beads and Cell Trapping in Precipitate Tubes. ChemPhysChem. 2015;16(11):2299-303.

26. Barge LM, Doloboff IJ, White LM, Stucky GD, Russell MJ, Kanik I. Characterization of iron-phosphate-silicate chemical garden structures. Langmuir. 2012;28(8):3714-21.

27. Kamiya K, Yoko T, Tanaka K, Fujiyama Y. Growth of fibrous hydroxyapatite in the gel system. Journal of Materials Science. 1989;24(3):827-32.

28. Tanahashi M, Kamiya K, Suzuki T, Nasu H. Fibrous hydroxyapatite grown in the gel system: effects of pH of the solution on the growth rate and morphology. J Mater Sci: Mater Med. 1992;3(1):48-53.

29. Steenbjerg Ibsen CJ, Mikladal BF, Bjornholt Jensen U, Birkedal H. Hierarchical tubular structures grown from the gel/liquid interface. Chemistry. 2014;20(49):16112-20.

30. Hughes EA, Williams RL, Cox SC, Grover LM. Biologically Analogous Calcium Phosphate Tubes from a Chemical Garden. Langmuir. 2017;33(8):2059-67.

31. Cartwright JH, Garcia-Ruiz JM, Novella ML, Otalora F. Formation of Chemical Gardens. J Colloid Interface Sci. 2002;256:351-9.

32. Adda-Bedia M, Kumar S, Lechenault F, Moulinet S, Schillaci M, Vella D. Inverse Leidenfrost Effect: Levitating Drops on Liquid Nitrogen. Langmuir. 2016;32(17):4179-88.

33. Makki R, Al-Humiari M, Dutta S, Steinbock O. Hollow Microtubes and Shells from Reactant-Loaded Polymer Beads. Angewandte Chemie International Edition. 2009;48(46):8752-6.

34. Watanabe J, Kashii M, Hirao M, Oka K, Sugamoto K, Yoshikawa H, et al. Quick-forming hydroxyapatite/agarose gel composites induce bone regeneration. Journal of Biomedical Materials Research Part A. 2007;83(3):845-52.

35. Hu J, Zhu Y, Tong H, Shen X, Chen L, Ran J. A detailed study of homogeneous agarose/hydroxyapatite nanocomposites for load-bearing bone tissue. Int J Biol Macromol. 2016;82:134-43.

36. Cerroni L, Filocamo R, Fabbri M, Piconi C, Caropreso S, Condò SG. Growth of osteoblast-like cells on porous hydroxyapatite ceramics: an in vitro study. Biomolecular Engineering. 2002;19:119-24.

37. Roszol L, Steinbock O. Controlling the wall thickness and composition of hollow precipitation tubes. Phys Chem Chem Phys. 2011;13(45):20100-3.

Chapter 5. Development of a covalently bonded hydroxyapatite and poly(ether ether ketone) composite

Adapted from:

Hughes EAB, Parkes A, Williams RL, Jenkins MJ, Grover LM. Development of a covalently bonded hydroxyapatite and PEEK composite. *Submitted.*

Authors: Erik A. B. Hughes[1], Andrew Parkes[2], Dr. Richard L. Williams[1], Dr. Mike J. Jenkins[2], and Prof. Liam M. Grover[1]

Affiliations: [1]School of Chemical Engineering, University of Birmingham, Edgbaston, B15 2TT, UK and [2]School of Metallurgy and Materials, University of Birmingham, Edgbaston, B15 2TT, UK

Corresponding author: Prof. Liam Grover (l.m.grover@bham.ac.uk)

Table of contents (TOC) image

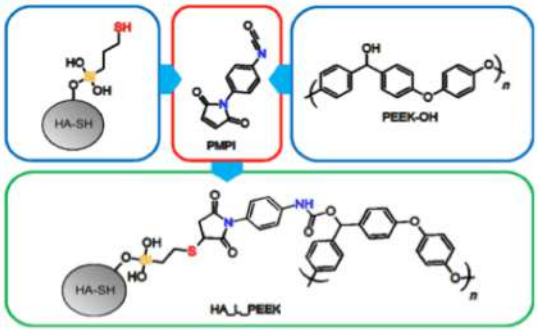

5.0 ABSTRACT

Novel hydroxyapatite (HA) loaded poly(ether ether ketone) (PEEK) composites are now used to manufacture commercially available spinal fusion devices. In this work, the interfacial interactions between HA and PEEK are improved beyond mechanical and physiochemical interlocking by creating covalent bonds between dissimilar phases. HA particulates were coated with (3-Mercaptopropyl) triethoxysilane (MPTES) introducing thiol moiety (-SH). PEEK ketone groups (C=O) were reduced to hydroxyl groups (-OH). HA-SH and PEEK-OH derivatives respectively were then coupled using a heterobifunctional linker. Compared to non-linked materials (HA_PEEK), covalently linked composites (HA_L_PEEK), loaded with 2.5 wt% HA, possessed an improved flexural modulus. No significant difference was between between the flexural modulus of PEEK and HA_L_PEEK ($p = 0.127$). However, HA_PEEK was significantly weakened ($p = 0.026$). Mechanical properties of composites are augmented by a reduction in HA debonding and micro crack development, in addition to enhanced load transfer between phases.

5.1 INTRODUCTION

Poly(ether ether ketone) (PEEK) is a high performance semi-crystalline engineering polymer that has been implemented across a range of industry sectors, including oil and gas, electronics, aerospace, automotive and medical [1-3]. One of the major uses of PEEK in the medical sector is in the fabrication of spinal fusion cages [2, 3]. Spinal cages have been in clinical use since the

1990's and were first shown to be successful in the treatment of horses suffering from nerve root compression [2, 4].

PEEK is an attractive material for this role as it is lightweight, strong and well suited for high load-bearing application [5-7]. It exhibits a modulus of 3 GPa to 4 GPa which falls within the range of cancellous and cortical bone (0.05 GPa to 30 GPa) [2]. Metallic spinal cages, such as those fabricated from titanium alloy (Ti-6Al-4V), are considerably heavier and exhibit a higher modulus (approximately 110 GPa) compared with polymeric counterparts [8, 9]. This modulus mismatch with hard tissue can lead to stress shielding, where bone does not experience mechanical stimuli due to the high modulus material bearing a considerable fraction of the applied load. Additionally, titanium based cages are associated with a high occurrence of subsidence for both lumbar and cervical devices, hard tissue weakening and porosity development [10-12].

Improving the ability of PEEK to integrate with bone is recognised as essential for guaranteeing spinal fusion [10, 13, 14]. In a side-by-side study of stand-alone devices, 100 % of titanium cages facilitated fusion, whereas PEEK cages were only 76 % successful [10]. PEEK is both hydrophobic and chemically inert, limiting bone attachment and osseointegration compared to Ti-6Al-4V [13, 15].

Researchers have extensively developed and characterized PEEK surface porosity and bulk porosity, coatings, surface modifications, and composite formulations [14-25]. It appears that PEEK composite structures are beginning to play a more prominent role as commercially available

medical implants as alternatives to metallic materials such as Ti-6Al-4V and stainless steel [2, 17]. These materials typically contain bioactive calcium phosphate particulates, including hydroxyapatite (HA, $Ca_5(PO_4)_3(OH)_2$) and beta tricalcium phosphate (β-TCP, $Ca_3(PO_4)_2$), which have been shown to improve the osseointegration of PEEK with increasing loading level [14, 16-20, 25]. Invibio® currently manufacture a medical grade HA and PEEK material, PEEK-OPTIMA™ HA Enhanced, which has FDA approval for orthopaedic devices and recently acquired the European CE mark of approval [26]. PEEK-OPTIMA™ HA Enhanced devices out-perform PEEK-OPTIMA™ Natural devices (HA free) in terms of bone on growth and fusion, demonstrated in a sheep model [27].

Under loading, however, inclusions can act as stress initiators and risers that diminish the mechanical properties of these materials [28]. Moreover, dissimilarity between HA and PEEK leads to poor interfacial interactions between the phases, limiting the level of biologically beneficial inclusion. Failure can arise due to HA particulates becoming debonded from the polymeric matrix of PEEK [16, 20]. High inclusion levels of HA also increases the brittleness of composites as the ductile flow of the matrix is disrupted, decreasing the required energy to initiate fracture [19, 20, 29].

Up until now, approaches to improve additive interactions with polymeric matrices have focused on improving physical or physiochemical interlocking [16, 30, 31]. Chemical interactions may facilitate more effective load transfer between composite components, allowing higher loadings of bioceramic to be added whilst avoiding shortfalls in mechanical properties that

lead to catastrophic failure during load bearing. Benefits of covalently linking composites have been demonstrated between modified PEEK and carbon nanotube fillers [32, 33]. In this paper, a covalently linked HA and PEEK composite is engineered by functionalizing HA with (3-Mercaptopropyl) triethoxysilane (MPTES) and modifying PEEK by a reduction reaction, producing HA-SH and PEEK-OH respectively. p-Maleimidophenyl isocyanate (PMPI) is then used to link HA-SH to PEEK-OH to produce a covalently linked HA_L_PEEK additive, before processing composite materials in a PEEK matrix. Extensive characterization of bioceramic and polymer starting materials and their respective derivatives is provided, as well as physiochemical analysis of PEEK, HA_PEEK and HA_L_PEEK composites.

5.2 EXPERIMENTAL METHODS

5.2.1 Materials

Hydroxyapatite (20 μm agglomerations from SEM analysis, ≥97 %, synthetic), (3-Mercaptopropyl) triethoxysilane (MPTES) (≥ 95 %), Propan-2-ol (puriss, p.a., ACS reagent, ≥ 99.8 % (GC)), HCl (ACS reagent, 37 %), Potassium hydroxide (reagent grade, 90 %), Methanol (CHROMASOLV®, ≥ 99.9 %), p-Maleimidophenyl isocyanate (purum, ≥ 97 %) and Sodium borohydride (99.99 % trace metals basis) were acquired from Sigma Aldrich Ltd (U.K.). Ethanol (absolute, analytical reagent grade), dimethyl sulfoxide (DMSO) (analytical reagent grade) and Ellman's reagent (5,5'-Dithio-bis-(2-nitrobenzoic acid)) were acquired from Fisher Scientific (U.K.). Acheson Silver DAG was acquired from Agar Scientific (U.K.). VICTREX® PEEK 450PF (25

μm, easy fine flow) was acquired from Victrex plc (U.K.). Kapton® polyimide film was acquired from DuPont™(U.S.A). Loctite® Frekote® 44-NC mold release agent was acquired from Henkel (Germany). Distilled water acquired from an arium® advance EDI pure water system by Sartorius (Germany).

5.2.2 Synthesis and fabrication methods

5.2.2.1 Synthesis of HA-SH derivative

In order to yield a sufficient quantity of HA-SH, three identical synthesis reactions were undertaken simultaneously. Briefly, three vessels were individually filled with 200 mL 90/10 (vol %) propan-2-ol/water solution. 2 mL MPTES and 250 mg HA were added to each vessel under stirring (250 rpm) on a MR stirrer hotplate (Heidolph, Germany). At 40 minute intervals, a further 2 mL MPTES and 250 mg HA were added. Upon addition of MPTES and 250 mg HA, the reaction pH was adjusted to between 3 and 6, and after 20 minutes adjusted to between 9 and 11. This process was repeated totalling 7 40 minute cycles (4.67 h). pH profiles were manually tracked with a Mettler Toledo SevenCompact™ pH/ion meter equipped with InLab Expert Pro-ISM probe (Mettler Toledo, U.S.A). The resulting HA-SH products from each separate vessel were then combined and washed in 5 mL ethanol five times, and recovered by centrifugation with a CR4.22 centrifuge (Jouan SA, France) at 4000 rpm for 10 minutes. HA-SH was then dried at 60 ^{o}C for 30 minutes to ascertain full curing of MPTES to HA surfaces.

5.2.2.2 Synthesis of PEEK-OH derivative

5 g of PEEK 450PF was dispersed in 120 mL DMSO charged with 1.5 g $NaBH_4$ under inert argon (Ar) atmosphere. The suspension was heated to 120 °C and allowed to react for 24 hours, after which the contents was cooled to room temperature. PEEK-OH product was filtered and washed with excess ethanol, distilled water and 0.1 M HCl (diluted from concentrate), then dried at 80°C under vacuum.

5.2.2.3 Synthesis of HA_L_ PEEK

5 g HA-SH was dispersed in 10 mL DMSO charged with 50 mg of PMPI under constant agitation. After 15 min, 5 g of PEEK-OH was added to the reaction mixture, and the reaction allowed to proceed for a total of 3 h. The resulting product was then washed in methanol, water and methanol again.

5.2.2.4 Composite fabrication and acquisition of test specimens

PEEK, HA_PEEK and HA_L_PEEK powder batches were prepared at a total mass of 50 g. Regarding HA containing batches, the bioceramic content was 2.5 wt%, and the polymeric matrix was unmodified PEEK. Prior to processing, batches were kept at 140 ^{o}C overnight period in order to remove residual moisture. Plaques were fabricated in a Moore Hydraulic Press retrofitted with heating plates (JRD Bipel, U.K.) to attain temperatures of 400 ^{o}C. A spacer placed between the plates acted as a frame for the plaque, providing a 27.9 cm^3 volume. Powders were spread evenly within the press

volume and heated to 125 ^{o}C at minimal plate contact to remove air pockets. Contact pressure was then applied and the temperature increased to 400 ^{o}C. After 4 h, heating was turned off and the apparatus was allowed to cool to room temperature before retrieval of plaques with dimensions 180 x 150 x 1.2 mm.

5.2.3 Chemical and physical characterisation methods

5.2.3.1 Raman spectroscopy

Raman spectroscopy data were collected using an inVia Raman microscope (Renishaw, U.K.). The instrument was equipped with a 532 nm laser. Each spectrum was collected over 3 acquisitions between 100 cm^{-1} and 4100 cm^{-1} and the data normalised between sets.

5.2.3.2 Powder X-ray diffraction (XRD)

Powder XRD patterns were acquired using a Powder Diffractometer D8 Auto sampler (Bruker, U.S.A.) with Cu Kα line (0.154 nm). Pattern data was collected between 2θ values of 5 ^{o} and 60 ^{o} with a 0.02 ^{o} step-size and a step time of 0.5 s/^{o}. Patterns were matched to patterns within The International Centre for Diffraction Data (ICDD) database.

5.2.3.3 Thiol group (-SH) quantification

Quantification of thiol groups was undertaken using an Ellman's reagent (DTNB, 5,5'-Dithio-bis-(2-nitrobenzoic acid)) assay protocol [38]. Briefly, a buffer solution was prepared (distilled water, 100 mM Na_3PO_4 , 1

mM EDTA, pH 8). 0.05 mL of Ellman's solution (4 mg DTNB in 1 mL buffer solution) was added to 2.5 mL of buffer solution to produce a reaction solution. 5 mg of HA-SH was dispersed in a 0.25 mL of buffer solution and added to the reaction solution. The solution was kept agitated for 15 minutes to develop an assay solution. Upon reacting with free thiol groups, DTNB is converted to 2-nitro-5-thiobenzoic acid (TNB). TNB has a molar absorption coefficient of 14150 M^{-1} cm^{-1} at 412 nm. 1 mL of this solution was then transferred to a cuvette and the absorbance read at 412 nm with a Cecil CE7500 spectrophotometer (Buck Scientific, U.S.). The absorbance reading for unmodified HA sample was used as a control, and was automatically taken away from the reading acquired from the HA-SH samples. Equation S5.3-S5.5 were followed in order to determine the molar concentration of –SH groups present in the sample [38].

5.2.3.4 Differential scanning calorimetry (DSC)

DSC analysis was undertaken using a DSC 6000 N520-0116 instrument (Perkin Elmer, U.S.A). Approximately 10 mg of sample was held for two minutes at 20 ^{o}C for temperature stabilisation of the equipment. Samples were then heated to 400 ^{o}C at a ramp rate of 10 ^{o}C/min before cooling back down to 20 ^{o}C at the equivalent ramp rate.

5.2.3.5 Thermal gravimetric analysis (TGA)

TGA was carried out using a STA 449 F3 Jupiter instrument (Netzsch, Germany). Samples were heated to 700 ^{o}C at a ramp rate of 10 ^{o}C/min.

Further analysis was carried out directly on the data to calculate hydroxylation degree (HD) of the PEEK-OH derivative (Equation S5.6-S5.11).

5.2.3.6 Scanning electron microscopy (SEM)

For Figure 5.4a-c and S5.7a-c, specimens were placed upon double-sided sticky carbon discs that had been secured onto aluminum stubs. Specimens were then gold sputter coated using a K550X sputter coater (Quorum Technologies, U.K.). SEM images were then acquired using an EVO MA 10 scanning electron microscope operating at 10 kV (Carl Zeiss AG, Germany). For Figure 5.7d-f, specimen test pieces were placed in liquid nitrogen to allow for cryogenic fracture and exposure of a clean internal surface. Upon the underside of each specimen, a small amount of silver Acheson Silver DAG was applied in order to reduce charging. Double-sided sticky carbon discs and adhesive were used to secure specimens firmly to aluminum stubs. Specimens were then gold sputter coated using a Polaron SC7640 sputter coater (Quorum Technologies, U.K.). SEM images were then acquired using a 6060 scanning electron microscope operating at 10 kV (JOEL, U.S.A.).

5.2.3.7 Fourier transform infrared (FT-IR) spectroscopy

FT-IR spectra were collected using a Nicolet 380 FT-IR spectrometer (Thermo-Scientific, U.S.A.), fitted with a Golden Gate ATR attachment (Specac, U.K.). Measurements were collected between 100 cm^{-1} and 4100 cm^{-1} wavenumbers. A background scan was acquired before each scan and

subtracted in order to minimize the appearance of H_2O and CO_2 molecular modes contaminating each spectrum of interest.

5.2.3.8 Micro- X-ray fluorescence spectroscopy (μ-XRF)

Scans were performed in mapping mode on sections of PEEK composites materials with exposed areas of HA using a M4 Tornado instrument (Bruker, U.S.A.). Measurements settings of 20 ms/pixel were employed with the instrument operating at 50 kV with anode current of 300 mA. The chamber was maintained at 20 mbar during measurements.

5.2.3.9 Flexural 3-point bend testing

A schematic of the mechanical testing set-up is provided (Figure S5.1). Specimens of 60 x 12 x 1.2 mm were cut out from plaques with a band saw. The span to depth ratio was calculated as outlined in ASTM D790/ISO 178 to ensure specimens failed through compression stress whilst minimising shear stress. Tests were performed on a 5566 testing rig (Instron, U.K.) at a crosshead speed of 1 mm/min. Flexural strength and flexural modulus were calculated using Equations S5.1-S5.2 included in Appendix Part 4.

5.2.4 Statistical analysis

One-way ANOVA and corresponding Holm-Sidak post-hoc tests were performed upon mechanical testing data. Values of $p<0.05$ were deemed statistically significant.

5.3 RESULTS AND DISCUSSION

5.3.1 Synthesis of HA-SH

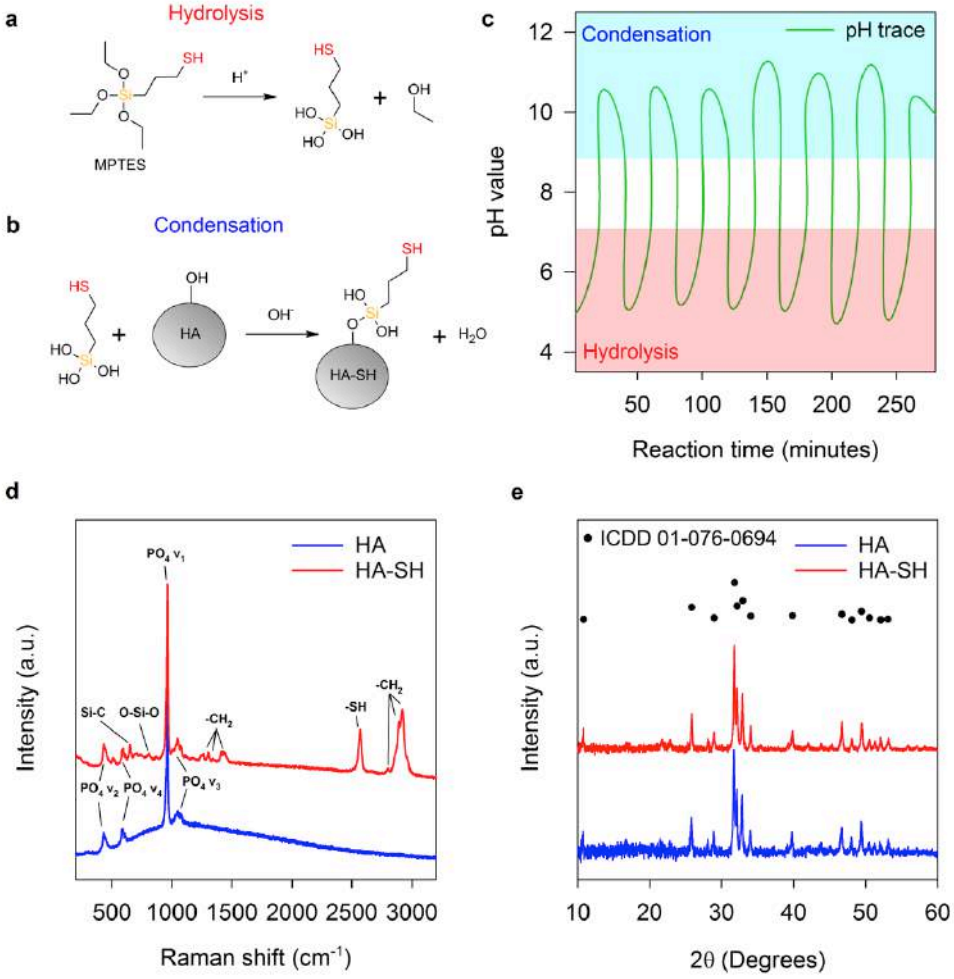

Figure 5.1 (a) Hydrolysis and **(b)** condensation reactions of MPTES. **(c)** pH profile of the reaction between HA and MPTES to produce HA-SH. **(d)** Raman spectra and **(e)** XRD patterns of as received HA and following the synthesis of HA-SH.

MPTES attaches to substrates through hydrolysis and subsequent condensation reactions (Figure 5.1a, b). Adjustment of pH over several hours promoted favorable thermodynamic environments for both reactions (Figure 5.1c) [34]. Acidic regions between pH values of 3 and 7 were used to promote

hydrolysis of siloxy groups (R-Si-$(OCH_3)_3$) to silanol groups (R-Si-$(OH)_3$), and adjustment of the pH to above 9 promoted condensation upon HA.

Vibrations of the tetrahedral HA PO_4 anion, including symmetric stretching (PO_4 v_1), symmetric bending (PO_4 v_2), asymmetric stretching (PO_4 v_3) and asymmetric bending (PO_4 v_4), are identified by peaks present at 435 cm^{-1}, 590 cm^{-1}, 960 cm^{-1} and 1050 cm^{-1} respectively (Figure 5.1d). Carbonate substitution of the HA crystal lattice is suggested by peaks at approximately 1070 cm^{-1} (CO_2 v_1).

Peaks relating to MPTES upon HA are present in the HA-SH spectrum, evidencing silane attachment [35-39]. A Si-C stretching peak appears at 652 cm^{-1}. A peak at 864 cm^{-1} is present due to CH_2 rocking. Peaks at 1262 cm^{-1}, 1301 cm^{-1}, 1342 cm^{-1} and 1431 cm^{-1} are indicative of $–CH_2$ twisting modes. Overlapping peaks at 2804 cm^{-1}, 2891 cm^{-1} and 2918 cm^{-1} are due to $–CH_2$ vibrations. The –SH stretching peak at 2569 cm^{-1} confirms HA-SH thiol groups [38]. A Si-O-Si stretching peak located at 809 cm^{-1} indicates silane oligmerisation, suggesting a network of MPTES molecules bound to HA-SH.

Subtle broadening of PO_4 v_{1-4} peaks in the spectrum HA-SH indicates alterations of P-O bonding environments. Broader peaks indicate structural disorder, whilst sharper peaks arise from ordered environments [40]. Differences could be due to the dynamic reaction experienced by HA during modification with MPTES, which may be capable of promoting dissolution and re-precipitation of alternative calcium phosphate phases, as well as the bonding of MPTES to HA-SH.

XRD confirmed HA remained the sole crystalline phase following modification with MPTES (Figure 5.1e). HA and HA-SH were successfully matched to ICDD pattern number 01-076-0694 (synthetic HA, * quality, with formula $Ca_5(PO_4)_3OH$). Additionally, crystalline regions of HA were minimally disrupted by the reaction with MPTES, as there was a non-substantial decrease in crystallinity from 77.0 % to 76.6 % as determined by analysis of XRD patterns, further evidencing that the widening of PO_4 peaks in the Raman spectrum of HA-SH is likely due to grafting of MPTES to HA rather than a reduction or change in crystallinity.

Quantification of thiol groups associated with the surface of HA-SH was approximated at $5.9 \times 10^{-6} \pm 8.2 \times 10^{-8}$ mol g^{-1} calculated using equations S5.3-S5.5.

5.3.2 Synthesis of PEEK-OH

PEEK was converted to PEEK-OH by reduction (Figure 5.2a) [41, 42]. Crystal structures of PEEK and PEEK-OH were assessed by powder XRD (Figure 5.2b). Peaks of both patterns were located at 2θ values of 19 °, 21 °, 23 ° and 29 °, representative of orthorhombic unit cell PEEK crystal planes of 110, 111, 200 and 211 respectively, suggesting that the lattice parameters are preserved during hydroxylation [41]. Conversion of PEEK to PEEK-OH reduced crystallinity from 46.1 % to 38.4 %.

The melting temperature (T_M) of PEEK was found to be 347.8 ^oC, which was approximately 4 ^oC greater than the T_M possessed by PEEK-OH of 343.7 ^oC (Figure 5.2c). On cooling, PEEK-OH appears to undergo minimal

crystallization, possessing no clear peak to define crystallization temperature (T_C), whilst PEEK possesses a T_C of 306.47 °C. This indicates that PEEK-OH becomes fully amorphous due to thermal treatment. When PEEK undergoes reduction chirality is introduced, which may increase the amorphous nature of PEEK-OH compared to PEEK (Figure S5.2). The -OH moiety introduced along the polymer chain may also inhibit crystallization by creating irregularity in forming crystalline regions. Moreover, hydrogen bonding mediated by -OH groups may be extensive enough to suppress polymer chain mobility required for crystallization [41].

PEEK undergoes a one step degradation beginning at approximately 550 ^{o}C (Figure 5.2d). The steep drop off in mass with temperature is indicative of main chain degradation [43]. PEEK-OH undergoes an initial mass loss between 100 ^{o}C and 250 ^{o}C that is attributed to the loss of weakly bound H_2O molecules. Loss between 250 °C and 400 °C was used to calculate the hydroxylation degree (HD) of PEEK-OH of 37.6 %, consistent with previous work (Figure S5.3)(Equations S5.6-S5.11). Main chain degradation begins at approximately 500 °C, suggesting a lower thermal stability of PEEK-OH compared to PEEK. Promisingly, the polymer derivative remains intact with respect to processing temperatures for PEEK between 380 ^{o}C and 400 ^{o}C.

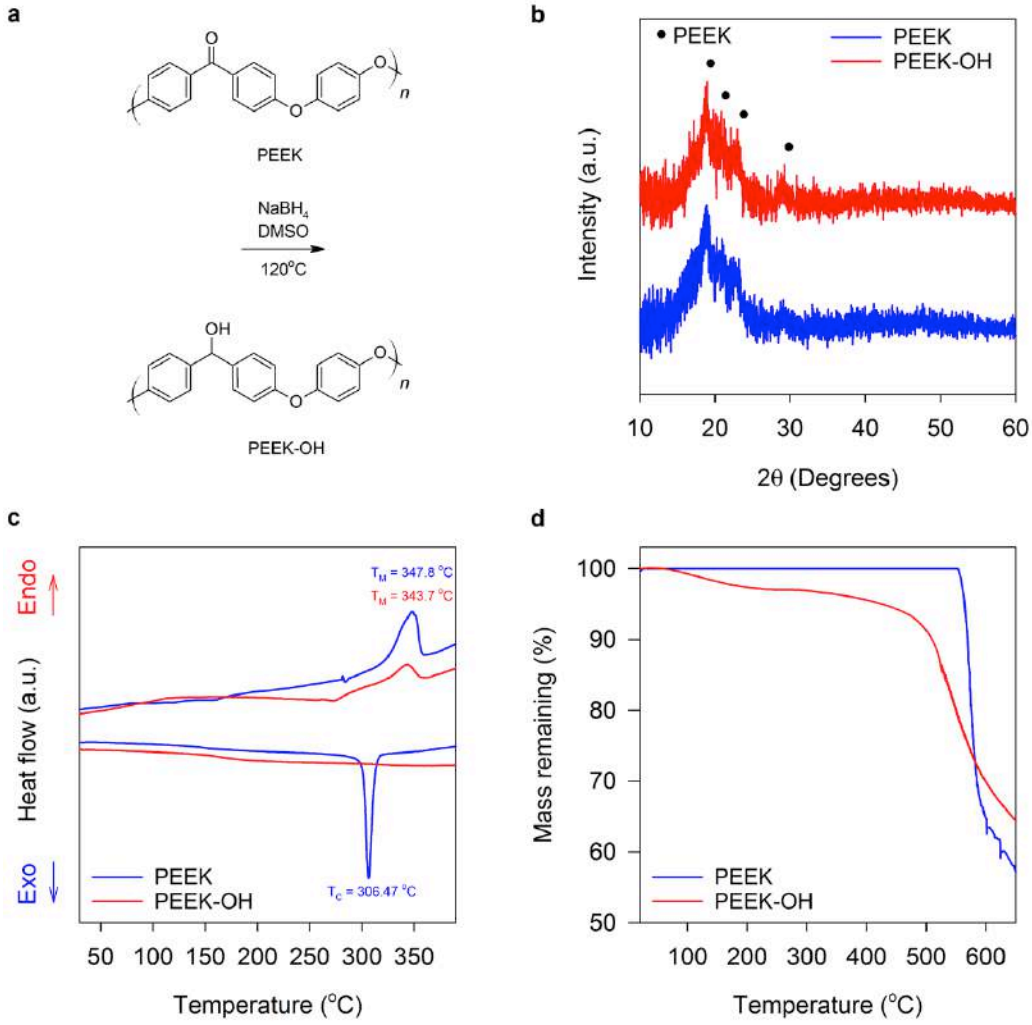

Figure 5.2 (a) Reduction reaction of PEEK to PEEK-OH. **(b)** XRD patterns, **(c)** DSC traces and **(d)** TGA traces of as received PEEK and following reduction to PEEK-OH.

5.3.3 Synthesis of chemically linked HA_L_PEEK

PMPI possesses maleimide and isocyanate termini. HA-SH thiol groups react with maleimide to produce a thioether bond (C-S-C) (Figure 5.3a). Hydroxyls of PEEK-OH react with isocyanate to produce a carbamate bond (R-O-C(=O)-NH-R) (Figure 5.3b).

Newly formed chemical bonds were assessed by FT-IR spectroscopy (Figure 5.3c). PO_4 modes associated with the structure of HA-SH are located at 470 cm^{-1}, 608 cm^{-1}, 962 cm^{-1} (as a shoulder), and 1033 cm^{-1}. Peaks associated with C-H stretching that originate from MPTES on the HA-SH surface are observed at 2920 cm^{-1} [38, 39]. FT-IR confirms formation of C-S-C bonds with PMPI by the symmetric and asymmetric peaks of which are detected at 677 cm^{-1} and 771 cm^{-1} [44]. The –SH stretching peak at 2546 cm^{-1} suggests a portion of thiol groups remain unreacted [38].

PEEK-OH peaks include out of plane aromatic hydrogen (O.A.H.) modes at 840 cm^{-1} and 860 cm^{-1}, a diphenyl ketone band at 927 cm^{-1}, asymmetric C-O-C bending at 1182 cm^{-1} and 1278 cm^{-1}, C-C(=O)-C bending at 1307 cm^{-1}, aromatic skeletal vibrations (A.S.V.) at 1412 cm^{-1} and 1493 cm^{-1}, and C=O stretching at 1650 cm^{-1}. Identification of carbamate bonds was made, but was difficult due to peak overlapping [45-47]. Carbamate COO^- and C=O stretching modes expected at 1600 cm^{-1} and 1650 cm^{-1} are overlapped by peaks relating to C=C and C=O stretching from PEEK-OH. Peaks for C-N stretching are found at 1220 cm^{-1} and 1703 cm^{-1}. N-H stretching peaks are located at 1550 cm^{-1} and 3370 cm^{-1}. Peaks at 1495 cm^{-1} and 2194 cm^{-1} are evidence of NH_3^+ modes. Unreacted N=C=O groups are identified by the peak at 2341 cm^{-1}. Minimal evidence of –OH stretching bands in the region between 3200 cm^{-1} and 3550 cm^{-1} also indicates the formation of carbamate bonds, as hydroxyls are used up during formation.

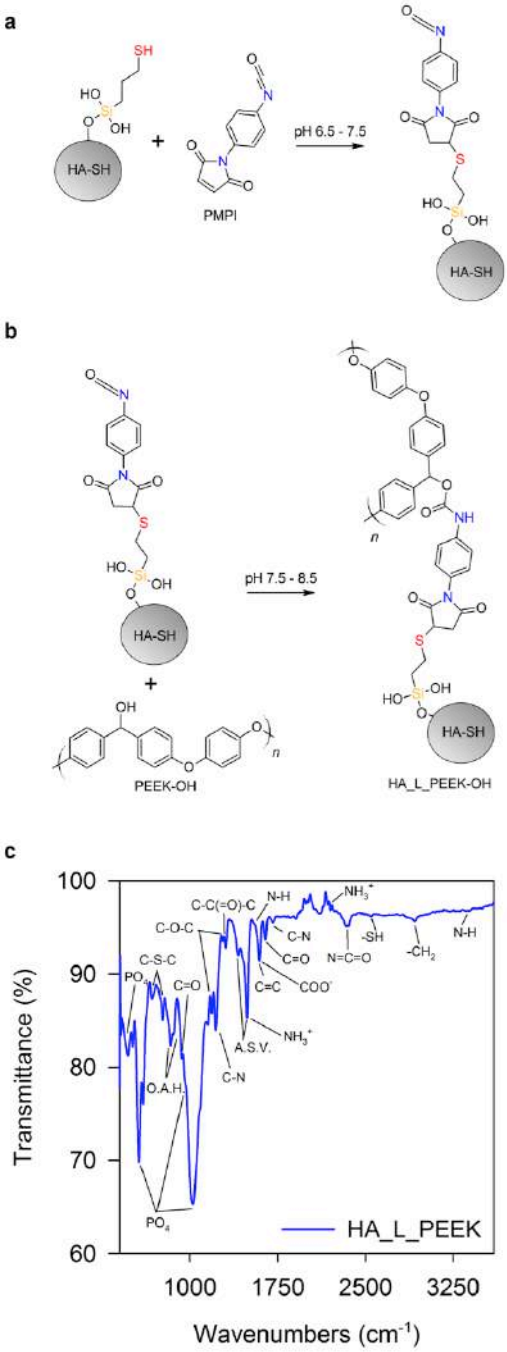

Figure 5.3 (a) Reaction between HA-SH and PMPI chemical linker and **(b)** between PEEK-OH and PMPI. **(c)** FT-IR spectrum for HA_L_PEEK.

SEM micrographs further evidenced the success of the linking procedure. Figure 5.4a shows that HA-SH particulates are in the approximate size range of between 25 μm and 50 μm in diameter and furthermore possess

textured surfaces and sharp interfaces. Particles of PEEK-OH were between 10 μm and 30 μm in diameter, and possessed smooth surfaces (Figure 5.4b). HA-SH and PEEK-OH powder particulates do not appear to interact strongly when mixed (Figure 5.4c). Mixing alone therefore does not appear to facilitate interactions between the dissimilar phases. After chemical linking with PMPI however, the resulting HA_L_PEEK appears to consist of agglomerates of both powders (Figure 5.4d).

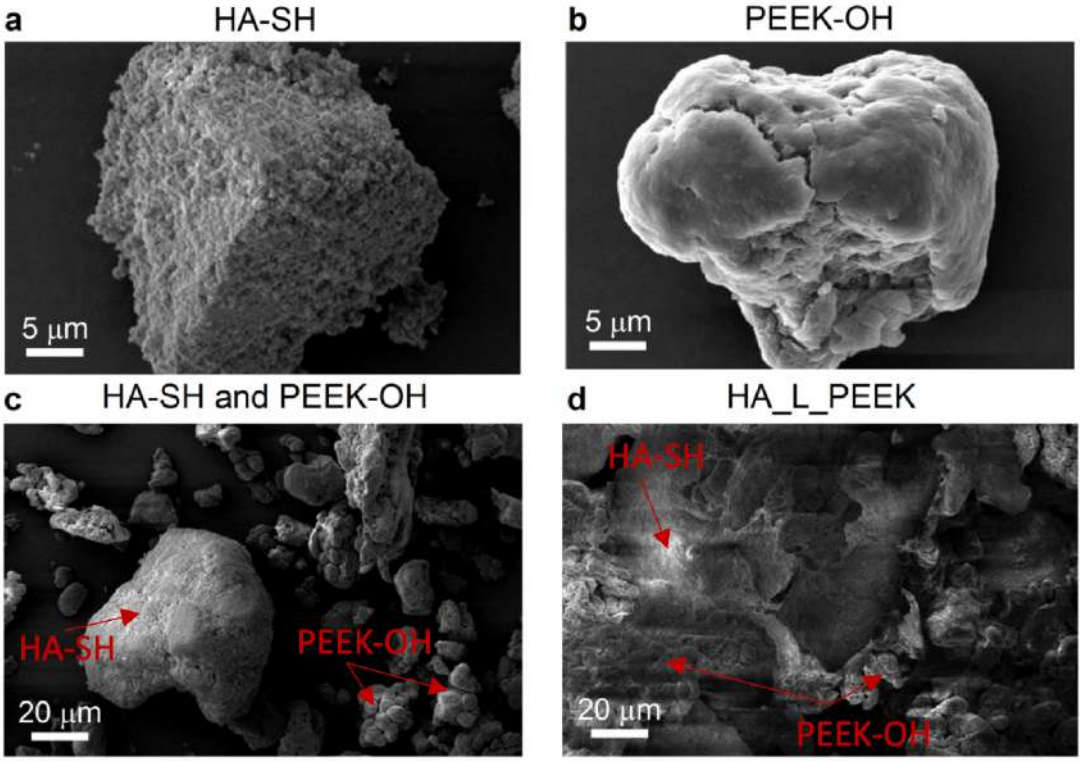

Figure 5.4 SEM micrographs of **(a)** HA-SH, **(b)** PEEK-OH, **(c)** a mixture of HA-SH and PEEK-OH particulates, and **(d)** chemically linked HA-SH and PEEK-OH (additive material for HA_L_PEEK composites).

Larger HA-SH particles appear to act as a substrate for bonding interactions with PEEK-OH particles, made possible through the chemical linking procedure. This is also consistent with our experimental method,

whereby the maleimide groups of PMPI firstly react with the –SH groups of HA-SH, allowing the then presented isocyanate groups of the linker to react with the –OH groups of PEEK-OH following its addition to the reaction mixture.

5.3.4 Composite characterisation

Mechanical properties of the composites were determined from 3-point bend testing (Figure 5.5a and Figure S5.1). PEEK specimens underwent ductile failure without fracture, and demonstrated plastic deformation at extension beyond the elastic region (Figure 5.5b). PEEK specimens remained whole after testing. Both HA_PEEK (without chemical linking) and HA_L_PEEK (with chemical linking) specimens containing 2.5 wt% HA underwent brittle failure immediately following elastic deformation, resulting in fracture (Figure 5.5b).

PEEK exhibited a flexural strength of 201.2±8.3 MPa, which was significantly greater that the flexural strength of HA_PEEK and HA_L_PEEK being 170.7±5.4 MPa ($p<0.001$) and 171.7±14.8 MPa ($p<0.001$) respectively (Figure 5.5c). Although covalent bonding slightly enhanced the flexural strength of HA_L_PEEK, it was not found to be significant ($p = 0.851$), presumably due to variation of results expected from brittle failure. The flexural modulus of PEEK was 5.3±0.3 GPa (Figure 5.5d). Interestingly, there was no statistical difference between PEEK and HA_L_PEEK materials in terms of flexural modulus, the former possessing a value of 5.0±0.3 GPa ($p=0.127$). However, the flexural modulus of HA_PEEK was significantly lower

in comparision to PEEK (p = 0.026). Therefore, HA_L_PEEK substantially improved upon HA_PEEK in terms of flexural modulus.

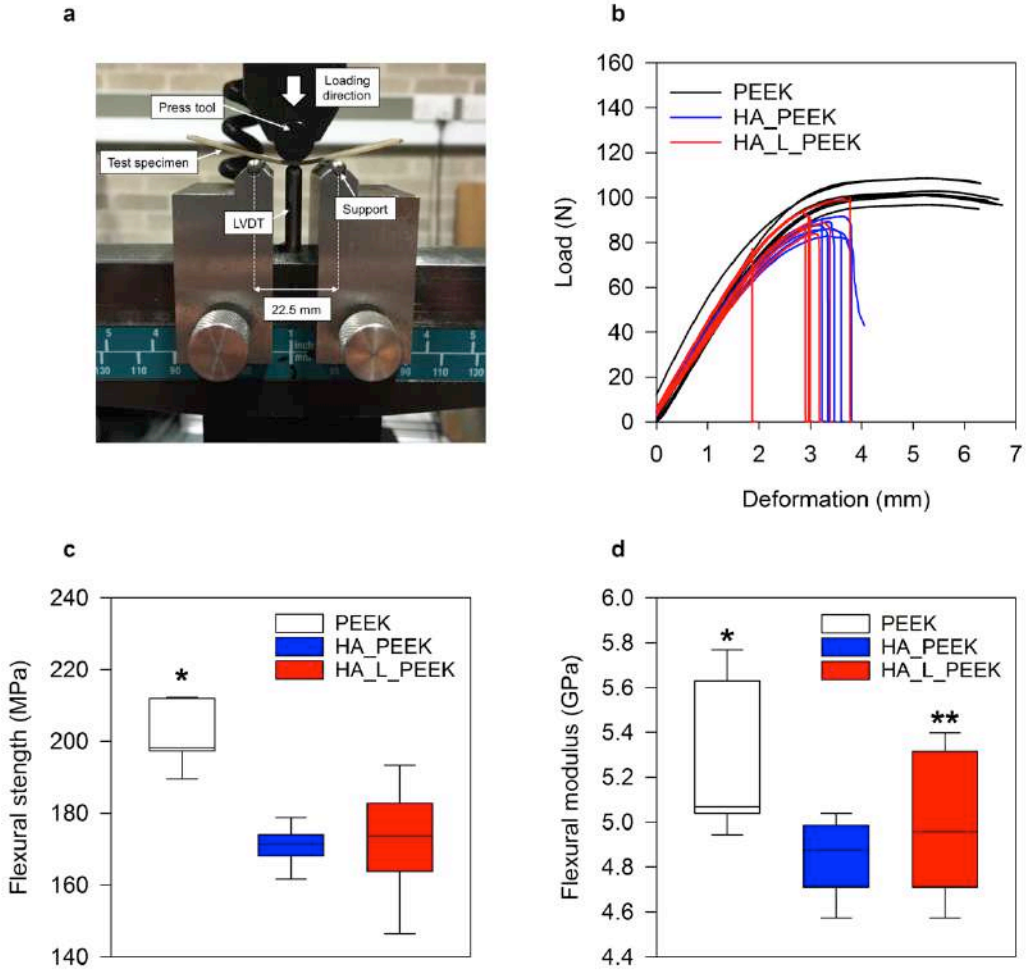

Figure 5.5 (a) 3-point bend test set-up (LVDT = Linear Variable Displacement Transducer). **(b)** Load displacement curves for PEEK, HA_PEEK and HA_L_PEEK materials. **(c)** Flexural strength box-plots for all groups calculated from the load displacement curves in **(b)** (n = 7) (* = $p < 0.05$ for PEEK vs. HA_PEEK and for PEEK vs. HA_L_PEEK). **(d)** Flexural modulus box-plot for all groups calculated from the load displacement curves in **(b)** (n = 7) (* = $p < 0.05$ for PEEK vs. HA_PEEK, ** = $p > 0.05$ for PEEK vs. HA_L_PEEK).

5.3.5 Mechanism of composite enhancement by covalent bonding

Chemical linking remained intact following composite fabrication, as confirmed by elemental mapping μ-XRF spectroscopy and DSC analysis, the latter described in Appendix Part 4 (Figure 5.6 and S5.4). Analysis of the chemical linking chemistry after fabrication was undertaken by comparing elemental maps of HA inclusions within HA_PEEK and HA_L_PEEK composites acquired using a μ-XRF instrument. The main elemental constituents of the HA inclusions were expectedly calcium (Ca) and phosphorous (P) as indicated by Kα signals at 3.7 KeV and 2.0 KeV respectively (Figure 5.6a,b). Elemental silicon (Si) was also detected in HA_L_PEEK by a peak at 1.75 keV, but was absent in HA_PEEK (Figure 5.6c). The silicon signal originates from the presence of the MPTES molecules grafted to HA as part of chemical linking formulation. Mapping of the Ca Kα and P Kα signals show that elemental Ca and P are localised to the HA particulates in both composites (Figure 5.6d).

During processing, high temperatures and mobile PEEK chains during melt are most likely to disrupt and distribute components of the linking chemistry throughout the wider polymeric matrix. Given that the Si content of HA_L_ PEEK appears to remain localised to HA particulates (Figure 5.6e), it can be taken as evidence that the chemical linking chemistry remains intact during the processing of composites to provide enhanced interactions between HA and PEEK.

The linking chemistry present in HA_L_PEEK may facilitate the observed improvement in both flexural strength and flexural modulus

compared to HA_PEEK through the provision of enhanced interfacial interactions between HA and PEEK components that is greater than mechanical interlocking alone.

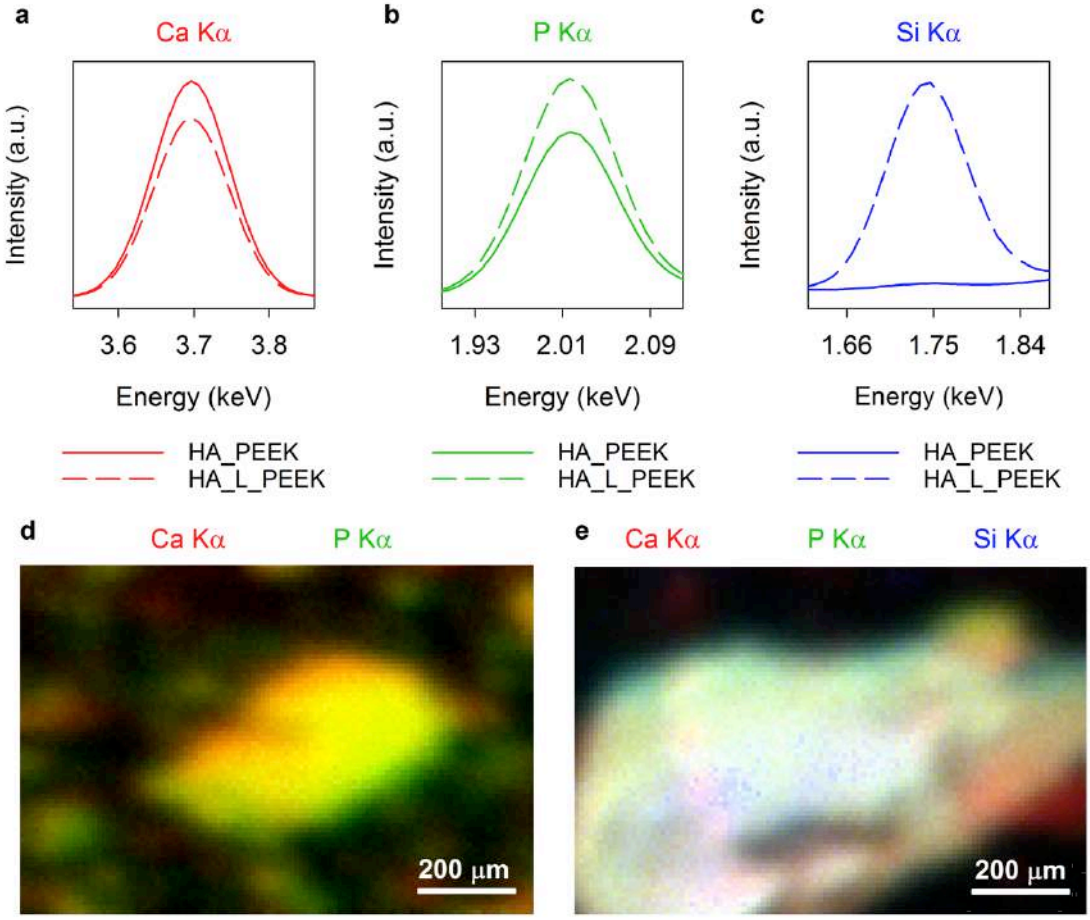

Fig 5.6 *μ*-XRF elemental mapping of HA particulates within HA_PEEK and HA_L_PEEK materials following composite fabrication. **(a)** *μ*-XRF spectrum central to the Ca Kα signal. **(b)** *μ*-XRF spectrum central to the P Kα signal. **(c)** *μ*-XRF spectrum central to the Si Kα signal. **(d)** Elemental map for a fracture surface of HA_L_PEEK with Ca and P Kα channels shown. **(e)** Elemental map for a fracture surface of HA_L_PEEK with Ca, P and Si Kα channels shown.

It is likely that this acts through two mechanisms as evidenced by SEM analysis of intact and fracture surfaces of HA_PEEK and HA_L_PEEK. Firstly, the established chemical interactions appear to lessen the development of HA debonding and micro-cracks (Figure 5.7a-c). Pre-existing microcracks can promote crack initiation, leading to premature failure of materials under load [48]. HA inclusions within HA_PEEK surfaces appear to promote micro cracks spanning 10's of microns (Figure 5.7 a, b). HA on the surface of HA_L_PEEK was not associated with debonding from PEEK or crack development prior to mechanical testing (Figure 5.7c).

Secondly, mechanical failure of these composites is partly dependent on flaws present within the brittle HA component, as well as HA particulates themselves. HA is a relatively stiff ceramic and can provide the resulting composite with an enhanced modulus [20, 49]. However, gains are dependent on loading level and the nature of the filler particulates [28, 49]. Lower levels of loading are generally favoured using both micro- and nano- scale particulates, as filler agglomeration that occurs at high loading levels reduces mechanical properties [25, 28, 49, 50]. This is because as particulate inclusions become smaller, they are less liable to contain flaws or act as flaws [48, 49, 51, 52]. Griffith's law states that the stress concentration at the tip of a defect depends on the defects size [51, 52]. Thus, the combined stress concentration will be greater for and within larger HA particulates.

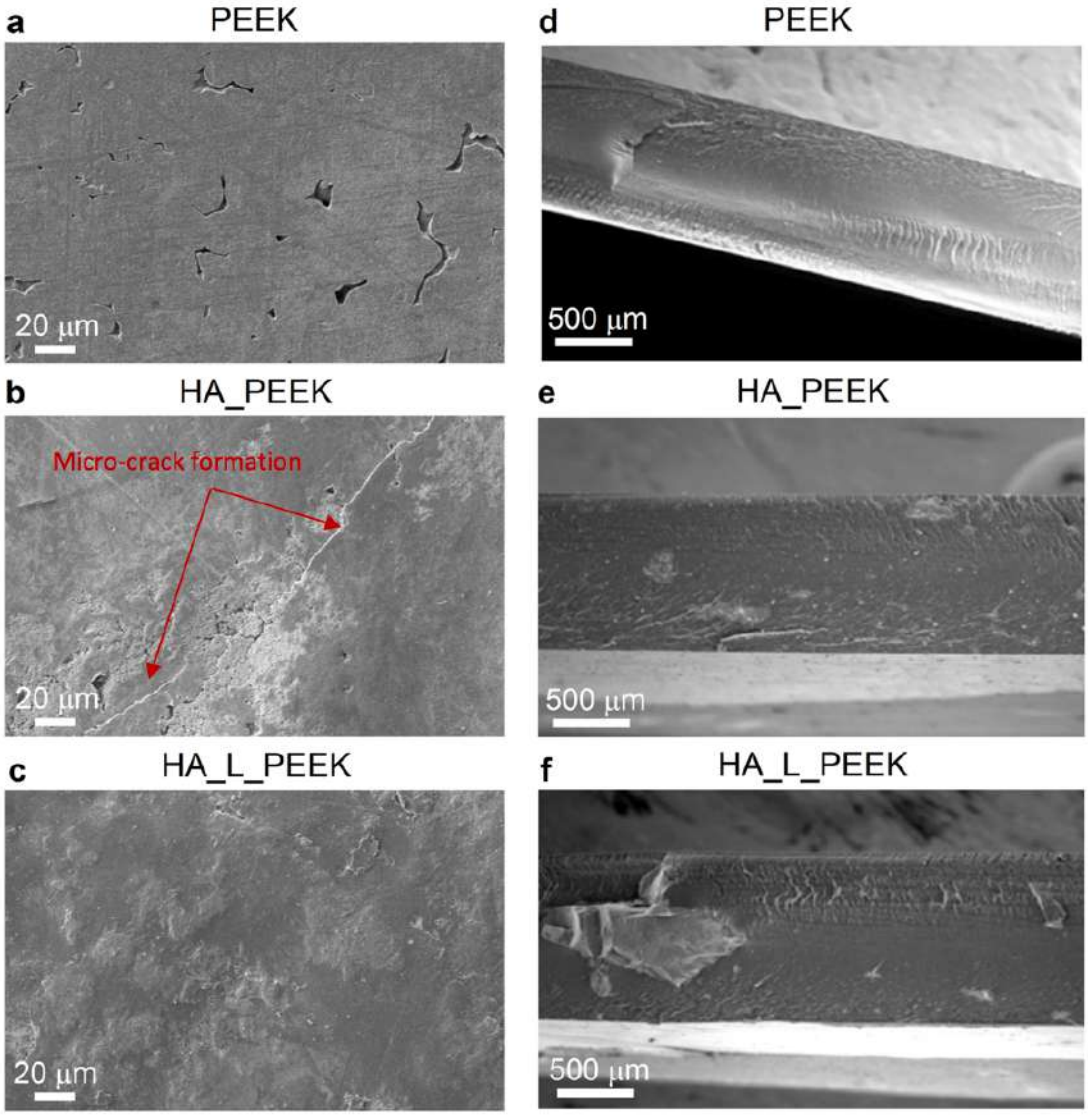

Figure 5.7 As fabricated surface of **(a)** PEEK, **(b)** HA_PEEK and **(c)** HA_L_PEEK. Fracture surface of **(d)** PEEK, **(e)** HA_PEEK and **(f)** HA_L_PEEK.

Particle shape and size distribution of covalently linked HA and PEEK is difficult to control due to the additive itself existing as an agglomeration of bioceramic and polymeric materials. The effect is exacerbated in the case of HA_L_PEEK composites (Figure 5.7d-f). Therefore, the particle size range of HA within HA_PEEK is between 60 μm to 220 μm, and between 125 μm to

1000 μm within HA_L_PEEK, as measured by SEM analysis. Evidently, covalent bonding maintains the mechanical properties of composite possessing larger inclusions, considering that there is no significant difference in flexural modulus between PEEK and HA_L_PEEK materials, whilst the properties of HA_PEEK are significantly lessened. Covalent interactions appear to improve load transfer between HA and PEEK phases by arresting crack growth and propagation at the interface, benefiting the ability of HA_L_PEEK to resist failure under load by increasing fracture energy [19, 20, 29]. Mechanical locking interactions present in HA_PEEK likely promotes brittle failure at lower force loadings due to the high stiffness possessed by HA not as effectively being transferred to the surrounding polymeric matrix, reducing regions of ductile flow about bioceramic irregularities [19, 20, 29].

Further work will look to reduce inclusion particle size, lessen agglomeration, increase the range of HA loadings and assess *in vitro* cytotoxicity. Utilising nano HA particulates will increase interaction surface area, and make it easier to attain homogeneous distribution, allowing higher loadings of HA to be included for the enhancement of integration with bone.

5.4 CONCLUSIONS

The formulation of a covalently linked HA and PEEK composite was demonstrated. Covalent interactions significantly improve the flexural modulus of HA_L_PEEK over HA_PEEK at 2.5 wt% HA loading, despite the former possessing larger HA inclusions due to agglomeration effects. Chemical linking contributes to the flexural modulus gains by reducing HA particle

debonding, arresting the development of micro cracks, and facilitating enhanced load transfer between phases.

Improvements to covalently linked composites may allow for the development of spinal fusion devices that potentially out perform metallic alternatives (i.e. Ti-6Al-4V) and plain PEEK in terms of fusion capacity, whilst avoiding additive debonding and diminishment of mechanical properties that currently hamper HA and PEEK composites. However, this will be challenging considering the good fusion capacity of titanium implants.

5.5 ASSOCIATED CONTENT

Supporting figures and equations are included in Appendix Part 4.

5.6 REFERENCES

1. Shukla D, Negi YS, Uppadhyaya JS, Kumar V. Synthesis and Modification of Poly(ether ether ketone) and their Properties: A Review. Polymer Reviews. 2012;52(2):189-228.

2. Kurtz SM, Devine JN. PEEK Biomaterials In Trauma, Orthopedic, And Spinal Implants. Biomaterials. 2007;28(32):4845-69.

3. Kurtz SM. Chapter 1 - An Overview of PEEK Biomaterials. In: Kurtz SM, editor. PEEK Biomaterials Handbook. Oxford: William Andrew Publishing; 2012. p. 1-7.

4. Bagby GW. Arthrodesis by the distraction-compression method using stainless steel implant. Orthopedics 1988;11(6):931-4.

5. Ferguson S, Visser JA, Polikeit A. The long-term mechanical integrity of non-reinforced PEEK-OPTIMA polymer for demanding spinal applications: experimental and finite-element analysis. Eur Spine J. 2006;15(2):149-56.

6. Mastronardi L, Ducati A, Ferrante L. Anterior cervical fusion with polyetheretherketone (PEEK) cages in the treatment of degenerative disc disease. Preliminary observations in 36 consecutive cases with a minimum 12-month follow-up. Acta neurochirurgica. 2006;148(3):307-12; discussion 12.

7. Ni J, Zheng Y, Liu N, Wang X, Fang X, Phukan R, et al. Radiological evaluation of anterior lumbar fusion using PEEK cages with adjacent vertebral autograft in spinal deformity long fusion surgeries. Eur Spine J. 2015;24(4):791-9.

8. Wu SH, Li Y, Zhang YQ, Li XK, Yuan CF, Hao YL, et al. Porous titanium-6 aluminum-4 vanadium cage has better osseointegration and less micromotion than a poly-ether-ether-ketone cage in sheep vertebral fusion. Artificial organs. 2013;37(12):E191-201.

9. Herrera A, Yanez A, Martel O, Afonso H, Monopoli D. Computational study and experimental validation of porous structures fabricated by electron beam melting: A challenge to avoid stress shielding. Materials science & engineering C, Materials for biological applications. 2014;45:89-93.

10. Cabraja M, Oezdemir S, Koeppen D, Kroppenstedt S. Anterior cervical discectomy and fusion: Comparison of titanium and polyetheretherketone cages. BMC Musculoskeletal Disorders. 2012;13(1):172.

11. Chen Y, Wang X, Lu X, Yang L, Yang H, Yuan W, et al. Comparison of titanium and polyetheretherketone (PEEK) cages in the surgical treatment of

multilevel cervical spondylotic myelopathy: a prospective, randomized, control study with over 7-year follow-up. Eur Spine J. 2013;22(7):1539-46.

12. Nemoto O, Asazuma T, Yato Y, Imabayashi H, Yasuoka H, Fujikawa A. Comparison of fusion rates following transforaminal lumbar interbody fusion using polyetheretherketone cages or titanium cages with transpedicular instrumentation. Eur Spine J. 2014;23(10):2150-5.

13. Almasi D, Iqbal N, Sadeghi M, Sudin I, Abdul Kadir MR, Kamarul T. Preparation Methods for Improving PEEK's Bioactivity for Orthopedic and Dental Application: A Review. International journal of biomaterials. 2016;2016:8202653.

14. Zhao M, Li H, Liu X, Wei J, Ji J, Yang S, et al. Response of Human Osteoblast to n-HA/PEEK--Quantitative Proteomic Study of Bio-effects of Nano-Hydroxyapatite Composite. Sci Rep. 2016;6:22832.

15. Evans NT, Torstrick FB, Lee CS, Dupont KM, Safranski DL, Chang WA, et al. High-strength, surface-porous polyether-ether-ketone for load-bearing orthopedic implants. Acta biomaterialia. 2015;13:159-67.

16. Ma R, Weng L, Bao X, Song S, Zhang Y. In Vivo Biocompatibility and Bioactivity of In Situ Synthesized Hydroxyapatite/Polyetheretherketone Composite Materials. 2013;127(4):2581-7.

17. Ma R, Tang T. Current strategies to improve the bioactivity of PEEK. Int J Mol Sci. 2014;15(4):5426-45.

18. Green S. Chapter 3 - Compounds and Composite Materials. In: Kurtz SM, editor. PEEK Biomaterials Handbook. Oxford: William Andrew Publishing; 2012. p. 23-48.

19. Wang L, Weng L, Song S, Sun Q. Mechanical properties and microstructure of polyetheretherketone–hydroxyapatite nanocomposite materials. Materials Letters. 2010;64(20):2201-4.

20. Abu Bakar MS, Cheng MHW, Tang SM, Yu SC, Liao K, Tan CT, et al. Tensile properties, tension–tension fatigue and biological response of polyetheretherketone–hydroxyapatite composites for load-bearing orthopedic implants. Biomaterials. 2003;24(13):2245-50.

21. Lee JH, Jang HL, Lee KM, Baek HR, Jin K, Hong KS, et al. In vitro and in vivo evaluation of the bioactivity of hydroxyapatite-coated polyetheretherketone biocomposites created by cold spray technology. Acta biomaterialia. 2013;9(4):6177-87.

22. Barkarmo S, Andersson M, Currie F, Kjellin P, Jimbo R, Johansson CB, et al. Enhanced bone healing around nanohydroxyapatite-coated polyetheretherketone implants: An experimental study in rabbit bone. Journal of Biomaterials Applications. 2014;29(5):737-47.

23. Johansson P, Jimbo R, Kozai Y, Sakurai T, Kjellin P, Currie F, et al. Nanosized Hydroxyapatite Coating on PEEK Implants Enhances Early Bone Formation: A Histological and Three-Dimensional Investigation in Rabbit Bone. Materials. 2015;8(7):3815-30.

24. Landy BC, VanGordon SB, McFetridge PS, Sikavitsas VI, Jarman-Smith M. Mechanical and in vitro investigation of a porous PEEK foam for medical device implants. J Appl Biomater Funct Mater 2013;11(1):35-44.

25. Wang L, Weng L, Song S, Zhang Z, Tian S, Ma R. Characterization of polyetheretherketone–hydroxyapatite nanocomposite materials. Materials Science and Engineering: A. 2011;528(10-11):3689-96.

26. Invibio Biomaterial Solutions Announces Global Launch of “PEEK-OPTIMA HA Enhanced Polymer” - A new PEEK-based biomaterial designed for superior bone apposition. [press release]. Online, 19/04/2017 2013.

27. Walsh WR, Pelletier MH, Bertollo N, Christou C, Tan C. Does PEEK/HA Enhance Bone Formation Compared With PEEK in a Sheep Cervical Fusion Model? Clin Orthop Relat Res. 2016;474(11):2364-72.

28. Michler GH, von Schmeling H-HK-B. The physics and micro-mechanics of nano-voids and nano-particles in polymer combinations. Polymer. 2013;54(13):3131-44.

29. Kuo MC, Tsai CM, Huang JC, Chen M. PEEK composites reinforced by nano-sized SiO2 and Al2O3 particulates. Materials Chemistry and Physics. 2005;90(1):185-95.

30. Sousa RA, Reis RL, Cunha AM, Bevis MJ. Coupling of HDPE/hydroxyapatite composites by silane-based methodologies. Materials in medicine. 2003;14:475-87.

31. Ma R, Li Q, Wang L, Zhang X, Fang L, Luo Z, et al. Mechanical properties and in vivo study of modified-hydroxyapatite/polyetheretherketone biocomposites. Materials science & engineering C, Materials for biological applications. 2017;73:429-39.

32. Díez-Pascual AM, Martínez G, Martínez MT, Gómez MA. Novel nanocomposites reinforced with hydroxylated poly(ether ether ketone)-grafted carbon nanotubes. Journal of Materials Chemistry. 2010;20(38):8247.

33. Díez-Pascual AM, Martínez G, González-Domínguez JM, Ansón A, Martínez MT, Gómez MA. Grafting of a hydroxylated poly(ether ether ketone) to the surface of single-walled carbon nanotubes. Journal of Materials Chemistry. 2010;20(38):8285.

34. Savard S, Blanchard LP, Léonard J, Prud'homme RE. Hydrolysis and condensation of silanes in aqueous solutions. Polymer Composites. 1984;5(4):242-9.

35. Wang S, Wen S, Shen M, Guo R, Cao X, Wang J, et al. Aminopropyltriethoxysilane-mediated surface functionalization of hydroxyapatite nanoparticles: synthesis, characterization, and in vitro toxicity assay. International journal of nanomedicine. 2011;6:3449-59.

36. de Campos RP, Yoshida IV, Breitkreitz MC, Poppi RJ, Fracassi da Silva JA. Raman imaging spectroscopic characterization of modified poly(dimethylsiloxane) for micro total analysis systems applications. Spectrochim Acta A Mol Biomol Spectrosc. 2013;100:67-71.

37. Schmitt M. Analysis of silanes and of siloxanes formation by Raman spectroscopy. RSC Advances. 2014;4(4):1907-17.

38. Williams RL, Hadley MJ, Jiang PJ, Rowson NA, Mendes PM, Rappoport JZ, et al. Thiol modification of silicon-substituted hydroxyapatite nanocrystals facilitates fluorescent labelling and visualisation of cellular internalisation. Journal of Materials Chemistry B. 2013;1(35):4370-8.

39. Kim D, Dhand V, Rhee K, Park S-J. Study on the Effect of Silanization and Improvement in the Tensile Behavior of Graphene-Chitosan-Composite. Polymers. 2015;7(3):527-51.

40. Esmonde-White K, Esmonde-White F. Raman spectroscopy in biomineralization. In: DiMasi E, Gower LB, editors. Biomineralization Sourcebook: Characterization of Biominerals and Biomimetic Materials: CRC; 2014.

41. Díez-Pascual AM, Martinez G, Gómez MA. Synthesis and Characterization of Poly(ether ether ketone) Derivatives Obtained by Carbonyl Reduction. Macromolecules. 2009;42(18):6885-92.

42. Conceicao TF, Bertolino JR, Barra GMO, Mireski SL, Joussef AC, Pires TN. Preparation and Characterization of Poly(Ether Ether Ketone) Derivatives. J Braz Chem Soc. 2008;19(1):111-6.

43. Naffakh M, Ellis G, Gómez MA, Marco C. Thermal decomposition of technological polymer blends 1. Poly(aryl ether ether ketone) with a thermotropic liquid crystalline polymer. Polymer Degradation and Stability. 1999;66:405-13.

44. Rao CNR, Venkataraghavan R, Kasturi TR. Contribution to the Infrared Spectra of Organosulphur Compounds. Canadian Journal of Chemistry. 1964;42:36-42.

45. Mioč UB, Ribnikar SV. Carbamates of the Lower Aliphatic Amines in Aprotic Solvents. I. Vibrational Spectra Bulletin de la Société chimique Beograd. 1978;43(9):603-12.

46. Chen GC, Rowell M, Ellis WD. Fungal Resistance of Southern Pine Impregnated with Methyl Fluorophenyl Carbamates or Reacted with Fluorophenyl Isocyanates. Wood and Fiber Science. 1990;22(2):165-72.

47. Robinson K, McCluskey A, Attalla MI. An ATR-FTIR study on the effect of molecular structural variations on the CO2 absorption characteristics of heterocyclic amines, part II. Chemphyschem. 2012;13(9):2331-41.

48. Loughran GM, Versluis A, Douglas WH. Evaluation of sub-critical fatigue crack propagation in a restorative composite. Dent Mater. 2005;21(3):252-61.

49. Rodrigues Jr. SA, Zanchi CH, de Carvalho RV, Demarco FF. Flexural strength and modulus of elasticity of different types of resin-based composites. Braz Oral Res. 2007;21(1):16-21.

50. Parvaiz MR, Mohanty S, Nayak SK, Mahanwar PA. Polyetheretherketone (PEEK) Composites Reinforced with Fly Ash and Mica. Journal of Minerals and Materials Characterization and Engineering. 2010;9(1):25-41.

51. Launey ME, Ritchie RO. On the Fracture Toughness of Advanced Materials. Advanced Materials. 2009;21(20):2103-10.

52. Gao H, Ji B, Jager IL, Arzt E, Fratzl P. Materials become insensitive to flaws at nanoscale: lessons from nature. Proc Natl Acad Sci U S A. 2003;100(10):5597-600.

Chapter 6. Conclusions and future work

6.0 GENERAL OVERVIEW

Whilst many hard tissue biomaterials ably serve their purpose as regenerative scaffolds and fusion devices, advancements in the formulation and fabrication of biomaterials are continually being driven forward by the need to meet the demands of an ever increasing and ageing population. The requirements of future bone graft substitutes and spinal implants requires composite biomaterials that are able to restore and support the regeneration of bone cost-effectively, as well as their use ultimately eliminating the need for revision surgery.

In order to deliver biomaterials of this nature, the aim of this thesis was to formulate calcium sulphate and phosphate based composites with enhanced properties that could be utilised in applications including bone regeneration and hard tissue fusion. This was achieved by identifying and formulating solutions to overcome the inherent limitations of current calcium based biomaterials. The formulation and characterisation strategies presented herein created, exploited and understood the interfacial interactions between organic/inorganic interfaces present between dissimilar phases. It was found that enhancing the organic/inorganic interfaces between dissimilar phases can result in significant improvements to the physiochemical attributes of the material and composite systems, as disseminated in each respective research chapter.

6.1 STUDY LIMITATIONS AND FUTURE PERSPECTIVES

6.1.1 Characterisation of novel poly (ether ether ketone)/calcium sulphate composite for bone augmentation

Chapter 2 is titled “Characterisation of novel poly (ether ether ketone)/calcium sulphate composite for bone augmentation” and focusd on the reinforcement of the biomedical cement, calcium sulphate (CS). Inorganic cements are used extensively in restoration of hard tissues such as bone, for instances where bone is unable to heal naturally. A reported limitation of CS is that it is very soluble when placed in physiological conditions and therefore may not provide a long-term scaffold for bone formation. Previously, it had been shown that polymer reinforcement of CS could slow resorption but lowered the mechanical properties. By reinforcing the ceramic with poly(ether ether ketone) (PEEK), a high performance engineering polymer, it was postulated that the properties of the ceramic content could be augmented, thus extending the period of time the osteogenic scaffold remains intact under physiological conditions. For the first time, both physical and chemical interfaces between the two materials were shown to develop as a result of a heat treatment process, which produced PEEK/CS composite materials. The treatment was found to be successful in reducing the rate of calcium sulphate degradation in a simulated physiological environment, as well as enhancing mechanical strength of the material.

As direct implication of this study, PEEK reinforcement of other biomedical ceramics may extend their longevity as an osteogenic scaffold *in vivo*. A calcium phosphate phase such as brushite ($CaHPO_4.2H_2O$), which

undergoes rapid dissolution when placed in the body, may benefit from such a treatment. Although it will likely dehydrate to monetite ($CaHPO_4$) at high temperature, which is more soluble, PEEK reinforcement may facilitate the hydration of the ceramic to brushite once the samples are placed in biological solutions.

From this study, the fate of PEEK following resorption of the degradable ceramic component remains unclear. It is assumed that if PEEK/CS were to be implanted, CS would provide an osteogenic scaffold for bone formation, with new bone taking up the volume occupied by CS and encasing the remaining PEEK framework. Following a dynamic ageing process over a period of 21 days, specimens of PEEK/CS with PEEK loadings >20 wt% remained intact and the CS structure underwent limited dissolution, although hydration of CS was detected. Had the ageing protocol been extended, it may have been possible to detect the onset of CS dissolution, and furthermore obtain the PEEK framework following complete dissolution of the CS. Prolonging the period of ageing would allow for further understanding as to the fate of PEEK, and moreover enable further study of *in vitro* biological responses to PEEK (e.g. cell attachment) in the absence of CS.

Further work should also investigate the loading of soluble therapeutics through liquid exchange with PEEK/CS materials, including antibiotics, as a preventative measure against infection, or growth factors to promote osteogenesis and bone healing. Additives may be incorporated by pre-soaking composites in solutions that contain the desired solute molecules prior to implantation.

Whilst PEEK was able to bring about significant gains in both the mechanical and degradation properties of CS, the compressive strength and modulus is short of the values acquired for other CS cements reported in the literature. Additionally therefore, compaction of CS and PEEK powders before hardening and heat-treatment, and increasing the P:L ratio whilst maintaining a workable formulation, may contribute to the reduction of pores that weaken hardened structures as has been previously demonstrated with other compositions of cement.

6.1.2 Biologically analogous calcium phosphate tubes from a chemical garden

Chapter 3 is titled “Biologically analogous calcium phosphate tubes from a chemical garden” showed that the interface between calcium loaded agar based hydrogel and phosphate solutions could be employed to produce tubular calcium phosphate structures. The structures produced were similar to chemical garden architectures. The micro scale architecture and composition of the resulting tubes makes them a prospective scaffold material for bone formation. However, *in vitro* studies need to be undertaken to determine the benefits of $CaPO_4$ tubular microstructure to facilitate cellular attachment and ingress, proliferation, and differentiation over conventional microstructures (e.g. powder micro particulates). Tubes can provide a high surface area, narrow pore distribution, and mass transport opportunities, which may benefit the development of an osteogenic environment over non-tubular materials.

Problematically, the tubule structures are very delicate, making it difficult to remove them from the solution phase. This may be overcome by encasing the tubules in a secondary phase, such as a ceramic slurry or polymeric hydrogel phase, that would penetrate the volume between tubules before hardening around them. The resulting structure would house the tubules, preserving their structure and facilitating an easier route of recovery following formation. Development of these structures could foreseeably be utilised as scaffolds for *in vitro* cell work regarding cellular viability and ingress.

6.1.3 Interfacial mineral fusion and tubule entanglement as a means to harden a bone augmentation material

Directly following on from the work in the preceding chapter, Chapter 4, titled “Interfacial mineral fusion and tubule entanglement as a means to harden a bone augmentation material”, explored the development of a bone graft technology that can harden *in situ* through generating biologically analogous tubular calcium phosphate structures. Calcium-loaded agarose spheres, and not just planar surfaces, were found to be capable of generating mineral tubes. This enabled the delivery of calcium-loaded hydrogel to bone defects, which could deposit tubular structures. Clinical application of the system was shown to be feasible using a defect model representative of a typical bone cavity encountered in surgery. Spheres in the vicinity of one another were able to unite within the defect through mineral deposited on adjacent sphere surfaces and interactions of tubule extensions.

Further work regarding this system should attempt to reduce the current Ca^{2+} and PO_4^{3-} concentrations required for tube growth to near physiologically relevant levels, as to limit the exposure of cells to harsh ionic concentrations that are potentially cytotoxic. Alterations in Ca^{2+} and PO_4^{3-} concentrations should maintain the capacity to generate a volume of mineral that is able to replenish a model defect. An *ex vivo* tissue model such as that employed in this chapter would be suitable, as it allows simultaneous characterisation of both native bone and mineral deposited, thus composition can be directly compared.

An alternative approach that would not require the adjustment of ionic concentrations would be to form a consolidated structure prior to implantation. This would require a mold of the defect site to be acquired and used as a template for which calcium loaded spheres can be packed into before stimulating mineralisation using concentrated phosphate solutions. Once unified, the construct could then be implanted *in vivo* providing an immediate scaffold for bone growth.

A limitation of employing an agarose hydrogel as the primary delivery vehicle of calcium ions in this system is its ability to provide biomechanically stability during defect healing. To overcome this, reinforcement of the spheres with ceramic particulates may increase the load bearing capability of the spheres whilst hardening within a bone defect. These particulates may also act as seeds of further nucleation throughout the hydrogel spheres. This would advantageously encourage mineralisation throughout the soft

component, in addition to the extensive mineral deposition upon the exterior of spheres and regions of porosity between spheres.

6.1.4 Development of a covalently bonded hydroxyapatite and poly(ether ether ketone) composite

Chapter 5, titled “Development of a covalently bonded hydroxyapatite and poly(ether ether ketone) composite”, explored the development of a covalently linked PEEK and hydroxyapatite (HA) composite material for spinal fusion devices. Currently, the addition of bioactive particulates into polymer matrices such as PEEK results in a trade-off in mechanical properties. Given that the interface between polymer and bioceramic particulates is crucial to mechanical performance, a method of covalently linking the two phases that assists in the transference of mechanical loading between brittle and ductile components was developed.

Chemically linking HA and PEEK significantly improves the flexural modulus of composites intended for the fabrication of spinal implants. The study demonstrates that the interfacial interactions between composite components can be improved beyond mechanical interlocking and physiochemical interactions by obtaining a direct chemical link between polymer and additive phases. Between HA and PEEK, the chemical linking procedure lessened particulate debonding, reduced the development of microcracks, and facilitated enhanced load transfer between the polymer matrix and filler particulates compared to HA_PEEK composites without linking. Consequently, the loading of HA within PEEK could be increased

without a loss of mechanical properties, which would be of benefit to the fusion capacity of a spinal fusion device fabricated from HA_L_PEEK.

Whilst this approach may potentially allow greater loadings of HA to be included in a PEEK matrix resulting in an increase in its fusion capacity and integration with hard tissue, further expansion of the of HA loadings are required. Production of the HA_L_PEEK additive was limited by a low yield synthesis method. Improvement in the yield of additive may be improved by alterations in reaction time and pH adjustment, ultimately requiring a systematic study into these effects.

Further work in this area should look to reducing inclusion particle size and increase the range of additive loadings mechanically tested. Ideally, smooth nano-scale spherical particulates should be introduced to increase the surface area of interaction with the matrix. Such particulates will also ensure more homogeneous distribution of the additive phase, reducing the variation between localized areas of composition and ultimately allow higher loadings of HA to be included for the purpose of enhancing bone/implant interface and attaining greater levels of bone growth.

In vitro biological analysis of the composites should additionally be undertaken to ensure osteoblast like cells attach and can proliferate upon chemically linked composites. It is currently unknown as to whether the chemistries present within the chemically linked HA_L_PEEK are cytotoxic under physiological conditions. Cytotoxicity may result from the chemistries not being compatible in the processed composite, or as a result of the hydrolytic or cell mediated break down and release of dissolution products

originating from the linking chemistry. Supernatant that has contained chemically linked HA_L_PEEK material may be analysed further to determine release of potentially cytotoxic products.

Thereafter*, in vitro* studies should then explore the detection of osteogenic differentiation and mineralisation markers produced by osteoblast precursor cells seeded upon chemically linked composites. The results may be used to indicate the most appropriate formulation for spinal fusion application. With regards to spinal fusion application, a composite that induces osteoblastic differentiation and mineralisation may accelerate fusion time.

6.2 CONCLUSIVE SUMMARY

In summary, the work presented in this thesis covers the development of several biomaterials and their subsequent characterisation, providing a valuable contribution to the literature, knowledge and industry. This was achieved by following the logical progression of the stated objectives. The research findings show that improving the organic/inorganic interactions between differing phases of a composite system significantly enhances the physiochemical nature and performance of the resulting novel biomaterials.

Given that prevention strategies to reduce hard tissue injury will never eliminate the evident need to restore and regenerate bone tissue in an ever increasing and ageing population, the systematic approaches taken in this thesis allow for the creation of new, improved and relevant composite formulations. Limitations of the novel composite systems conceived may be

overcome through future study and systematic method alteration. Overall, the methods herein address the requirement for the formulation biomaterials with augmented application parameters.

Appendix Part 1

Characterisation of a novel poly (ether ether ketone)/calcium sulphate composite for bone augmentation

Supporting information:

Figures

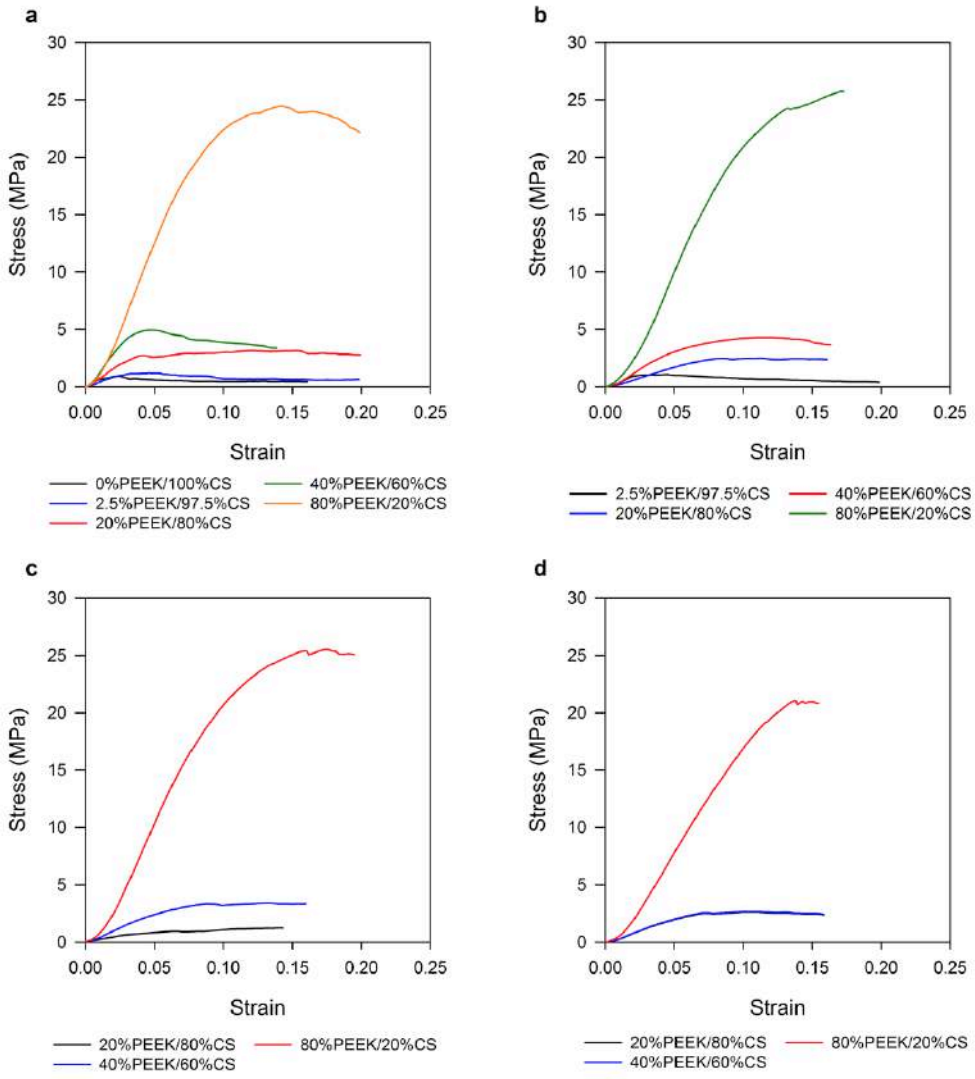

Figure S2.1 Averaged stress vs. strain curves for n=10 PEEK/CS specimens tested **(a)** after heat treatment prior to ageing (0 Days) and **(b)** after 7 Days, **(c)** 14 Days and **(d)** 21 Days of ageing.

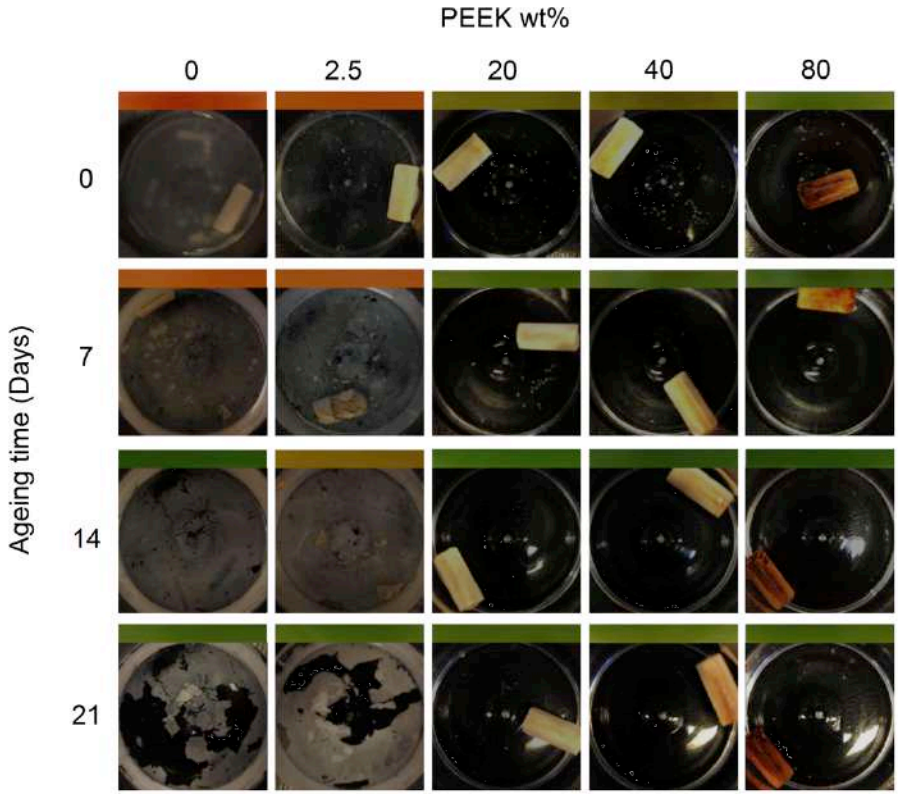

Figure S2.2 Top down view of PEEK/CS specimens during dynamic ageing study at 1 day, 7 days, 14 days and 21 days, bar above individual images is the colouration of an aliquot of PBS ageing media after addition of universal pH indicator before replenishment (PBS media was green) (orange = pH 5 – 5.5, yellow = pH 6 – 6.5, green = pH 7 - 7.5).

Equations

% volumetric shrinkage = $((V_1 - V_2) / V_1) \times 100$ (Equation S2.1)

Where,

V_1 = Volume of specimen prior to heat treatment (mm^3)

V_2 = Volume of specimen after heat treatment (mm^3)

$\rho_{rel} = \rho_{app} / \rho_{true}$ (Equation S2.2)

Where,

ρ_{rel} = Relative density of specimen (g/cm^3)

ρ_{app} = Apparent density of specimen (g/cm^3)

ρ_{true} = True density of specimen (g/cm^3)

Porosity = $(1 - \rho_{relative}) \times 100$ (Equation S2.3)

Where,

$\rho_{relative}$ = Relative density of specimen

$\sigma = F / A$ (Equation S2.4)

Where,

σ_{comp} = Compressive stress (MPa)

F = Loading force (N)

A = Specimen contact area (mm^2)

$\varepsilon = l_{change} / l_{original}$ (Equation S2.5)

Where,

ε = Strain

l_{change} = Change in specimen height (mm)

$l_{original}$ = Original specimen height (mm)

$E_{comp} = (\sigma / \varepsilon) / 1000$ (Equation S2.6)

Where,

E_{comp} = Compressive modulus (GPa)

σ = Stress (MPa)

ε = Strain

Appendix Part 2

Biologically analogous calcium phosphate tubes from a chemical garden

Supporting information:

Figures

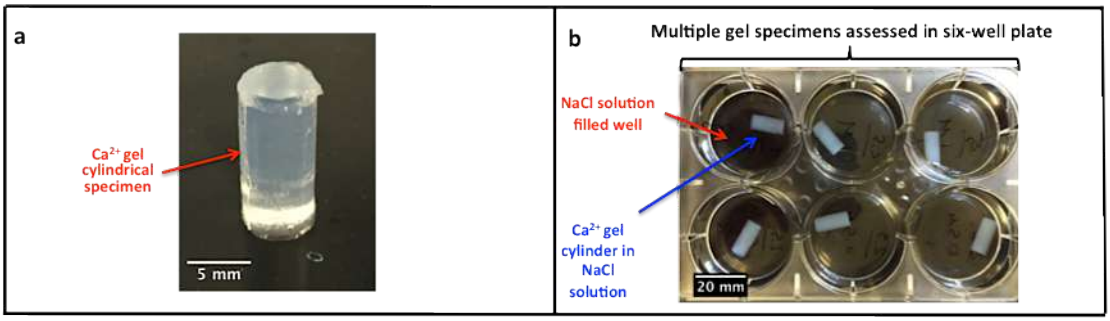

Figure S3.1 A 12 mm x 6 mm gel specimen employed in gel mass gain/loss studies **(a)** and gels soaking in various NaCl solutions **(b)**.

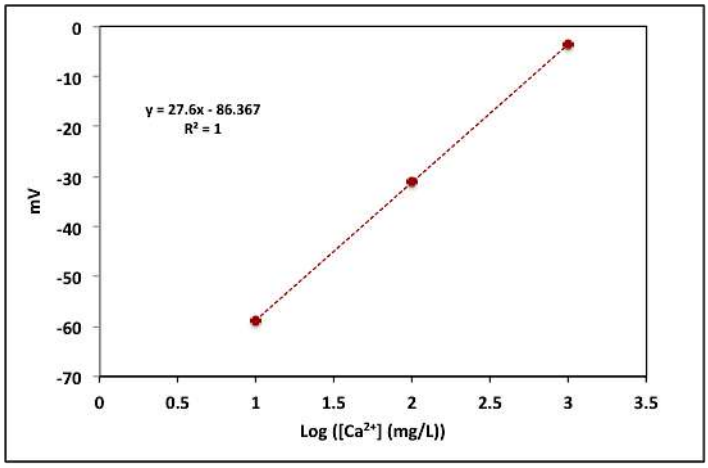

Figure S3.2 Ca^{2+} calibration curve of mV against Log Ca^{2+} concentration of known standards (equation of trend line and r^2 value shown, each data point represents n=1).

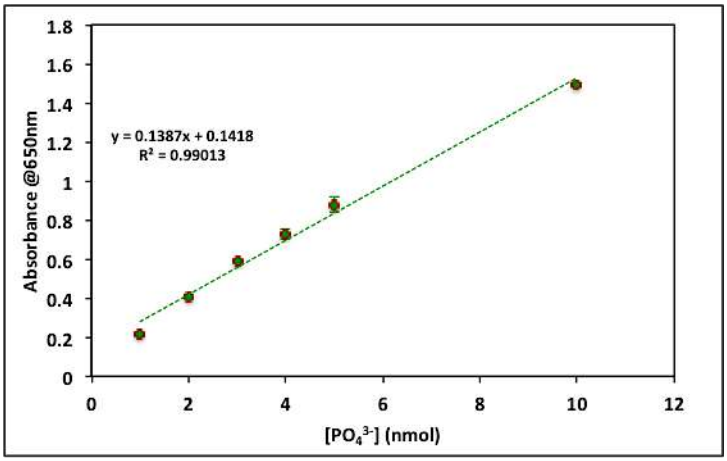

Figure S3.3 PO_4^{3-} calibration curve of absorbance @650 nm against PO_4^{3-} concentration of known standards (equation of trend line and r^2 value shown, each data point is average of n=2, error bars represent standard deviation).

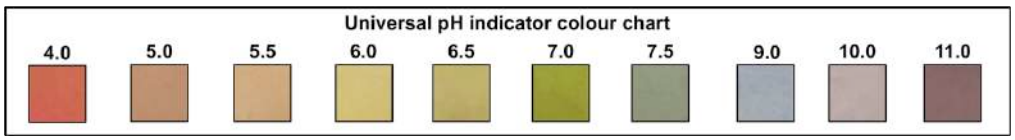

Figure S3.4 Universal pH indicator solution colour change corresponding to values of pH between 4 and 11.

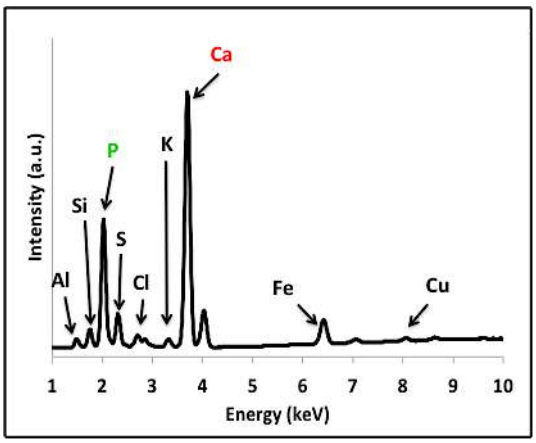

Figure S3.5 XRF spectrum of area covering tube section and background material support.

Tables

Table S3.1 Concentrations of PO_4^{3-} and NaCl salts with equivalent solute potentials used in experiments.

PO_4^{3-} [M]	**NaCl [M]**	**Equivalent solute potential (bar)**
0.25	0.5	-24.8
0.5	1	-49.5
1	2	-99.1
1.5	3	-148.6
2	4	-198.1
2.5	5	-247.6

Equations

$$[Ca^{2+}]_f = \frac{20mL \times [Ca^{2+}]_m}{(20ml\text{-}V_{rep})} \quad \text{(Equation S3.1)}$$

Where, $[Ca^{2+}]_f$ = Final Ca^{2+} concentration eluted, $[Ca^{2+}]_m$ = Measured Ca^{2+} concentration detected in sample, V_{rep} = Total replenishment volume

$M_{gel\ sol} = M_{gel} \times 0.98$ (Equation S3.2)

Where, $M_{gel\ sol}$ = Mass of gel specimem solution phase content (assuming 98% water content), M_{gel} = Mass of gel specimen.

$\psi_S = -iCRT$ (Equation S3.3)

Where, ψ_S = Solute potential, i = Ionisation constant, C = Solution concentration, R = Gas constant, T = Temperature (Conversion from bar to MPa, 1 bar = 0.1 Mpa)

Appendix Part 3

Interfacial mineral fusion and tubule entanglement as a means to harden a bone augmentation material

Supporting information:

Figures

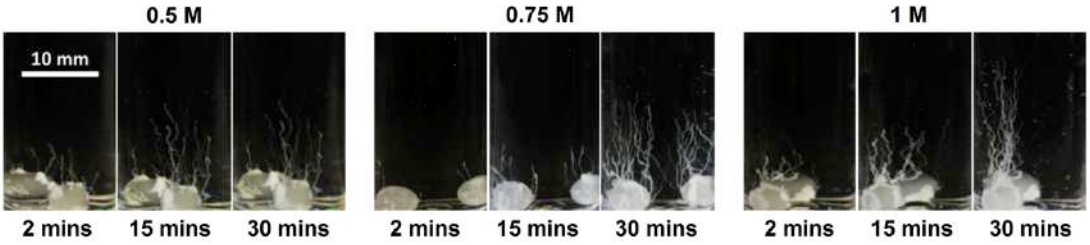

Figure S4.1 Calcium phosphate tubule growth after 2 mins, 15 mins, and 30 mins from calcium loaded spheres placed in phosphate solutions at concentrations of 0.5 M, 0.75 M, and 1 M.

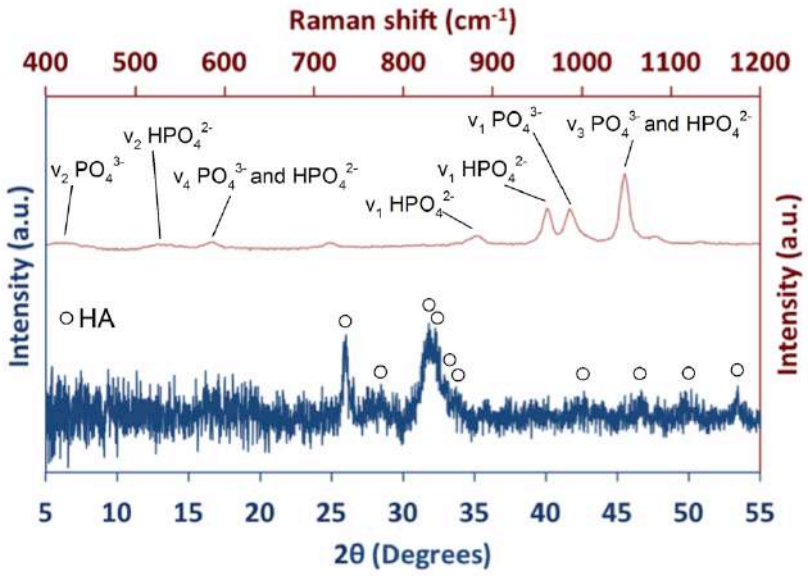

Figure S4.2 Raman spectrum (red) and powder XRD pattern (blue) of tubule precipitate harvested at 3 h. The presence of both HA and DCPD is confirmed

by Raman spectroscopy through the identification of stretching and bending modes associated with PO_4^{3-} ions (found in HA) and HPO_4^{2-} ions, present in the structure of HA and DCPD respectively. The predominant crystalline phase constituting tubule precipitate was found to be HA. Inability to identify DCPD peaks suggests the phase exists in an amorphous form. Peak broadening a high noise to signal ratio suggests the mineral is of low crystallinity overall; a characteristic also true of mammalian bone mineral.

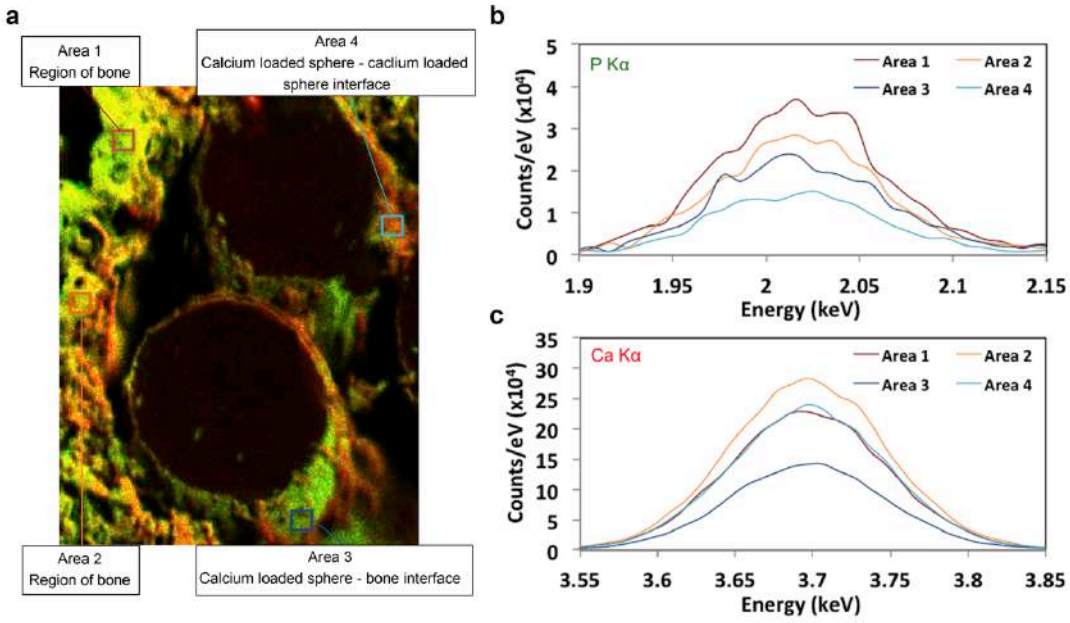

Figure S4.3 (a) μ-XRF elemental mapping of a cross-section of the human hard tissue defect (Kα channels for calcium (red) and phosphate (green) shown), as presented in Figure 3c. μ-XRF spectra were acquired for the total scan points within the referenced square areas placed upon areas of mineral. The areas selected account for two areas of bone (Areas 1 and 2), a mineral fusion interface between a calcium loaded sphere and bone (Area 3), and likewise between two calcium loaded spheres within the defect (Area 4). **(b)**

Spectra of highlighted areas for the P Kα signal. **(c)** Spectra of highlighted areas for the Ca Kα signal. Both **(b)** and **(c)** show slight variation in Kα signal strength, however, there exists a distinct elemental similarity between mineral deposited within and about the periphery of the defect volume.

Appendix Part 4

Development of a covalently bonded hydroxyapatite and poly(ether ether ketone) composite

Supporting information:

Figures

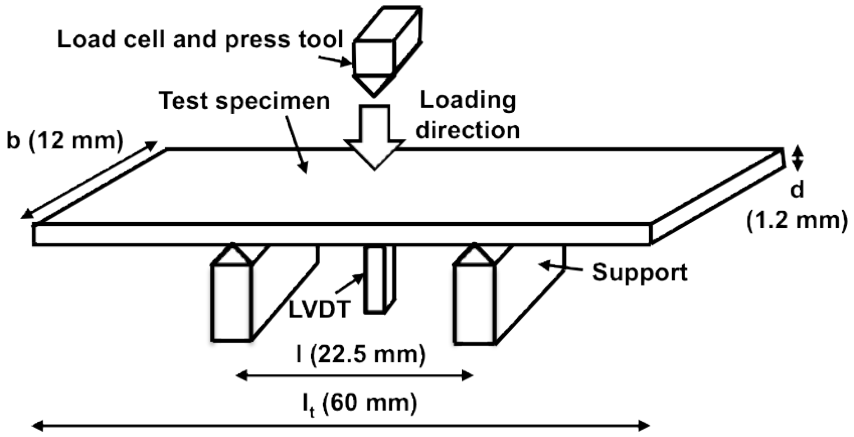

Figure S5.1 Schematic of mechanical 3-point bend testing set-up, where b = specimen width, d = specimen thickness, l = separation length between supports, l_t = total specimen length, and LVDT = linear variable displacement transducer. Specimen dimensions and support separation distance comply with ASTM D790/ISO 178 standard.

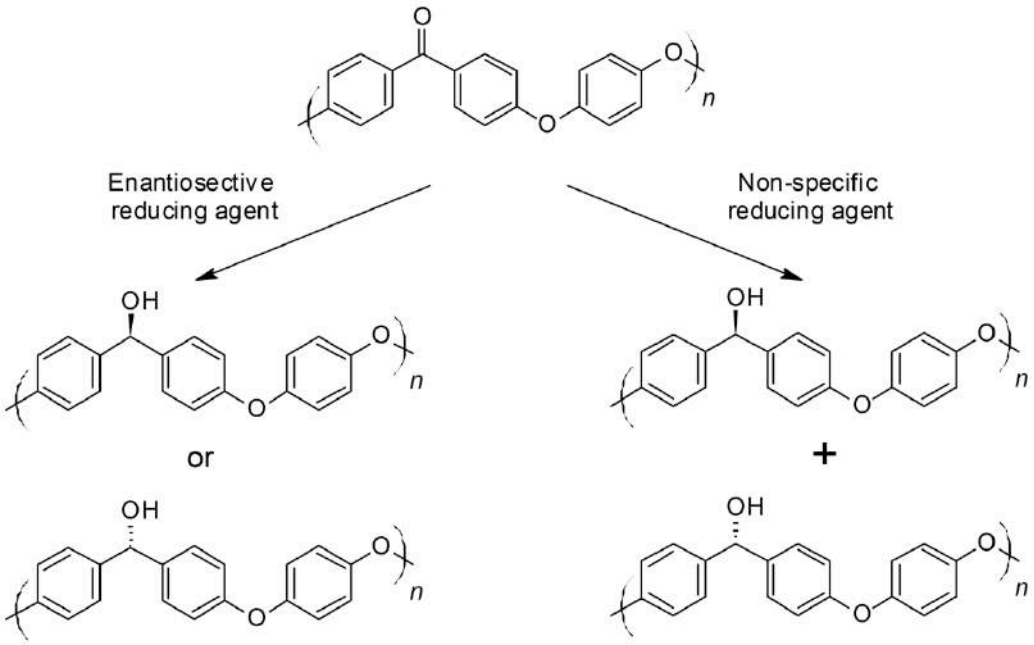

Figure S5.2 PEEK reduction to PEEK-OH by entioselective and non-specific reducing agents resulting in chiral or non-chiral forms of PEEK-OH respectively.

Chirality is introduced when PEEK is chemically modified by reducing agents facilitating the conversion of =O groups to –OH groups. An enantioselective reducing agent may produce only one enantiomer of PEEK-OH, whereby the –OH groups are configured in one direction. Because $NaBH_4$ is non-selective, a mixture of PEEK-OH enantiomers is expected. The mixture of resulting –OH group configurations may disrupt forming crystallites of the material leading to an increase in the amorphous nature of PEEK-OH compared to PEEK.

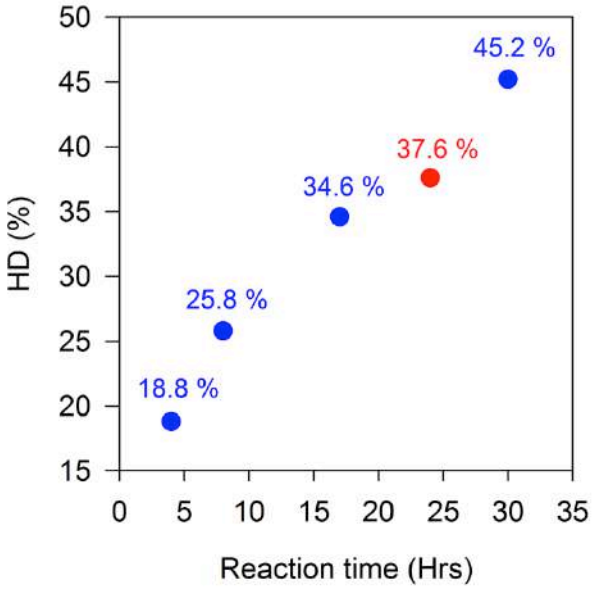

Figure S5.3 PEEK-OH hydroxylation degree (HD) resulting from the reaction of PEEK with $NaBH_4$ at various reaction times. Shown in red is the value for HD acquired in this work, whilst values shown in blue are those reported by Díez-Pascual and colleagues [1].

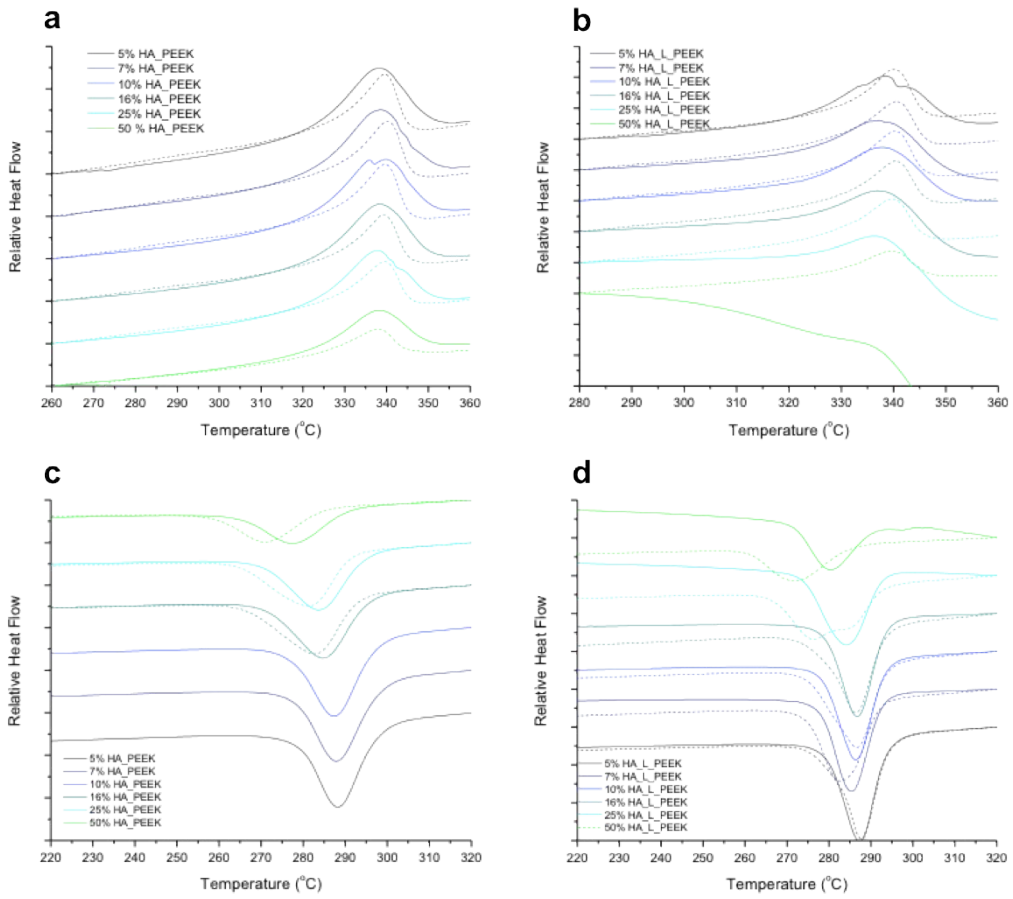

Figure S5.4 Dynamic scanning colorimitry (DSC) traces for HA_PEEK and HA_L_PEEK materials. Heating runs for (a) HA_PEEK materials and (b) HA_L_PEEK. Cooling runs for (c) HA_PEEK materials and (d) HA_L_PEEK (solid lines are those of run 1, dashed lines are those of run 2)

Regarding the HA_PEEK and HA_L_PEEK materials, run 1 heating traces appear to contain some noise contamination indicative of polymer movement in the melt (Figure S5.4a,b). This is not apparent in the second heating run, suggesting that the samples settled within the DSC sample pan. Interestingly, a pronounced drop off in the DSC trace is observed for HA_L_PEEK material containing > 25 wt % HA content (Figure 5.4b). We attribute this to loss of excess solvent present in the HA_L_PEEK that was not

removed during our purification steps, as during the second heating run, the traces conform to a regular pattern.

The cooling curves are noteworthy in that as the HA content increases, the crystallisation of PEEK appears to be hindered, given that exotherm shift to reduced temperatures with increasing HA content (Figure S5.4c-d). Re-crystallisation may be affected more extensively within HA_L_PEEK as the re-crystallisation temperatures are consistently lower than those observed for HA_PEEK. This may be due to the improved interaction between HA chemically linked to PEEK in this system.

These preliminary data appear to suggest the interfacial interactions present in HA_L_PEEK affect the re-crystallisation of the material more extensively than the interactions present between non-linked phases comprising HA_PEEK. Furthermore, processing considerations for these materials may need to take into account the effects of solvent release during initial heating, especially at loadings >25 wt% HA in HA_L_PEEK composites.

Equations

$$\sigma_f = \frac{3Fl}{2bd^2} \qquad \text{(Equation S5.1)}$$

Where: σ_f= Flexural strength (MPa), F= Max force before yielding or fracture (N), l= Test specimen support separation length (mm), b= Test specimen width (mm), and d= Test specimen thickness (mm).

$$E_f = \frac{Fl^3}{4bd^3\delta}$$ (Equation S5.2)

Where: E_f= Flexural modulus (MPa), F= Force (N), l= Test specimen support separation length (mm), b= Test specimen width (mm), d= Test specimen thickness (mm), and δ= Test specimen displacement (V_{DC}).

$$C = \frac{A}{Eb}$$ (Equation S5.3)

$$M = 2.80\ \text{mL} \times \left(C \times \frac{1\ \text{L}}{1000\ \text{mL}}\right)$$ (Equation S5.4)

$$C_{sample} = \left(\frac{M}{0.25\ \text{mL}}\right) \times \frac{1000\ \text{mL}}{1\ \text{L}}$$ (Equation S5.5)

Where: C = -SH concentration as measured (mol L^{-1}), E = TNB molar absorption coefficient, 14150 (M^{-1} cm^{-1}), b =path length of cuvette (1 cm), M = -SH concentration as measured (mol), and C_{sample} = -SH concentration of the sampled volume 0.25 mL containing HA-SH (mol L^{-1}).

The concentration of –SH groups was converted from units of mol L^{-1} to mol g^{-1} by calculating the equivalent mass in grams of HA-SH sample in 1 L and dividing C_{sample} by this number (e.g. 20 g HA-SH in 1 L so 20).

$$M_{250^oC} = \left(\frac{M_S}{100}\right) \times \%\ M_{250^oC}$$ (Equation S5.6)

$$M_{400^oC} = \left(\frac{M_S}{100}\right) \times \%\ M_{400^oC}$$ (Equation S5.7)

$$M_{OH} = \%\, M_{400^oC} - M_{250^oC} \quad \text{(Equation S5.8)}$$

$$mol_{OH} = \frac{M_{OH}}{Mr_{OH}} \quad \text{(Equation S5.9)}$$

$$M_{PEEK\text{-}OH} = mol_{OH} \times Mr_{PEEK\text{-}OH} \quad \text{(Equation S5.10)}$$

$$HD = \left(\frac{M_{PEEK\text{-}OH}}{M_{250^oC}}\right) \times 100 \quad \text{(Equation S5.11)}$$

Where: M_s = TGA sample mass (g), M_{250^oC} = TGA sample mass at 250 °C (g), $\%\, M_{250^oC}$ = % TGA sample mass remaining at 250 °C (%), M_{400^oC} = TGA sample mass at 400 °C (g), $\%\, M_{400^oC}$ = % TGA sample mass remaining at 400 °C (%), M_{OH} = Mass of OH groups lost from PEEK-OH between 250 °C and 400 °C (g), mol_{OH} = Moles of OH groups lost from PEEK-OH between 250 °C - 400 °C (g), Mr_{OH} = Molar mass of OH group (g mol^{-1}), $M_{PEEK\text{-}OH}$ = Mass of PEEK-OH in sample (g), $Mr_{PEEK\text{-}OH}$ = Molar mass of PEEK-OH group (g mol^{-1}), and HD = PEEK-OH hydroxylation degree (%).

References

[1] Díez-Pascual AM, Martínez G, Gómez MnA. Synthesis and Characterization of Poly(ether ether ketone) Derivatives Obtained by Carbonyl Reduction. Macromolecules. 2009;42(18):6885-92.